

Copyright © 2003 by Jonathan Neal Blakely
All rights reserved

Report Documentation Page			Form Approved OMB No. 0704-0188		
Public reporting burden for the collection of information is estimated to average 1 hour per response, including the time for reviewing instructions, searching existing data sources, gathering and maintaining the data needed, and completing and reviewing the collection of information. Send comments regarding this burden estimate or any other aspect of this collection of information, including suggestions for reducing this burden, to Washington Headquarters Services, Directorate for Information Operations and Reports, 1215 Jefferson Davis Highway, Suite 1204, Arlington VA 22202-4302. Respondents should be aware that notwithstanding any other provision of law, no person shall be subject to a penalty for failing to comply with a collection of information if it does not display a currently valid OMB control number.					
1. REPORT DATE 2003		2. REPORT TYPE		3. DATES COVERED 00-00-2003 to 00-00-2003	
4. TITLE AND SUBTITLE Experimental Control of a Fast Chaotic Time-Delay Opto-Electronic Device			5a. CONTRACT NUMBER		
			5b. GRANT NUMBER		
			5c. PROGRAM ELEMENT NUMBER		
6. AUTHOR(S)			5d. PROJECT NUMBER		
			5e. TASK NUMBER		
			5f. WORK UNIT NUMBER		
7. PERFORMING ORGANIZATION NAME(S) AND ADDRESS(ES) Duke University ,Department of Physics,Durham,NC,27708			8. PERFORMING ORGANIZATION REPORT NUMBER		
9. SPONSORING/MONITORING AGENCY NAME(S) AND ADDRESS(ES)			10. SPONSOR/MONITOR'S ACRONYM(S)		
			11. SPONSOR/MONITOR'S REPORT NUMBER(S)		
12. DISTRIBUTION/AVAILABILITY STATEMENT Approved for public release; distribution unlimited					
13. SUPPLEMENTARY NOTES					
14. ABSTRACT see report					
15. SUBJECT TERMS					
16. SECURITY CLASSIFICATION OF:			17. LIMITATION OF ABSTRACT Same as Report (SAR)	18. NUMBER OF PAGES 147	19a. NAME OF RESPONSIBLE PERSON
a. REPORT unclassified	b. ABSTRACT unclassified	c. THIS PAGE unclassified			

EXPERIMENTAL CONTROL OF A FAST CHAOTIC TIME-DELAY OPTO-ELECTRONIC DEVICE

by

Jonathan Neal Blakely

Department of Physics
Duke University

Date: _____

Approved: _____

Dr. Daniel J. Gauthier, Supervisor

Dr. Robert P. Behringer

Dr. Stephen W. Teitsworth

Dr. Joshua E. S. Socolar

Dr. William Joines

Dissertation submitted in partial fulfillment of the
requirements for the degree of Doctor of Philosophy
in the Department of Physics
in the Graduate School of
Duke University

2003

ABSTRACT

(Physics)

EXPERIMENTAL CONTROL OF A FAST CHAOTIC TIME-DELAY OPTO-ELECTRONIC DEVICE

by

Jonathan Neal Blakely

Department of Physics
Duke University

Date: _____

Approved: _____

Dr. Daniel J. Gauthier, Supervisor

Dr. Robert P. Behringer

Dr. Stephen W. Teitsworth

Dr. Joshua E. S. Socolar

Dr. William Joines

An abstract of a dissertation submitted in partial
fulfillment of the requirements for the degree
of Doctor of Philosophy in the Department of
Physics in the Graduate School of
Duke University

2003

Abstract

The focus of this thesis is the experimental investigation of the dynamics and control of a new type of fast chaotic opto-electronic device: an active interferometer with electronic bandpass filtered delayed feedback displaying chaotic oscillations with a fundamental frequency as high as 100 MHz. To stabilize the system, I introduce a new form of delayed feedback control suitable for fast time-delay systems. The method provides a new tool for the fundamental study of fast dynamical systems as well as for technological exploitation of chaos.

The new opto-electronic device consists of a semiconductor laser, a Mach-Zehnder interferometer, and an electronic feedback loop. The device offers a high degree of design flexibility at a much lower cost than other known sources of fast optical chaos. Both the nonlinearity and the timescale of the oscillations are easily manipulated experimentally. To characterize the dynamics of the system, I observe experimentally its behavior in the time and frequency domains as the feedback-loop gain is varied. The system displays a route to chaos that begins with a Hopf bifurcation from a steady state to a periodic oscillation at the so-called fundamental frequency. Further bifurcations give rise to a chaotic regime with a broad, flattened power spectrum. I develop a mathematical model of the device that shows very good agreement with the observed dynamics.

To control chaos in the device, I introduce a new control method suitable for fast time-delay systems, in particular. The method is a modification of a well known control approach called time-delay autosynchronization (TDAS) in which the control perturbation is formed by comparing the current value of a system variable to its value at a time in the past equal to the period of the orbit to be stabilized. The current state of a time-delay dynamical system retains a memory of the state of the

system one feedback delay time in the past. As a result, the past state of the system can be used to predict the current state. In order to take advantage of this effect, the new control method forms a perturbation according to the TDAS scheme but delays actuation of the control perturbation by a time equal to the feedback delay time of the system to be controlled. This effectively sets the control-loop latency equal to the feedback delay time of the uncontrolled system. I demonstrate this control method experimentally by stabilizing a periodic orbit of the active interferometer. I quantify the effectiveness of the controller by measuring the range of feedback loop gains over which the orbit can be stabilized. The stabilized orbit, which oscillates with a frequency of 51.8 MHz, is the fastest unstable periodic orbit in a chaotic system controlled experimentally to date.

Application of the new control method requires the adjustment of two time delays in the controller. The first, the control delay time, should equal the period of the orbit to be controlled, while the second, the control loop latency, should equal the feedback delay time of the system to be controlled. I investigate, through experiments and simulations, the sensitivity of the method to errors in setting these time delays. I find that the control delay time must be set exactly equal to the period of the orbit to minimize the control perturbations when the orbit is stabilized. In contrast, the control loop latency may vary within a finite range without affecting the performance of the controller.

Acknowledgments

Although only one author is given credit for this thesis, there are many contributors. It is fitting that their contributions be recognized at the outset.

First, I would like to acknowledge the financial support of the U. S. Army Research Office, grant number DAAD19-02-1-0223.

I am deeply indebted to my advisor, Dr. Daniel J. Gauthier, for being a true mentor. He has always been generous with praise when I earned it, advice when I badly needed it, and constructive criticism when I deserved it. Besides being a first rate scientist, he is also a good editor - something every physics grad student writing a thesis badly needs.

I appreciate the time and consideration given to this thesis by the members of my committee.

I have been fortunate to work with some wonderful collaborators. Drs. Louis Pecora and Thomas Carroll contributed experimental data and constructive ideas to the first paper I published. Although they are both eminent persons in the field of non-linear dynamics, they always treated me as a colleague when I was but a humble third year gradstudent. Dr. Joshua Socolar and two of his students, Ian Harrington and Philipp Hövel, helped me to understand the role of time delays in control and dynamics. Dr. Lucas Illing, who joined our group as I was already writing my thesis, began contributing ideas immediately.

During my seven short years at Duke, I had the pleasure of sharing an office with a fine group of graduate students: David Sukow, Martin Hall, William Brown, Micheal Stenner, Seth Boyd, Hana Dobrovolny, Hejeong Jeong, and J.-P. Smits. I'm also indebted to the post-doctoral researchers who have passed through the group over the last seven years. Dr. Olivier Pfister, now on the faculty of the University of Virginia, had a fantastic sense of humor and a tremendous enthusiasm for physics. Dr. Sonya Bahar brought an artistic sense to the office. Dr. John Swartz was known as "the guy who can fix things" (*e.g.* the Coke machine). Dr. Lucas Illing I have already mentioned above.

Throughout the many years of my education, I have learned from a number of gifted and inspiring teachers. I would like to recognize, in particular, my high school physics teacher, Charles Payne, and the physics faculty at the University of North Carolina at Greensboro, Drs. Robert Muir, Steve Danford, Promod Pratap, and Gaylord Hageseth, in particular.

Finally, I would like to thank my family for giving me the foundation and support to succeed in life. My parents, Lee and Melanie Blakely, taught me the value of working hard. My beautiful wife, Christina, has been with me through the ups and downs of graduate school. Her faith in me and enthusiasm for me have never faltered.

Contents

Abstract	iv
Acknowledgments	vi
List of Figures	ix
List of Tables	xvi
1 Introduction	1
1.1 Chaotic Dynamics	1
1.2 Overview of Thesis	3
2 Control and Latency	8
2.1 Control-Loop Latency: A Linear Example	10
2.2 Latency and Controlling Fast Chaos	19
3 The Active Interferometer with Bandpass-Filtered Time-Delayed Feedback	25
3.1 Experimental Apparatus	28
3.2 Mathematical Model	31
3.2.1 The Semiconductor Laser	32
3.2.2 The Mach-Zehnder Interferometer	40
3.2.3 The Electronic Feedback Loop	47
3.3 Experimental Determination of Model Parameters	50
3.4 Dynamics of Closed-Loop System without Modulation	56
3.4.1 Hopf Bifurcation	57
3.4.2 Route to Chaos	64

3.5	Dynamics with External Modulation	70
3.6	Discussion	76
4	Modified TDAS Control for Time-Delay Systems	78
4.1	Modified TDAS Control	79
4.2	Experimental Demonstration of Modified TDAS Control	83
4.2.1	Modified TDAS Controller Implementation	85
4.2.2	Procedure for Measuring Delays	88
4.2.3	Observation of Control	89
4.3	Mathematical Model of Interferometer with Controller	95
4.4	Summary	101
5	Influence of Delay Mismatch in the Modified TDAS Control Method	103
5.1	Simulations	105
5.2	Experimental Observations	108
5.3	Discussion	113
6	Conclusion	115
6.1	Summary	115
6.2	Future Directions	117
	Bibliography	120
	Biography	130

List of Figures

1.1	A new fast chaotic opto-electronic device: The active interferometer with delayed bandpass nonlinear electronic feedback.	4
1.2	Time series of optical power emitted by the interferometer when the device is undergoing fast chaotic oscillation. Note that the timescale of the oscillation is 5-10 ns.	5
1.3	Block diagram showing the general form of the class of time delay systems to which the modified TDAS method may be applied. The basic elements are a low pass filter, a nonlinear element ($f[x]$), and a delayed feedback loop. Well known models such as the Ikeda and Mackey-Glass equations are of this form.	6
2.1	Block diagram showing basic parts of any feedback control scheme. The time, τ_ℓ , between measuring the state of the system and actuating the control is known as the control loop latency.	9
2.2	Domain of control of the fixed point at origin of the first-order linear dynamical system with instantaneous proportional feedback control. The axes show the bifurcation parameter, a , and the control gain, b	13
2.3	D -partition of the ab parameter space. The dashed lines show curves on which the characteristic quasipolynomial has at least one root with a real part equal to zero.	15
2.4	D -partition of the ab parameter space used to locate the domain of control. In Region I, no roots of the characteristic quasipolynomial have positive real parts. In Regions II and III, one and two roots have positive real parts, respectively.	16
2.5	Domain of control of the first-order linear system with proportional feedback control and non-zero control loop latency. Control is only possible when latency, τ_ℓ , is less than the response time of the system, a^{-1}	18
3.1	Schematic of active interferometer with delayed band-pass filtered electronic feedback. The device produces chaotic oscillations on nanosecond timescales.	27

3.2	Photograph of the experimental apparatus. The black box left of center is the laser housing. The path of the laser beam is highlighted by the thick white line. The coil of coax cable to the right of center is the delay line.	29
3.3	Schematic diagram of the electronic feedback loop including the photodiode and laser. The components labelled A-I are as follows: A - Hamamatsu silicon photodiode S4751; B - MiniCircuits directional coupler ZFDC-20-4; C - MiniCircuits amplifier ZFL-1000L; D - MiniCircuits amplifier ZFL-1000GH; E - Coaxial cable RG 58/U; F - MiniCircuits power combiner ZFSC-2-1W-75; G - bias-T in Thorlabs laser mount TCLDM9; H - Thorlabs laser diode controller LDC-500; I - Hitachi laser diode HL6501MG.	30
3.4	The first component of the active interferometer with delayed bandpass feedback: The semiconductor laser. The laser provides linear conversion of changes in the injection current to changes in the optical power and frequency.	32
3.5	(a) Simplified schematic of a semiconductor laser. (b) Schematic of a typical “buried heterostructure” laser. Cladding layers provide both carrier confinement and lateral optical waveguiding.	34
3.6	Square of relaxation oscillation frequency as a function of injection current. By operating with a large DC injection current, I ensure that the laser is never modulated at frequencies near the relaxation oscillation.	38
3.7	The second component of the active interferometer with delayed bandpass feedback: The Mach-Zehnder interferometer. The interferometer provides the nonlinearity needed to obtain chaos.	40
3.8	(a) Schematic of a Mach-Zehnder interferometer with unequal optical path lengths. (b) There are four separate paths through the interferometer. At each output port, the beams from two paths combine and interfere.	42
3.9	The third component of the active interferometer with delayed bandpass feedback: The electronic feedback loop. Time delay and bandpass filtering are produced by the feedback loop.	47

3.10	Block diagram of feedback loop. Light from the interferometer is converted into an electrical signal by the photodiode (PD). All electrical components are lumped into one amplifier with gain γ , one low-pass filter with time constant τ_L , one high-pass filter with time constant τ_H , and a time delay of τ_D . Finally, the electrical signal is converted back into light by the laser diode (LD).	48
3.11	Setup for open loop measurements used to determine the transfer characteristics of the feedback loop.	52
3.12	Frequency response of open loop system at two different gain values: (a) $\gamma = 14.6$, (b) $\gamma = 4.8$	54
3.13	Setup for open loop measurements used to determine parameter α	55
3.14	Time series of optical power detected at second port of interferometer with feedback gain $\gamma = 4.0$ mV/mW. The system is in a steady state with fluctuations due to phase noise.	58
3.15	Experimental and simulated data showing how the amplitude of the periodic oscillation increases with the feedback gain γ . (a) The filled circles show the experimentally measured amplitude. The large error bars are due to the influence of phase noise near the transition. The open circles show data from the model. (b) A closer look at the model data near the bifurcation point. The line is a least squares fit to the points just beyond the bifurcation. The linear scaling of the square of the amplitude with the feedback gain indicates a supercritical Hopf bifurcation.	59
3.16	Time series from the (a) experiment and (b) model of the output at the second interferometer port in periodic regime. The feedback gain is $\gamma = 6.8$ mV/mW.	60
3.17	Hopf frequency as a function of delay time τ_D . Circles are data points from the numerical model. Triangles are experimental data points. The dotted lines show the function n/τ where $n = 1, 2, 3, \dots$	62

3.18	Hopf frequency predicted by linear stability analysis of steady state. The solid line corresponds to the active interferometer with bandpass feedback. The dotted line corresponds to the same system but with the high-pass filtering removed from the feedback loop. The discrete frequency jumps due to the high-pass filter are not displayed in well-known low-pass systems such as the Ikeda and Mackey-Glass. . . .	63
3.19	Experimentally measured time series and power spectra measured from the second output port of interferometer. Three steps on the route to chaos are shown.	66
3.20	Time series and power spectral densities from model at the same gains as experimental data shown in Fig. 3.19.	69
3.21	A closer look at the low-frequency part of the power spectral density of the interferometer output from the model with $\gamma = 13.2$ mV/mW. The frequency resolution is four times higher than in Fig. 3.20(b). .	70
3.22	Frequency locking due to weak external modulation at a frequency near the fundamental oscillation frequency. The circles show experimental data. The solid line shows results from the mathematical model. The feedback gain is $\gamma = 6.3$ mV/mW.	72
3.23	Experimentally measured time series and power spectra of the output power at the second port of the active interferometer with external modulation showing route to chaos as γ is increased. The loop gain γ is (a) 2.2 mV/mW, (b) 8.8 mV/mW, (c) 11.0 mV/mW, and (d) 15.4 mV/mW. The period-doubled orbit in (b) has a much stronger component at half the fundamental frequency (~ 26 MHz) than in the undriven system (see Fig. 3.19(b)).	73
3.24	Time series and power spectra from the numerically integrated model of the modulated system showing the route to chaos. As in the experiment, the frequency content of the period doubled orbit has a much stronger component at half the fundamental frequency than the similar orbit in the unmodulated case (see Fig. 3.20(b)). The gain γ is (a) 2.2 mV/mW, (b) 8.8 mV/mW, (c) 11.0 mV/mW, and (d) 15.4 mV/mW.	75

4.1	Block diagram showing the general form of the class of time-delay systems to which the modified TDAS method may be applied. The basic elements are a low pass filter, a nonlinear element ($f[x]$), and a delayed feedback loop. Well known models such as the Ikeda and Mackey-Glass equations are of this form.	81
4.2	Autocorrelation function of the nonlinear term of the Ikeda model of a passive nonlinear resonator in the regime of high dimensional chaos. The peak at τ_D suggests that a delayed version of the nonlinear term may contain sufficient information about the current state of the system to successfully control it.	82
4.3	Block diagram showing the modified TDAS control scheme. The feedback control signal is the difference between the values of the nonlinear function $f[x]$ at times separated by the period of the desired orbit. The control loop latency is set equal to τ_D	83
4.4	Schematic diagram of active interferometer and controller. A photodetector at the second port of the interferometer converts the emitted power into a voltage. The voltage signal is split. One half is delayed by a time τ_P and then subtracted from the other. The resulting signal is amplified and combined with the feedback loop of the interferometer before the bias-T. The propagation time through the controller is set equal to the feedback delay time, τ_D	84
4.5	Schematic diagram of the modified TDAS controller. The components labelled A-I are as follows: A - Hamamatsu silicon photodiode S4751; B - Coaxial cable RG 58/U and variable delay; C - MiniCircuits power splitter/combiner ZFSC-2-1W-75; D - Coaxial cable RG 58/U and variable delay; E - M/ACOM 180 hybrid junction H-9; F - MiniCircuits directional coupler ZFDC-20-4; G - MiniCircuits amplifier ZFL-1000GH; H - MiniCircuits directional coupler ZFDC-10-1; I - MiniCircuits power splitter/combiner ZFSC-2-1W-75.	85

4.6	Typical experimental power spectra recorded when the feedback gain $\gamma = 12.4$. (a) The control gain $\gamma_c = 0.08$ is small enough that the spectrum is indistinguishable from that of the system with no control. (b) The control gain $\gamma_c = 5.5$, well within the domain of control. The large peaks at half-integer multiples of the fundamental frequency are suppressed more than 20 dB below their uncontrolled amplitude and the broad background falls several dB below its uncontrolled level. (c) The control gain $\gamma_c = 9.4$, new sideband frequencies appear around the fundamental frequency and its harmonics indicating control is no longer effective.	90
4.7	Experimentally measured average error signal at three different gain values. The dashed line shows the cutoff of 4.2 mV chosen to define the domain of control.	92
4.8	Experimentally measured domain of control. At each point, the root mean square of the error signal was compared with a cutoff value. The black dots mark points below the cutoff.	93
4.9	Time series of power emitted from created by numerically integrating model of inteferometer and controller. The feedback gain is $\gamma = 14.0$ mV/mW. (a) Uncontrolled irregular oscillation with $\gamma_c = 0$ mV/mW. (b) Stabilized oscillation near the fundamental frequency with $\gamma_c = 4.5$ mV/mW.	97
4.10	Root mean square of error signal from model. Domain of control is estimated by recording control gain values that produce an error signal below a cutoff value. The dashed horizontal line shows the cutoff at 0.01 mW.	99
4.11	Domain of control of modified TDAS applied to the model of the active interferometer.	101
5.1	(a) Experimental and (b) theoretical domains of control as determined in the previous chapter. The black circle shows the point in each domain at which the data in this chapter is collected.	106
5.2	Average error signal in the modified TDAS controller as control loop latency is varied in the mathematical model. The feedback gain $\gamma = 12.28$ and the control gain $\gamma_c = 4.65$	107

5.3	Average error signal in the modified TDAS controller as control loop latency is varied in the mathematical model. The feedback gain $\gamma = 12.28$ and the control gain $\gamma_c = 4.65$. A wide range of latency from zero to over $2\tau_D$ is shown in (a). The region around the minimum is shown in more detail in (b).	109
5.4	The control delay is determined by the difference in propagation time through the two highlighted sections. The direct path is shown as a heavy dashed line. The delayed path is shown as a heavy solid line.	110
5.5	Average error signal in the modified TDAS controller as the control time delay is varied. The circles show experimental values. The feedback gain $\gamma = 12.28$ and the control gain $\gamma_c = 4.65$. The solid line shows the simulation reproduced from Fig. 5.2.	111
5.6	Schematic diagram of active interferometer with modified TDAS control. The control loop latency is the propagation time around the path shown here by the heavy black line.	112
5.7	Average error signal in the modified TDAS controller as the control loop latency is varied. The circles show experimental values. The feedback gain $\gamma = 12.28$ and the control gain $\gamma_c = 4.65$. The solid line shows the simulation reproduced from Fig. 5.3.	113

List of Tables

3.1	Physically relevant values of model parameters	51
3.2	Dynamic transitions in the opto-electronic device without modulation as the feedback gain is varied.	65
3.3	Experimentally observed dynamic transitions in the modulated sys- tem as the feedback gain is varied.	74
4.1	Shortest period orbits controlled experimentally in chaotic systems. The modified TDAS method described in this chapter is used to stabilize the shortest timescale dynamics reported to date. Note that with this method the latency need not be small compared to the period of the orbit.	94

Chapter 1

Introduction

1.1 Chaotic Dynamics

Since efforts by the earliest astronomers to predict the motion of celestial bodies, *dynamics*, or the evolution of a system in time, has been a central concern of physical science [1]. Today, the study of dynamics is an active branch of physics driven by the amazing variety of phenomena observed in nonlinear dynamical systems, such as spontaneous pattern formation and solitons. Without question, one of the most widely studied nonlinear dynamical phenomena is *chaos*. Chaotic dynamics play a role in nearly every branch of physics, including condensed matter [2, 3], atomic physics [4], cosmology [5, 6], high energy physics [7, 8], and optics [9, 10].

As the name “chaotic” implies, these dynamical systems display highly irregular, even random-like oscillations. In the phase space of a chaotic system, trajectories beginning at initially close points diverge exponentially fast. However, trajectories are bounded and evolve asymptotically toward a fractal set known as a *strange attractor*. Embedded within the strange attractor are a large (even infinite) set of unstable periodic orbits (UPO). Loosely speaking, these orbits form the skeleton of the strange attractor. Given a knowledge of the UPOs, one can determine important dynamical invariants and statistical properties that characterize the chaotic dynamics [11]-[17].

In 1990, Ott, Grebogi, and Yorke [18] demonstrated that it is possible to *control* chaos in the sense that unstable periodic orbits in a chaotic attractor can be stabilized by feedback control applying only small perturbations. They pointed out that

since chaotic evolution is ergodic a chaotic system will eventually come arbitrarily close to any given UPO. Thus, the controller simply waits for the system to visit the neighborhood of the desired orbit and then applies only weak perturbations to keep it there. Numerous chaos control schemes have since been developed and demonstrated on a wide variety of physical systems [19]. Chaos control schemes are important tools for building a fundamental understanding of chaotic dynamics because they provide a means for identifying and characterizing UPOs.

Chaos control methods are also of great practical importance given the abundance of nonlinear systems in nature and technology [20]. These methods dramatically enhance the tools available to control engineers. Chaos control is now an active area of research in the field of control theory [21, 22].

My contribution to this field is an experimental investigation of the control of a fast time-delay chaotic system. Delay dynamical systems evolve in an infinite dimensional phase space and display a wide range of behavior including multistability and high-dimensional chaos. In some respects, delay-dynamical systems are analogous to spatially extended systems with the time delay playing the role of the system size [23, 24]. While time-delay systems have been studied extensively, there are many aspects of the dynamics of these systems that are poorly understood. Chaos control techniques suitable for time-delay chaotic systems assist both in the fundamental understanding and the technological exploitation of time-delay dynamics.

The complexity and versatility of time-delay dynamics have inspired a number of proposed technological applications such as secure communications [25]-[33], dynamic memory [34, 35], and chaos-based computation [36, 37]. Many of these applications require high-speed chaotic fluctuations to facilitate rapid transmission or processing of data. At the same time they require tools for manipulating the

chaotic system such as chaos control methods. However, control of fast chaotic systems is particularly challenging. The reason is that all controllers require some finite processing time, known as *control loop latency* [38], between observing the state of the system and perturbing the system to effect control. If the state of the chaotic system changes significantly during the latency time, the control perturbation may not affect the system in the intended manner and, consequently, control may fail. Thus, control of fast chaotic systems requires the development of novel control techniques that mitigate the influence of control loop latency.

1.2 Overview of Thesis

This dissertation documents my investigation of controlling a fast chaotic time delay system. It consists of six chapters. Chapter 2 presents a pedagogical introduction to control loop latency, and a brief review of the methods for controlling fast chaos developed prior to my research. Chapter 3 describes a new time-delay chaotic opto-electronic device. The next two chapters describe the application of a new method of controlling fast time-delay systems to the opto-electronic device. The control method is a modification of the time delay autosynchronization (TDAS) method that is well-suited for fast time delay systems because it allows for a relatively large amount of control loop latency. In Chapter 4, I present an experimental demonstration of the modified TDAS control method. In Chapter 5, I examine the influence of the control time delay and latency on the effectiveness of control. I summarize my main results and discuss the direction of future work in Ch. 6.

In particular, I frame the problem of controlling fast dynamics in Chapter 2 through a pedagogical example and a brief review of research that has preceeded my work. First, I examine the stabilization of the steady state of a one dimensional linear system for which the domain of control with and without latency can be

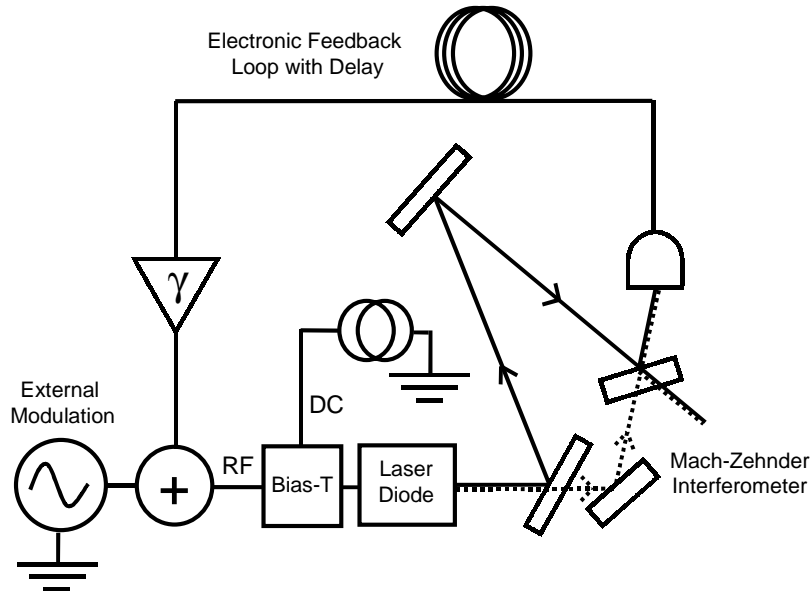


Figure 1.1: A new fast chaotic opto-electronic device: The active interferometer with delayed bandpass nonlinear electronic feedback.

determined analytically. Then I review several techniques for controlling chaotic dynamics. Beginning with the original OGY method [18], I follow the development of controllers designed specifically for controlling fast chaotic systems such as Pyragas's time delay autosynchronization [39].

In Chapter 3, I introduce a flexible and inexpensive new source of fast optical chaos suitable both for use in high-speed applications and low-speed laboratory experiments. The system, shown schematically in Fig. 1.1, consists of a diode laser, a Mach-Zehnder interferometer, and an electronic delayed feedback loop that modulates the diode's injection current according to the power output by the interferometer. I examine the dynamics of the system when it is running autonomously and with external modulation provided by an RF voltage. In both cases, the laser

emission undergoes a periodic oscillation when the gain in the feedback loop is low. The frequency of oscillation is determined by the feedback delay time. As the gain is increased, the periodic state gives way to chaos through a series of bifurcations. Figure 1.2 shows a time series of the intensity at the interferometer output port

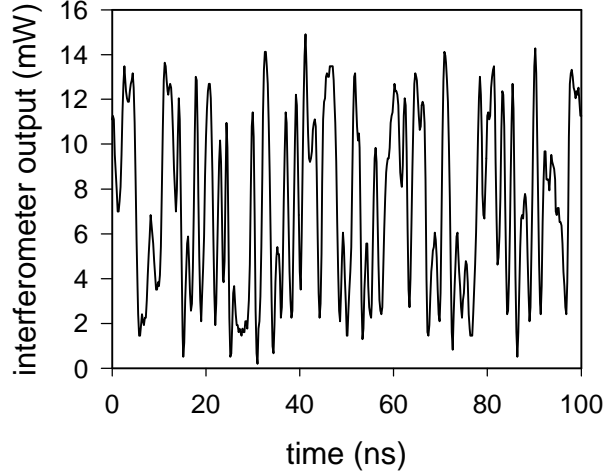


Figure 1.2: Time series of optical power emitted by the interferometer when the device is undergoing fast chaotic oscillation. Note that the timescale of the oscillation is 5-10 ns.

during fast chaotic oscillation on a nanosecond timescale. To obtain a theoretical understanding of the behavior of the device, I develop a detailed mathematical model that reproduces accurately the observed dynamics. This fast time delay system serves as a testbed for the control method introduced in the next chapter.

In Chapter 4, I propose a new method for controlling chaos in fast time delay systems. A block diagram of such a system is shown in Fig. 4.1. The basic elements of systems in this class are a low-pass filter, a nonlinear element, and a delayed feedback loop. Well known models such as the Ikeda [40] and Mackey-Glass [41] equations are members of this class as well as several chaotic opto-electronic devices [42]-[45], [34]. The new method of control is a modification of the TDAS control

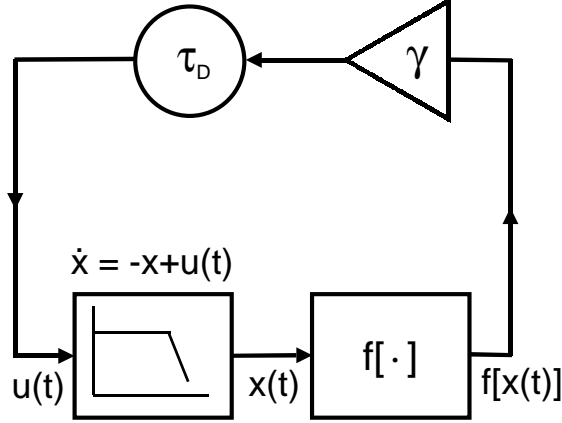


Figure 1.3: Block diagram showing the general form of the class of time delay systems to which the modified TDAS method may be applied. The basic elements are a low pass filter, a nonlinear element ($f[x]$), and a delayed feedback loop. Well known models such as the Ikeda and Mackey-Glass equations are of this form.

technique where the feedback is nonlinear and the control loop latency is precisely set equal to the time delay in the uncontrolled system. Specifically, the form of the modified TDAS feedback is

$$\delta p(t) = \gamma_c \{f[x(t - \tau_D)] - f[x(t - \tau_D - \tau_P)]\} \quad (1.1)$$

where $\delta p(t)$ represents the continuous adjustment of an accessible system parameter p about its nominal value, $f[x(t)]$ is the output of a nonlinear element in the system, τ_D is the time delay of the chaotic system to be controlled, τ_P is the period of the unstable orbit to be stabilized, and γ_c is the control gain. I demonstrate the application of this technique by using it to control the active interferometer with bandpass feedback. To quantify the effectiveness of the controller, the domain of control is estimated experimentally and numerically.

In Chapter 5, I continue my study of the modified TDAS control method by examining the influence of the control time delay and control loop latency on the

success of the controller. I review studies of the role of these delays in the original TDAS method and indicate aspects of these results that should apply also to the modified TDAS method. In experiments and simulations, the effectiveness of control is observed as each of these delays is varied around its nominal value. The results are compared to expectations based on the original TDAS method.

In Chapter 6, the final chapter of this thesis, I review the main results of my experiments and discuss the direction of future work. The active interferometer with bandpass delayed feedback may be a suitable system for a number of possible applications such as message encoding and random number generation. The modified TDAS control method represents a step forward in the search for effective control methods for fast chaotic time delay systems.

Chapter 2

Control and Latency

Many techniques exist for “controlling” dynamical systems, that is, manipulating them to produce a desired behavior [21]-[46]. A very common approach to control a system is to use a feedback loop to stabilize an otherwise unstable behavior of the system [46]. A typical feedback loop in a controller consists of the basic components shown in Fig. 2.1. First, some information about the state of the system is gathered through measurements. Next, the information is used to determine how the system should be perturbed in order to produce the desired behavior rather than the natural evolution of the uncontrolled system. Finally, an actuator applies the perturbation. In many cases these three tasks can be completed in a span of time over which the state of the dynamical system changes very little. Then, for computational convenience, the feedback may be considered to be instantaneous. However, in any real feedback control scheme, a finite amount of time is required for the controller to observe the system, determine the nature of the perturbation, and apply the perturbation.

This amount of time is called the *control-loop latency*, labelled τ_ℓ in Fig. 2.1. If the unstable system’s state changes significantly in the time interval between measurement and actuation, the perturbation may no longer be appropriate for stabilizing the system. Thus, the latency of a controller places a practical limit on the speed of the instabilities it can stabilize.

To get an idea of when latency poses a practical problem, consider a very simple but commonly used control method known as *proportional feedback control* [46]. In this method, the controller produces a perturbation proportional to the difference

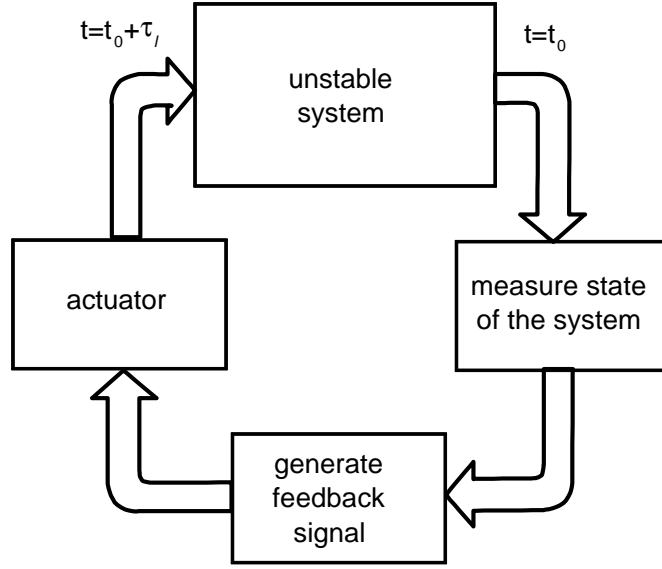


Figure 2.1: Block diagram showing basic parts of any feedback control scheme. The time, τ_l , between measuring the state of the system and actuating the control is known as the control loop latency.

between a measurement of the state of the system and a reference value. Suppose the state of the system is quantified by a voltage (produced by a measurement transducer, for example). First, consider a controller implemented using a personal computer with an analog-to-digital converter to record the measurement, some high-level software like LabView to evaluate the difference between the measured state and the reference value, and a digital-to-analog converter to actuate the control. In that case, the latency would be on the order of $10 \mu\text{s}$. Therefore, unstable dynamics involving frequencies beyond about 50 kHz would be too fast. If the controller is implemented using analog electronics such as operational amplifiers (10 MHz typical bandwidth at unity gain), then instabilities with a ~ 5 MHz characteristic frequency could likely be stabilized. Using RF electronics, which typically have a bandwidth on the order of 1 GHz, latency could be reduced to a few nanoseconds, allowing control of ~ 500 MHz fluctuations.

In the case of proportional feedback control, any one of these implementations is possible. However, such a simple controller is not effective in many cases, such as stabilizing unstable periodic orbits in chaotic or other nonlinear systems. More complex controllers that produce very good results when applied to slow systems cannot be implemented so easily at higher frequencies. Thus, there is a clear need for control techniques designed specifically to work in the regime of “fast” dynamics, *i.e.* when the latency is comparable to the characteristic time-scale of the dynamical system. The following chapters will describe a new approach to controlling one class of fast chaotic systems, but first a review of the basic problem of control with latency and past approaches to solving it is presented here. In Sec. 2.1, I illustrate the problem posed by control loop latency through a simple example for which the domain of control and its dependence on latency can be calculated analytically. In Sec. 2.2, I review the development of controllers for fast chaotic systems.

2.1 Control-Loop Latency: A Linear Example

In this section, I introduce several ideas needed to understand the problem of latency in a controller. The concepts of stability, control, and latency are illustrated by the example of a first-order linear dynamical system. An analysis of this system provides a simple demonstration of how control fails due to latency.

Consider the very simple dynamical system described by the linear differential equation

$$\dot{x} = ax. \tag{2.1}$$

The point $x = 0$ is the only *fixed point* of the system, that is, a point in phase space where $\dot{x} = 0$ [48]. Suppose the fixed point, denoted by x_* , is the desired behavior of the system. Consider the effect of a small perturbation from the fixed

point $\delta = x - x_*$. The evolution of this perturbation is obtained by substituting into Eq. 2.1 to obtain the differential equation

$$\dot{\delta} = a\delta, \quad (2.2)$$

the solution to which is

$$\delta(t) = \delta_o e^{at}, \quad (2.3)$$

where δ_o is the initial perturbation to the system. If $a < 0$, the perturbation decays and the fixed point is stable. On the other hand, if $a > 0$, the perturbation will grow so the fixed point is unstable. In a situation where the fixed point represents a desired behavior but is unstable, a controller can be added to the system to maintain the desired behavior. I will assume $a > 0$ for the rest of this section.

Note that a is the exponential growth rate of perturbations and therefore is the natural time scale of the dynamical system. When control is added to the system it is reasonable to expect that latency will degrade the performance of the controller when it is of the order of or greater than a^{-1} . In this case, the perturbation can grow significantly before the controller can respond. Before demonstrating this formally, I will examine the case of instantaneous feedback.

To stabilize the fixed point, I apply proportional feedback control as described above. The system state is compared to a reference state (the fixed point in this case) and a signal proportional to the difference is fed back to the system affecting its future evolution. When the feedback is instantaneous, the dynamical system plus controller is described by the differential equation

$$\dot{x} = ax + b(x - x_*), \quad (2.4)$$

where b denotes the strength of the feedback or *control gain*. Since $x_* = 0$, Eq. 2.4

can be rewritten as

$$\dot{x} = (a + b)x. \quad (2.5)$$

To determine the controller's effect on the stability of the fixed point, I again consider a small perturbation, $\delta = x - x_*$. Equation 2.5 implies the perturbation will evolve according to the differential equation

$$\dot{\delta} = (a + b)\delta \quad (2.6)$$

whose solution is given by

$$\delta(t) = \delta_o e^{(a+b)t}. \quad (2.7)$$

From Eq. 2.7, the effect of the controller is clear. If $b < -a$, the perturbation decays and the fixed point is stable. A useful method of visualizing the effect of a controller is to plot the control gain b versus a system parameter, such as a . The region in this plot where the unstable state is stabilized by the controller is referred to as the domain of control. Figure 2.2 shows the domain of control for the example system with proportional feedback control and no control-loop latency.

Having demonstrated how a desired behavior of a dynamical system is attained through feedback control, two important points should be noted. First, in this example, the desired behavior happened to be a fixed point or steady state. In general, unstable periodic states (more accurately *unstable periodic orbits* or UPOs) in phase space can be controlled, too [21, 22]. In fact, research on controlling chaos tends to focus on stabilizing UPOs rather than fixed points. The reason for this is that chaotic systems typically contain an infinite number of UPOs, presenting a surprising degree of flexibility from a single system. Second, adding the controller to the dynamical system does not change the location of the fixed point; only the stability of the fixed point is altered. Some schemes for control do involve making

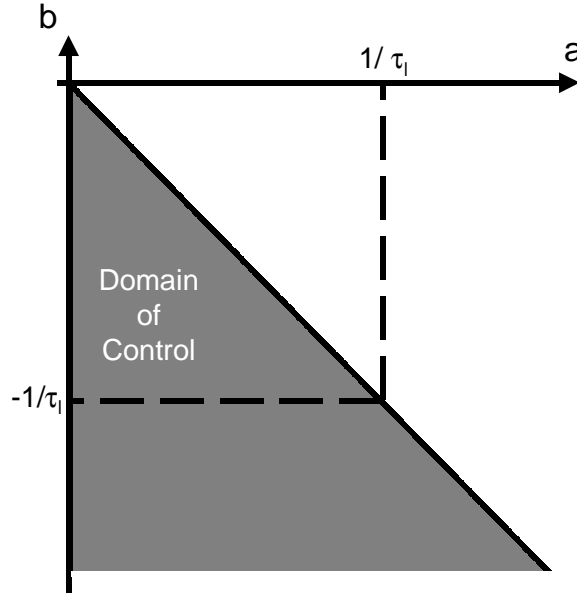


Figure 2.2: Domain of control of the fixed point at origin of the first-order linear dynamical system with instantaneous proportional feedback control. The axes show the bifurcation parameter, a , and the control gain, b .

dramatic changes to the phase space of the unstable system such as altering UPOs or creating new UPOs. However, it is often desirable that the behavior of the unstable system should be preserved, *e. g.* to minimize the power used by the controller. Thus, the controller should not introduce new UPOs into the dynamics.

To investigate the effect of latency on the controller, I determine how the domain of control changes as latency becomes significant. Suppose the control signal is applied at a time τ_ℓ later than it would be if it were instantaneous. The evolution of the dynamical system is then given by

$$\begin{aligned}\dot{x}(t) &= ax(t) + b\{x(t - \tau_\ell) - x_*\}, \\ &= ax(t) + bx(t - \tau_\ell).\end{aligned}\tag{2.8}$$

Once again, the controller's effect on the stability of the fixed point is determined

by examining the evolution of a small perturbation $\delta = x - x_*$. Equation 2.8 implies the perturbation will evolve according to

$$\dot{\delta}(t) = a\delta(t) + b\delta(t - \tau_\ell) \quad (2.9)$$

To solve this equation, I insert an exponential trial solution into Eq. 2.9 of the form

$$\delta(t) = \delta_0 e^{\lambda t} \quad (2.10)$$

where λ is the eigenvalue of the fixed point. The result is the characteristic equation

$$\begin{aligned} \lambda &= a + be^{-\lambda\tau}, \\ \lambda - a - be^{-\lambda\tau} &= 0. \end{aligned} \quad (2.11)$$

The left hand side of Eq. 2.11 is known as the *characteristic quasipolynomial* and will be denoted $\Phi(\lambda)$. If the fixed point is to be stable, *i.e.* the perturbation is to decay, there must be no solutions to Eq. 2.11 containing a positive real part. Equivalently, $\Phi(\lambda)$ must have no roots with positive real parts. The region in the ab parameter space where this condition is satisfied is the domain of control.

To find this region, I use the *method of D-partition* [47]. I divide the ab plane into distinct regions separated by curves on which $\Phi(z)$ has at least one root with real part equal to zero. At all points within one such region of the plane, $\Phi(\lambda)$ has the same number of roots with a positive real part. This partition of the parameter space is known as a *D-partition*. To locate the domain of control, I identify the particular region in which that number is zero. The first boundary curve is found by setting λ equal to zero to get the line

$$a = -b. \quad (2.12)$$

To obtain the rest, assume $\lambda = iy$ so Eq. 2.11 becomes

$$iy - a - be^{-iy\tau} = 0. \quad (2.13)$$

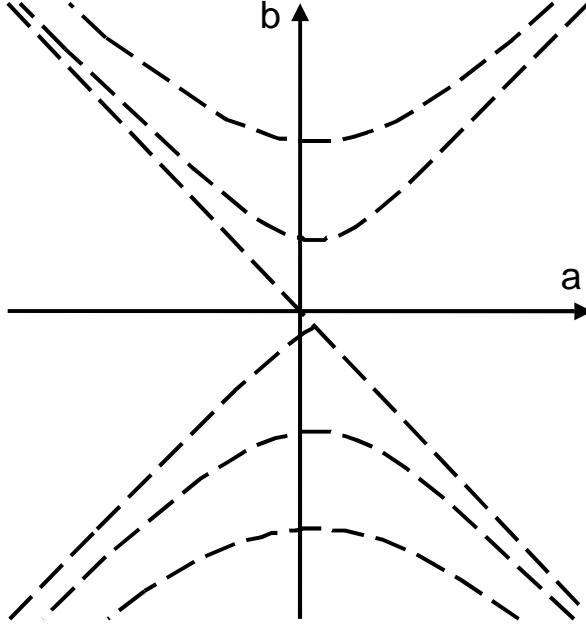


Figure 2.3: D -partition of the ab parameter space. The dashed lines show curves on which the characteristic quasipolynomial has at least one root with a real part equal to zero.

Separating the real and imaginary parts gives the parametric form of the infinite set of curves that make up the remaining boundaries

$$a = y \frac{\cos \tau_\ell y}{\sin \tau_\ell y}, \quad (2.14)$$

$$b = \frac{-y}{\sin \tau_\ell y}. \quad (2.15)$$

One curve defined by these equations meets the line $a = -b$ at a cusp point $(1/\tau_\ell, -1/\tau_\ell)$. The first few bounding curves closest to the origin are shown in Fig. 2.3.

A closer view of the region surrounding the origin is given in Fig. 2.4

In the simple case where $a < 0$ and no control is applied ($b = 0$), the fixed point is stable so no solutions to Eq. 2.11 have positive real parts. Therefore, for all

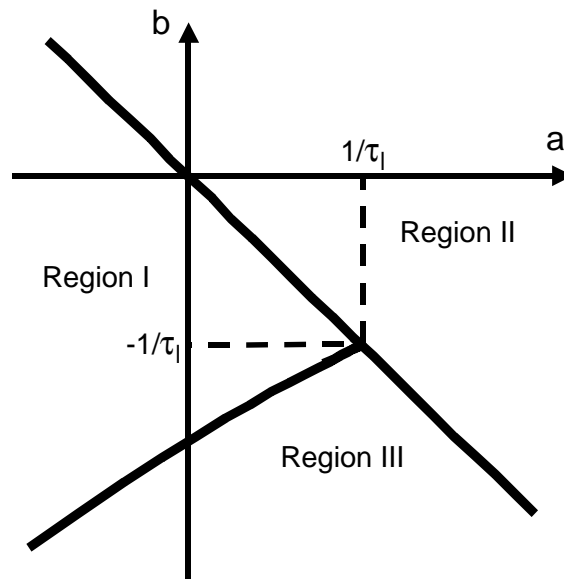


Figure 2.4: *D*-partition of the ab parameter space used to locate the domain of control. In Region I, no roots of the characteristic quasipolynomial have positive real parts. In Regions II and III, one and two roots have positive real parts, respectively.

points in Region I of Fig. 2.4 there are no solutions to Eq. 2.11 with positive real parts. To determine the number of roots with positive real part in Region II, note that along the line $b = 0$ the characteristic equation reduces to the simple form

$$\lambda = a, \quad (2.16)$$

so there is clearly only one root with a positive real part. (As $b \rightarrow 0$, the real parts of all the roots except one approach $-\infty$.)

To determine the number of roots with positive real part in region III, consider the sign of the differential of the root of $\Phi(\lambda)$ with zero real part as a boundary is crossed. Specifically, if

$$\Phi(\lambda, a, b) = 0, \quad (2.17)$$

then

$$\frac{\partial \Phi}{\partial \lambda} d\lambda + \frac{\partial \Phi}{\partial a} da + \frac{\partial \Phi}{\partial b} db = 0. \quad (2.18)$$

The differential of the real part of the root is

$$\text{Re}(d\lambda) = \text{Re} \left(\frac{-\frac{\partial \Phi}{\partial a} da - \frac{\partial \Phi}{\partial b} db}{\frac{\partial \Phi}{\partial \lambda}} \right). \quad (2.19)$$

Moving from Region II to III across the line $a = -b$, assuming $da < 0$, $db = 0$, and

$b < -1/\tau_\ell$, Eq. 2.19 becomes

$$\text{Re}(d\lambda) = \frac{da}{1 + b\tau_\ell} > 0. \quad (2.20)$$

The real part receives a positive increment implying that points in Region III have at least one more root with positive real part than in Region II. A similar analysis of the other boundaries shows that further roots with positive real parts appear as each boundary is crossed on the line $a = 0$ moving away from Region I. Therefore, Region I is the only region with no unstable roots.

The domain of control is simply the section of Region I to the right of the line $a = 0$ as shown in Fig. 2.5. In contrast to the latency-free case, no control is

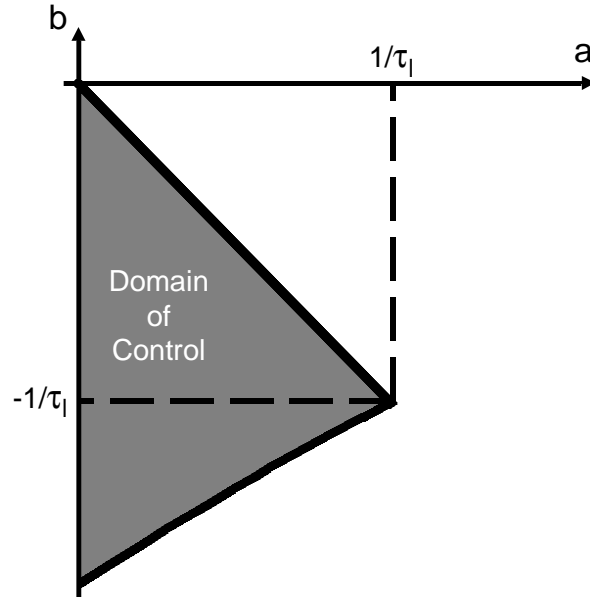


Figure 2.5: Domain of control of the first-order linear system with proportional feedback control and non-zero control loop latency. Control is only possible when latency, τ_ℓ , is less than the response time of the system, a^{-1} .

possible when $\tau_\ell < 1/a$. Control can only be achieved if the latency is shorter than the characteristic timescale of the system. This result is consistent with the intuitive argument presented above that perturbations to the system may grow too rapidly for the control response to be effective. Figure 2.5 also shows that the domain of control is of finite extent even when $\tau_\ell < 1/a$, whereas it extends indefinitely when latency is not present.

Analogous effects of control loop latency have also been found in chaos control schemes. Sukow *et al.* [49] investigated the effect of latency on control of a fast chaotic electronic circuit using two different control schemes known as *time-delay*

autosynchronization or TDAS and *extended time-delay autosynchronization* or ETDAS (an explanation of these schemes appears in the next section). In both cases, the domain of control decreased in size as the latency was increased until control was finally lost. The maximum latency at which control was attained was as much as four times larger with ETDAS than TDAS, but ETDAS control failed when the latency reached $\sim 86\%$ of the correlation time of the uncontrolled orbit even in the best case observed. Just *et al.* [50] developed an approximate prediction for the critical latency at which TDAS control fails. They predict TDAS control can be achieved when

$$\tau_\ell < \tau_P \frac{\left(1 - \frac{\nu\tau_P}{2}\right)}{\nu\tau_P}, \quad (2.21)$$

where τ_P and ν are the period and Floquet exponent (or average growth rate of perturbations) of a the UPO to be stabilized, respectively. This prediction was tested in experiments on a nonlinear electronic circuit with Rössler type behavior. Control failed experimentally when the latency reached a value $\sim 11\%$ of period of the UPO. Equation 2.21 predicted failure at $\sim 12.5\%$ of the period, in reasonable agreement with the experimental results.

2.2 Latency and Controlling Fast Chaos

The dynamical system examined in the previous section shows that control of even the simplest fixed point may fail in the presence of control-loop latency. Control engineers have contended with the problem of latency for decades [51]. Most work on this problem has focused on the properties fixed points of linear dynamical systems. For example, methods for determining stability, controllability and robustness to latency of linear systems have been developed (see Refs. [52, 53] and the references therein). In recent years, physicists have taken note of this problem as it presents a

practical limit on the application of chaos-control schemes to stabilize UPOs of fast chaotic systems. High-speed chaotic optical systems have been studied that have characteristic timescales ~ 1 ns or less [54]-[57]. The possibility of employing fast controlled or synchronized chaotic optical systems in novel communication systems [25]- [33] has enhanced the urgency of finding new techniques for dealing with latency. In this section, I will trace the evolution of fast chaos-control techniques towards controllers that require less computation in order to minimize latency.

The first technique for controlling chaotic systems was proposed by Ott, Grebogi, and Yorke [18] in 1990 and is commonly known as the OGY method. According to this method, the dynamical system to be controlled is represented by a discrete map of the form

$$\mathbf{z}_{i+1} = \mathbf{F}(\mathbf{z}_i, \mathbf{p}), \quad (2.22)$$

where \mathbf{z}_i is a vector representing the system state (*e.g.*, the current location on a surface of section in a time-delay reconstructed phase space) and p is an accessible system parameter that can be varied about a nominal value \bar{p} . The UPO to be stabilized is an unstable fixed point, denoted \mathbf{z}_* , of the uncontrolled system, *i.e.* the map $\mathbf{F}(\mathbf{z}_i, \bar{\mathbf{p}})$. Time series analysis is used to determine a linear approximation of the dynamics near the fixed point of the form

$$\mathbf{z}_{i+1} - \mathbf{z}_* = \mathbf{A}(\mathbf{z}_i - \mathbf{z}_*) + \mathbf{B}(\mathbf{p} - \bar{\mathbf{p}}), \quad (2.23)$$

where \mathbf{A} represents the system response to deviations from the fixed point of the uncontrolled system and \mathbf{B} represents the response to deviations in the parameter, p , respectively. Then feedback is implemented by varying the parameter p around a nominal value \bar{p} according to the rule

$$p - \bar{p} = -\mathbf{K}^\top [\mathbf{z}_i - \mathbf{z}_*], \quad (2.24)$$

where the matrix \mathbf{K} determines the strength of the feedback. Substituting Eq. 2.24 into Eq. 2.23, I obtain

$$\mathbf{z}_{i+1} - \mathbf{z}_* = (\mathbf{A} - \mathbf{B}\mathbf{K}^\top)(\mathbf{z}_i - \mathbf{z}_*). \quad (2.25)$$

The fixed point is stable if the eigenvalues of the matrix $\mathbf{A} - \mathbf{B}\mathbf{K}^\top$ have modulus smaller than unity. A well known technique from control engineering called *pole placement* [46] is used to determine the appropriate value of \mathbf{K} to ensure this condition is satisfied [59].

The effectiveness of the OGY method was demonstrated experimentally by Ditto *et al.* [60] who applied it successfully to a chaotic magnetoelastic ribbon in an applied AC magnetic field. A personal computer was used to perform time series analysis to obtain the necessary linear approximations and vector calculations involved in evaluating Eq. 2.24. As stated earlier, this introduced many microseconds of latency into the control loop. This was not a problem in the work of Ditto *et al.* because the characteristic timescale of the oscillations they suppressed was 0.85 seconds (the period of the applied AC field). However, such latency is a problem when the system to be controlled oscillates at frequencies above ~ 10 kHz.

An early modification of the OGY method was *occasional proportional feedback* [61]. In this scheme, a scalar state variable $z(t)$ of the dynamical system to be controlled is sampled at regular intervals to create a discrete representation of the system. If, on the i^{th} sample, the observed value of the state variable z_i falls within a window of width W centered on the value z_* , control is activated by adjusting an accessible parameter p from its nominal value \bar{p} by an amount

$$\delta p_i = \gamma (z_i - z_*), \quad (2.26)$$

where γ is the control gain. Otherwise, the parameter p is maintained at its nominal value \bar{p} . The appropriate values of the control gain γ , window size W , and center

location z_* can quickly be obtained by trial and error. The computationally costly linear fitting and vector calculations involved in the OGY method are avoided in OPF. As a result, this technique is easily implemented using analog electronics that produce a smaller latency. Roy *et al.* [62] employed the fastest implementation of OPF reported in the literature so far to stabilize chaotic oscillations of a multimode laser with characteristic frequency 118 kHz.

Myneni *et al.* [63] simplified the OPF technique to further reduce control-loop latency. In their scheme, the system state $\mathbf{Z}(t)$ (scalar or vector) is observed continuously. When the system enters a predefined window W in phase space, an accessible parameter p is perturbed from its nominal value \bar{p} by an amount δp of fixed magnitude and sign. The control perturbation is turned off when the system exits from W . The boundary and location of W are chosen so that the intersection of W and the desired UPO is zero and the transit time through W increases along the local unstable directions. As in the OPF method, the appropriate window size and location and the magnitude and sign of δp can be determined by trial and error. Myneni *et al.* implemented this scheme using high-speed electronic components on a custom printed circuit board achieving a control-loop latency of just 4.4 ns. With this controller, they successfully stabilized UPOs of a chaotic Colpitts oscillator with a characteristic frequency of 19.1 MHz.

The techniques described so far represent one line in the evolution of fast chaos controllers. A distinct line of control techniques is based on continuous feedback proportional to a past state of the system. Unlike the controllers mentioned previously, these techniques require no switching of the perturbation from one value to the next or on and off. The process of switching must be done on a much shorter time scale than the chaotic oscillations. Therefore, in principle this approach can be applied to systems that are so fast that suitable switching technology is not ex-

ist such as high-speed optical systems. In theory, at least, many of these delayed feedback techniques can even be implemented wholly in the optical domain.

The first such method was *time-delay autosynchronization* or TDAS [39]. In this method, the dynamical system of interest is subjected to continuous feedback through an accessible parameter p of the form

$$\delta p(t) = -\gamma \{z(t) - z(t - \tau_P)\}, \quad (2.27)$$

where $z(t)$ is an observed system variable, γ is the control gain, and τ is fixed a time interval. Control is achieved by setting τ equal to the period of the UPO to be stabilized and choosing an appropriate control gain. If no accurate model of the unstable system is available, the control gain and delay can simply be swept to locate suitable values. However, for situations where a model is available, there exist numerical [64] and analytical methods [65, 66] for predicting the domain of control.

Time-delay autosynchronization has been successfully applied to such diverse experimental systems as electronic circuits [67, 49], Taylor-Couette fluid flow [68], an $^{15}\text{NH}_3$ laser, and plasma instabilities [70, 71]. Sukow *et al.* [49] reported the fastest implementation of TDAS prior to the current study using it to stabilize a 10.1 MHz diode resonator. Their controller, constructed using high-frequency analog electronics, had a latency of 10 ns [38]. However, due to the computational simplicity of TDAS, much faster implementations certainly seem possible. For example, an all-optical implementation of TDAS has been proposed and successfully applied to a numerical model of a two-level laser system [73].

Some interesting generalizations of TDAS have been investigated. Just *et al.* [66] considered the possibility of using a nonlinear function $g[z(t)]$ of a system variable

to create the feedback signal

$$\delta p(t) = -\gamma \{g[z(t)] - g[z(t - \tau_P)]\} \quad (2.28)$$

in experimental situations where the variable $z(t)$ itself is not directly accessible. Nakajima and Ueda showed that for some orbits where TDAS fails control can be achieved by setting the control time delay to half the period of the orbit [74]. Socolar *et al.* [72] introduced a generalization of TDAS where more than one past state of the system is used to create the feedback signal. In this scheme, called extended time-delay autosynchronization or ETDAS, the control signal is of the form

$$\delta p(t) = -\gamma \left[z(t) - (1 - R) \sum_{k=1}^{\infty} R^{k-1} z(t - k\tau_P) \right] (z(t) - z(t - \tau_P)) \quad (2.29)$$

where $0 \leq R < 1$ determines the weight of past states in the sum. This technique has been demonstrated experimentally on electronic circuits.

In Ch. 4, I introduce a new modification of TDAS suitable to fast chaotic systems with a time delay. Many such systems are currently being studied for use in high data rate chaos-based communications systems. The following chapter describes one such system in detail. Applying control to fast time-delay systems will almost certainly mean dealing with the issue of latency. However, the current state of a time-delay dynamical system retains a memory of the state of the system one feedback delay time in the past. As a result, the past state of the system can be used to predict the current state. The modified TDAS control scheme takes advantage of this effect by delaying actuation of the control perturbation by a time equal to the feedback delay time of the system to be controlled.

Chapter 3

The Active Interferometer with Bandpass-Filtered Time-Delayed Feedback

Dynamical systems with a time-delay or memory effect can display an astonishing range of complex behavior. For example, Ikeda *et al.* [75] studied a passive optical resonator described by the equation

$$\dot{x}(t) = -x(t) + \mu \sin [x(t - t_R)], \quad (3.1)$$

where μ and t_R are the strength of nonlinearity and the time-delay, respectively. With no time-delay ($t_R = 0$) this one dimensional dynamical system is limited to simple fixed-point dynamics. However, when $t_R \gg 1$ this system can exhibit multi-stability and high-dimensional chaos [40]. Such complex time-delay dynamics arise in many physical, biological, chemical, and engineering models [52], [76]-[78]. Optical time-delay systems, in particular, have been a subject of continued interest over the past two decades. Besides the passive optical resonator [40, 76] mentioned above, other important systems include semiconductor lasers with optical or electro-optical feedback [79]- [81], CO₂ lasers with delayed feedback via an intracavity electro-optic modulator [82, 83], and electro-optic hybrid devices with delayed feedback [34].

More recently, the possibility of chaos-based technology has sparked interest in fast chaotic optical time-delay systems. Proposed technological applications of such systems include dynamic memory [34], dynamics-based computation [36, 37], and communications [25]-[33]. In each of these applications, high-speed chaotic fluctuations are needed to facilitate rapid processing or transfer of information. For

example, chaos-based secure communication at 250 Mbit/s has been achieved using an erbium-doped fiber ring laser (EDFL) as a source of picosecond chaotic oscillations [29]. The complexity of time-delay dynamical systems may also be an advantage in these applications. Research on the security of chaos-based communication schemes indicates high-dimensional dynamics are necessary to ensure that nonlinear forecasting techniques cannot be used by an eavesdropper to extract a message from the chaotic carrier [88]- [90].

In this chapter, I introduce a new fast chaotic time-delay dynamical system as a flexible, inexpensive source of fast optical chaos. Both the timescale and the complexity of the dynamics are easily tuneable. Compared to other time-delay optical system such as the EDFL mentioned above, this system is constructed with inexpensive, readily accessible components. These characteristics make it an attractive experimental system for studying time-delay dynamics and control. In the next chapter, the device will serve as a testbed for a new chaos control method.

Figure 3.1 shows a schematic diagram of the device. Light emitted from a laser interferometer falls on a photodiode. The electrical signal from the diode is amplified, propagates through a long coaxial cable, and is used to modulate the injection current of the laser. The propagation time through the cable is long compared to the response time of the laser interferometer itself. The nonlinearity of the interferometer coupled with the delay in the feedback loop combine to produce a range of steady state, periodic, and chaotic behavior.

This new device has some important differences with previous optical time-delay systems. First, Ohtsubo *et al.* [85]- [43] studied an active interferometer with electronic feedback, but used low frequency limiting the oscillation frequency to tens of kilohertz. In my system, the high-frequency electronic feedback signal is applied to a semiconductor laser through a radio-frequency device called a *bias-T*

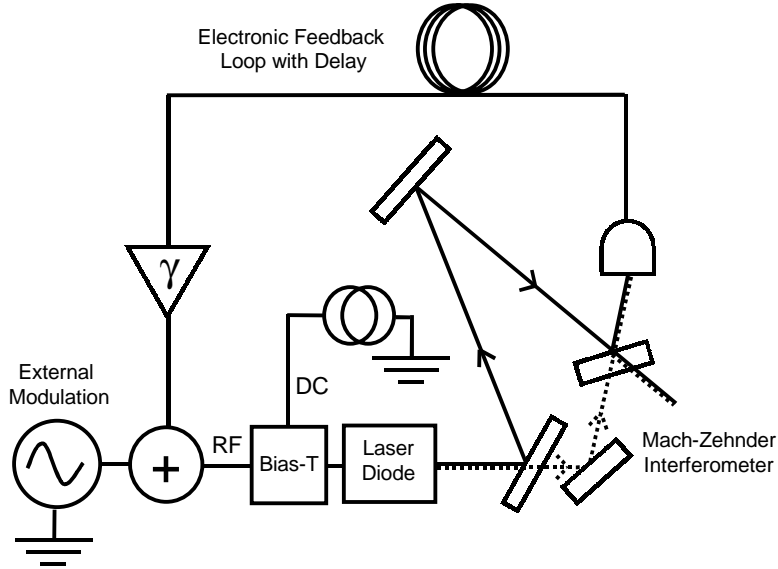


Figure 3.1: Schematic of active interferometer with delayed band-pass filtered electronic feedback. The device produces chaotic oscillations on nanosecond timescales.

allowing me to achieve >100 MHz oscillations. Using state of the art technologies, 10-100 GHz frequencies should be attainable. Second, the low-frequency electronics in Ohtsubo's system produced a low pass characteristic in the feedback loop. In contrast, the bias-T used in my system produces a bandpass characteristic in the feedback loop blocking any DC component from circulating. The dynamics of time-delay systems with band-pass filtered feedback is a largely unexplored topic. However, it is of increasing importance for fast chaos applications since many high speed opto-electronic devices are AC-coupled. Two interesting results that have been reported are the use of bandpass filtering to tailor the spectrum of the chaotic signal to fit a desired communication band and the observation of apparently very high-dimensional chaos [44, 87].

In Sec. 3.1, I describe the experimental system. In Sec. 3.2, I develop a theoretical model of the active laser interferometer with bandpass feedback. In Sec. 3.3, I describe the measurements necessary to determine the parameters of the model. In Sec. 3.4, the dynamics of this new system are explored through a survey of the route to chaos. Section 3.5 describes this effect of external modulation on the system. In Sec. 5.3 I discuss the issues involved in scaling the system to run at faster speeds, a necessity for use in a real communication system.

3.1 Experimental Apparatus

In this section I describe my experimental implementation of the active interferometer with bandpass-filtered delayed feedback. The light source is a $0.65\ \mu\text{m}$ wavelength AlGaInP diode laser (Hitachi HL6501MG) with a multi-quantum well structure. The diode is housed in a commercial mount (Thorlabs TCLDM9) equipped with a bias-T for adding an RF component to the injection current, and temperature regulation circuitry. Thermoelectric coolers connected to a proportional-integral-derivative feedback controller (Thorlabs TEC2000) provide 1 mK temperature stability, minimizing frequency and power drift due to heating effects. The light generated by the laser is collimated by a (Thorlabs C230TM-B, $f=4.5\text{mm}$) lens, producing an elliptical beam ($1\text{ mm} \times 5\text{ mm}$) with a maximum output power of 35 mW at the maximum operating current of 90 mA.

The laser beam is directed into a Mach-Zehnder interferometer. The interferometer contains two paths for the light to follow whose lengths differ by 45 cm. A Si photodetector (Hamamatsu S4751, 750 MHz bandwidth) measures the intensity of light emerging from the interferometer. The sensitive area of the photodiode is much smaller than the cross sectional area of the laser beam so only a fraction of the interferometer's output is detected. The size of the detector is actually an

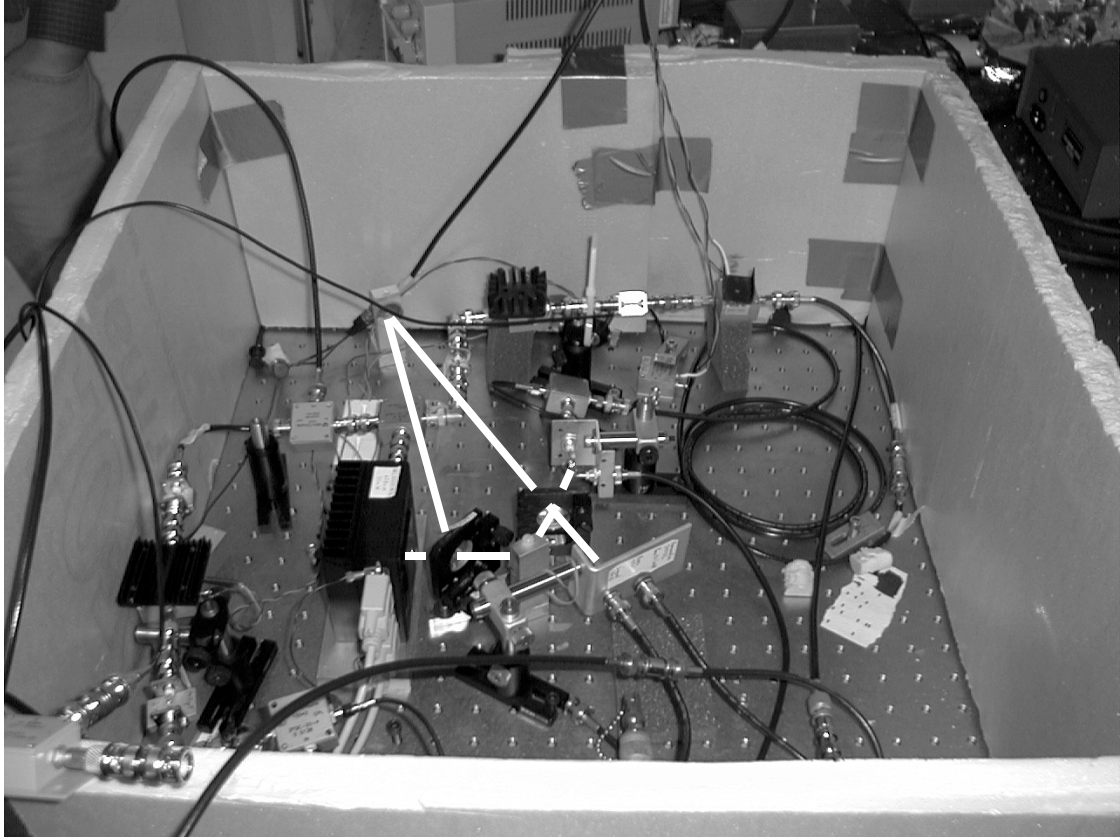


Figure 3.2: Photograph of the experimental apparatus. The black box left of center is the laser housing. The path of the laser beam is highlighted by the thick white line. The coil of coax cable to the right of center is the delay line.

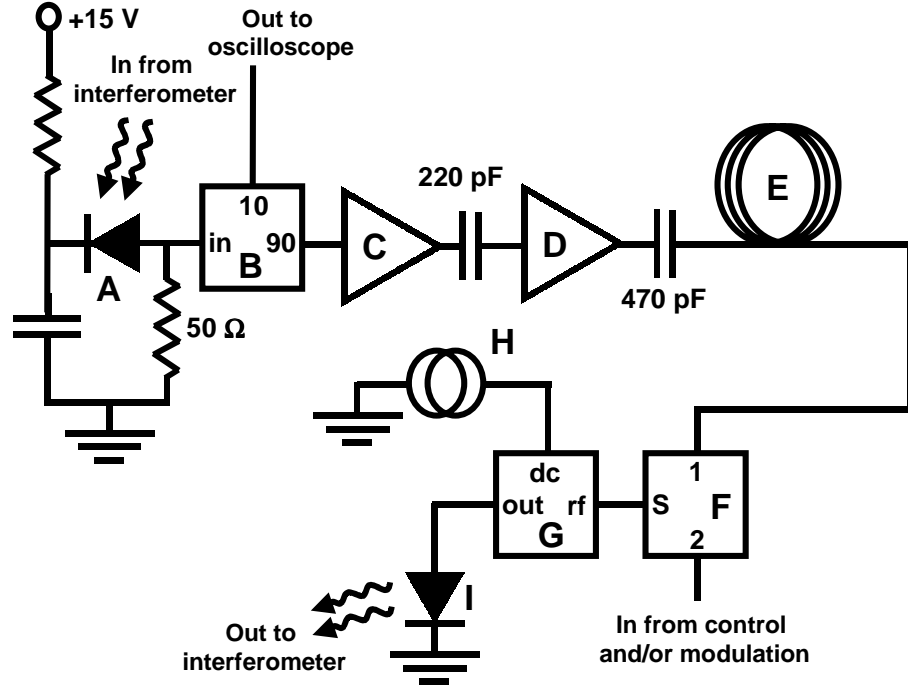


Figure 3.3: Schematic diagram of the electronic feedback loop including the photodiode and laser. The components labelled A-I are as follows: A - Hamamatsu silicon photodiode S4751; B - MiniCircuits directional coupler ZFDC-20-4; C - MiniCircuits amplifier ZFL-1000L; D - MiniCircuits amplifier ZFL-1000GH; E - Coaxial cable RG 58/U; F - MiniCircuits power combiner ZFSC-2-1W-75; G - bias-T in Thorlabs laser mount TCLDM9; H - Thorlabs laser diode controller LDC-500; I - Hitachi laser diode HL6501MG.

advantage since, due to aberrations and finite precision in alignment, more than one fringe appears within the beam cross section. The limited aperture allows a more spatially uniform field to fall on the detector, producing better fringe visibility. A neutral density filter is used to reduce the optical power reaching the photodiodes to avoid saturation.

The electronic feedback loop which begins with the photodiode and ends back at the laser is shown schematically in Fig. 3.3. The part numbers of the components are given in the figure caption. The photodiode (labelled A in Fig. 3.3) produces a

current proportional to the optical power falling on its surface, which is converted into a current using a $50\ \Omega$ resistor. The voltage across this resistor is transmitted down a coaxial cable (RU 58). One percent of the signal power is split off by a directional coupler (B in Fig. 3.3) and sent to a fast oscilloscope or spectrum analyzer to monitor the state of the system. The signal propagating down the main line next reaches a low-noise, fixed-gain amplifier (C in Fig. 3.3), a DC-blocking capacitor (220 pF), a variable gain amplifier (D in Fig. 3.3), and a second DC-blocking capacitor (470 pF). The capacitors serve as high pass filters to reduce the loop gain at frequencies below 10 MHz where a thermal effect enhances the laser's sensitivity to frequency modulation. A power splitter/combiner (labelled F in 3.3) combines the feedback signal with any external modulation or control signal that is present and the resulting voltage is applied to the bias-T input on the laser mount. The bias-T (G in Fig. 3.3) converts the signal into a current and adds it to a DC component from a commercial laser driver (H in Fig. 3.3) to form the laser's injection current.

The entire system is fixed on an optical table using short (2 inch) mounts for mechanical stability. This stability is extremely important as variation in the path length on the order of the the wavelength of the laser light ($0.65\ \mu\text{m}$) produces significant power variations at the output of the interferometer. Furthermore, the entire apparatus is covered by an insulating box to reduce thermal expansion or contraction of the mirror mounts due to air currents.

3.2 Mathematical Model

In this section, I develop a mathematical model of the active laser interferometer with delayed bandpass feedback. The device consists of three main components: a semiconductor laser that provides linear electro-optical conversion, a Mach-Zehnder

interferometer that provides nonlinearity, and an electronic feedback loop that provides time delay and bandpass filtering. I consider each of these components in a separate subsection. A block diagram appears at the top of each subsection to highlight the component to be discussed. I combine the component models to arrive at a mathematical model of the full experimental system. I do not include external modulation in this section. In Sec. 3.5, the model is extended to include modulation by a driving voltage.

3.2.1 The Semiconductor Laser

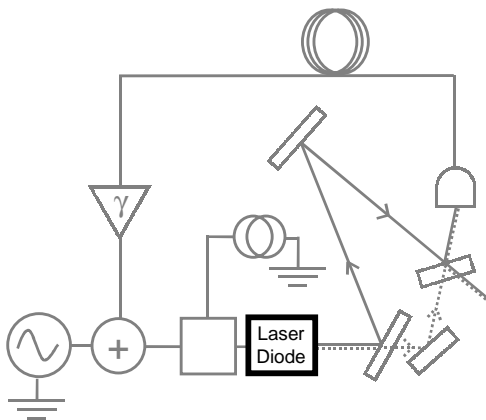


Figure 3.4: The first component of the active interferometer with delayed bandpass feedback: The semiconductor laser. The laser provides linear conversion of changes in the injection current to changes in the optical power and frequency.

The light source in the active laser interferometer is a semiconductor laser. Invented in 1962 [97]-[100], the semiconductor laser (or laser diode) has since become a key component of optical telecommunications systems. Reasons for its suitability include its compact size (relative to other lasers) and the fact that its power can be directly modulated through variation of the injection current [95]. These features

also make it suitable for my purposes.

Most types of laser involve three basic elements: a pumping mechanism, a gain medium, and a resonator. The pumping mechanism adds energy to the gain medium, maintaining it in an excited state (*i.e.*, a population inversion). Photons propagating through the excited medium stimulate coherent emission of more photons. The resonator ensures that each photon passes several times through the gain medium, and is thereby amplified many times before escaping. Light leaves the resonator in the form of an intense, coherent beam.

All three of these elements are present in a diode laser. The laser is essentially a semiconductor p-n junction (or *homojunction*). Light is emitted when electrons and holes recombine in the depletion region of the junction which constitutes the gain medium. The pumping mechanism is an injected current that produces electron-hole pairs. Two cleaved facets of the semiconductor crystal form a Fabry-Perot resonator. A schematic drawing of a homojunction diode laser is shown in Fig. 3.5(a). Modern laser diodes differ from simple p-n junctions because additional layers of n-type or p-type are added (forming a *heterojunction*) to confine the injected current to the *active region*. The various layers each have a different index of refraction and conveniently constitute a dielectric waveguide that confines the optical field to the gain region. The entire sandwich of semiconductor layers is referred to as a *heterostructure*. One type of GaAlAs heterostructure is shown in Fig. 3.5(b). If the width of the active layer is comparable the DeBroglie wavelength of the electrons (~ 10 nm), carrier motion normal to the active layer is confined to a quantum well. So called *quantum well lasers* tend to have high gain at lower current densities. The diode used in my interferometer is a multi-quantum well laser.

The dynamical behavior of a semiconductor laser can be modelled by rate equations, a set of first-order differential equations that describe the evolution of the

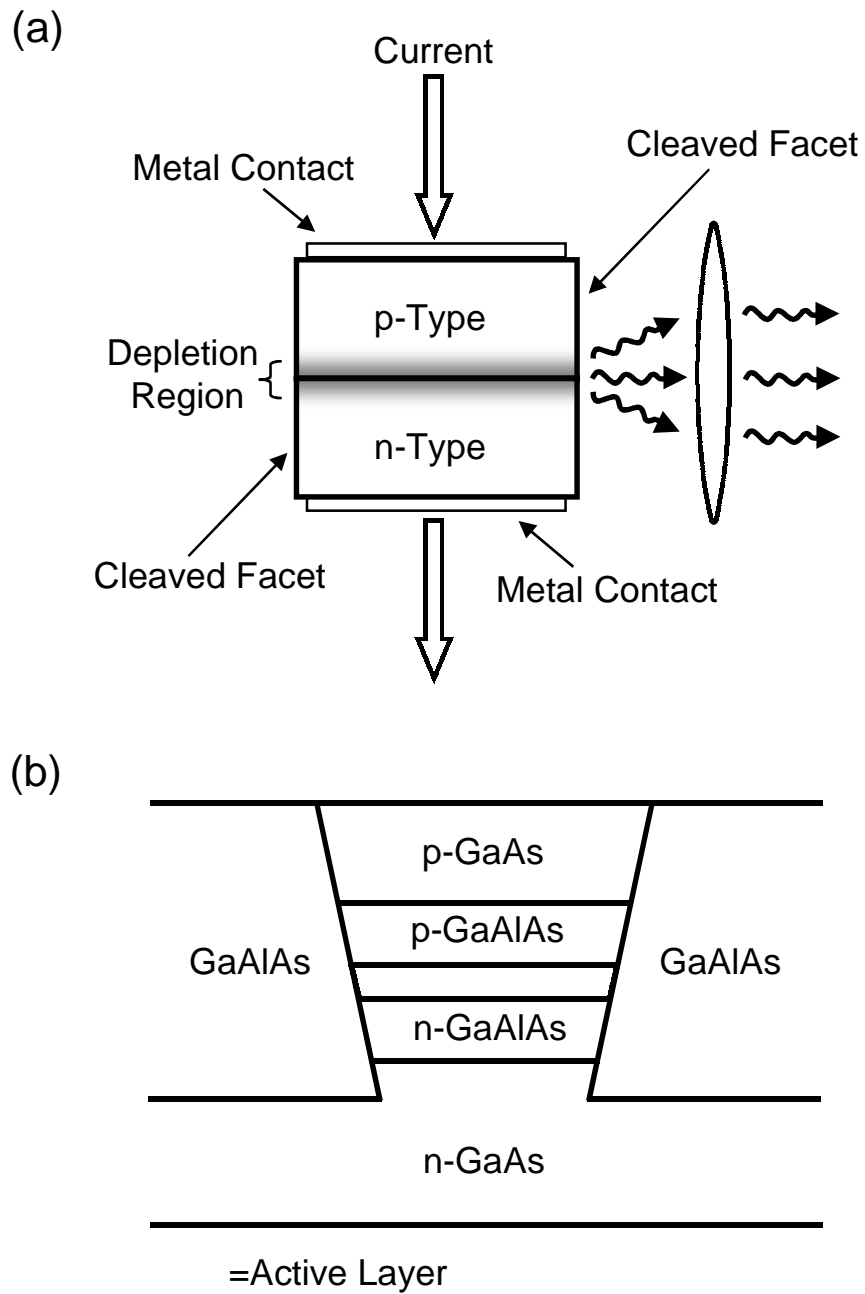


Figure 3.5: (a) Simplified schematic of a semiconductor laser. (b) Schematic of a typical “buried heterostructure” laser. Cladding layers provide both carrier confinement and lateral optical waveguiding.

optical field and carrier density. The dynamics of a single-mode double heterostructure semiconductor laser is described by [95, 96]

$$\dot{S} = (G - \gamma) S + R_{sp}, \quad (3.2)$$

$$\dot{N} = \frac{I}{q} - \gamma_e N - GS, \quad (3.3)$$

$$\dot{\phi} = -\frac{\bar{\mu}}{\mu_g} (\omega_0 - \Omega) + \frac{1}{2} \beta_c (G - \gamma), \quad (3.4)$$

where S and N are the number of photons and carriers, respectively, in the active layer, ϕ is the phase of the optical field, and I is the injection current. The gain G is a function of both the photon and carrier numbers, and the spontaneous emission rate R_{sp} is a function of the carrier number. The loss due to absorption or transmission through the reflective facets is denoted by γ , q is the charge of an electron, γ_e is the rate of non-radiative recombination of electron-hole pairs, $\bar{\mu}$ is the effective index of refraction for the lasing Fabry-Perot mode, μ_g is the group refractive index, $\omega_0/2\pi$ is the steady state optical frequency, Ω is the cavity resonance frequency, and β_c is the linewidth enhancement factor. The optical frequency of the laser is

$$\nu = \frac{1}{2\pi} (\omega_0 + \dot{\phi}). \quad (3.5)$$

Equations 3.2-3.4 constitute a detailed model of the semiconductor laser. However, they contain numerous parameters that are difficult to determine empirically from a commercially packaged laser. Also, they do not accurately describe the effects of injection current modulation because they do not include package and chip-related impedances that tend to shunt current around the active layer [94]. Fortunately, the full rate equation model is not always necessary. When the injection current I is fixed, the rate equations display a steady state. Below a threshold current value

I_{th} , the steady state power is nearly zero (except for a small contribution from spontaneous emission). Above threshold, the steady state power is linearly proportional to the injection current. The laser approaches the steady state from an arbitrary initial condition via damped oscillations with a damping rate Γ_R . The frequency of these oscillations, denoted by Ω_R , is known as the *relaxation oscillation frequency*. Typically, $\Omega_R/2\pi \sim \Gamma_R \sim 2$ GHz. A simpler model of the semiconductor laser is applicable when the injection current is modulated at frequencies well below Ω_R , as described below.

Agrawal and Dutta [95] show that the optical power and phase respond sinusoidally when the injection current is weakly modulated around a constant value such that $I(t) = I_{DC} + \delta I \sin(\omega_m t)$. The amplitude δS and phase θ_S of the photon number fluctuation are given by

$$\delta S = \frac{G_N S}{q (\Omega_R^2 + \Gamma_R^2) \sqrt{1 + \frac{\omega_m^4}{(\Omega_R^2 + \Gamma_R^2)^2} + \left(\frac{4\Gamma_R^2}{(\Omega_R^2 + \Gamma_R^2)} - 2 \right) \frac{\omega_m^2}{(\Omega_R^2 + \Gamma_R^2)}}} \delta I, \quad (3.6)$$

$$\theta_S = \tan^{-1} \left(\frac{-2\Gamma_R \omega_m}{(\Omega_R^2 + \Gamma_R^2)} \frac{1}{\left(1 - \frac{\omega_m^2}{(\Omega_R^2 + \Gamma_R^2)} \right)} \right) \quad (3.7)$$

where S is the steady state power and $G_N = \partial G / \partial N$. Note that these expressions reduce to

$$\delta S \simeq \frac{G_N S}{q (\Omega_R^2 + \Gamma_R^2)} \delta I, \quad (3.8)$$

$$\theta_S \simeq \frac{-2\Gamma_R}{(\Omega_R^2 + \Gamma_R^2)} \omega_m \sim \left(-10^{-2} \frac{\text{rad}}{100 \text{ MHz}} \right) \frac{\omega_m}{2\pi}. \quad (3.9)$$

in the limit where $\omega_m \ll \sqrt{\Omega_R^2 + \Gamma_R^2}$. Thus, if the modulation frequency is small enough compared to the relaxation oscillation frequency, the laser's optical power varies linearly with the injection current and with no phase lag. A

similar result holds for the optical phase. Agrawal and Dutta give the phase response to current modulation in terms of the resulting change in optical frequency $\delta\nu(t) = \delta\nu_0 \sin(\omega_m t + \theta_c)$, where

$$\delta\nu_0 = \delta I \frac{\beta_c G_N}{4\pi q} \sqrt{\frac{\omega_m^2 + \Gamma_P^2}{(\Omega_R^2 + \Gamma_R^2)^2 \left(\left(1 - \frac{\omega_m^2}{\Omega_R^2 + \Gamma_R^2}\right)^2 + \frac{4\Gamma_R^2}{(\Omega_R^2 + \Gamma_R^2)} \frac{\omega_m^2}{(\Omega_R^2 + \Gamma_R^2)} \right)}}, \quad (3.10)$$

$$\theta_c = \tan^{-1} \left(\frac{\omega_m}{\Gamma_P} \right) + \tan^{-1} \left(\frac{-2\Gamma_R \omega_m}{(\Omega_R^2 + \Gamma_R^2) \left(1 - \frac{\omega_m^2}{(\Omega_R^2 + \Gamma_R^2)}\right)} \right), \quad (3.11)$$

where

$$\Gamma_P = \frac{R_{sp}}{S} - S \frac{\partial G}{\partial P} \sim 2 \text{ GHz}. \quad (3.12)$$

In the limit where $\omega_m \ll \sqrt{\Omega_R^2 + \Gamma_R^2}$, these equations reduce approximately to

$$\delta\nu_0 = \frac{\beta_c G_N}{4\pi q} \frac{\Gamma_P}{(\Omega_R^2 + \Gamma_R^2)} \delta I \quad (3.13)$$

$$\theta_c = \left(\frac{1}{\Gamma_P} - \frac{-2\Gamma_R}{(\Omega_R^2 + \Gamma_R^2)} \right) \omega_m \sim \left(0.3 \frac{\text{rad}}{100 \text{ MHz}} \right) \frac{\omega_m}{2\pi}. \quad (3.14)$$

Thus, if the current is modulated slowly enough, the laser may be viewed as a simple linear current-power and current-frequency transducer.

To ensure that the system remains in the regime of slow modulation, I determine the relaxation oscillation frequency experimentally. I take advantage of the well known fact that the power spectrum of the intensity noise of a diode laser is strongly peaked around the relaxation oscillation frequency [95]. With the laser emitting in a steady state, the intensity noise is detected by a fast photodiode (New Focus 1580-B, 12 GHz bandwidth). The frequency content of the signal from the detector is visualized using a high-speed spectrum analyzer (Hewlett-Packard 8566B, 22 GHz

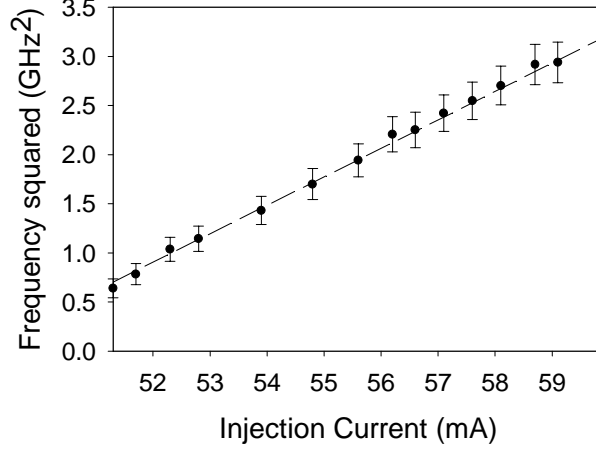


Figure 3.6: Square of relaxation oscillation frequency as a function of injection current. By operating with a large DC injection current, I ensure that the laser is never modulated at frequencies near the relaxation oscillation.

bandwidth). The location of the peak in the spectrum is recorded as the injection current of the laser is varied. Figure 3.6 shows the result. The experimental data reflect the well-established relation [95]

$$\Omega_R^2 \propto i - i_{th}. \quad (3.15)$$

Based on the slope obtained from a least squares fit, I determine the relaxation oscillation frequency at the operating current of 74 mA used in the experiments is 2.7 GHz, much higher than the bandwidth of several of the components in the electronic feedback loop. Thus, it may be safely assumed that the laser is never modulated at a rate close to the relaxation oscillation frequency.

Based on the results of the preceeding paragraphs, I approximate the laser's behavior as

$$P = \sigma (I - I_{th}) = \sigma (I_{AC} + I_{DC} - I_{th}), \quad (3.16)$$

$$\nu = \eta (I - I_{th}) = \eta (I_{AC} + I_{DC} - I_{th}), \quad (3.17)$$

where P is the total optical power emitted by the laser diode, and σ and η are empirically determined constants. The injection current I is the sum of a constant bias current I_{DC} and a small fluctuating current I_{AC} . For convenience, the constant terms can be lumped to obtain

$$P = \sigma I_{AC} + P_0, \quad (3.18)$$

$$\nu = \eta I_{AC} + \nu_0, \quad (3.19)$$

where $P_0 = \sigma (I_{DC} - I_{th})$ and $\nu_0 = \eta (I_{DC} - I_{th})$. Since both quantities are linear functions of I_{AC} , the frequency can be expressed as a function of the output power

$$\nu = \frac{\eta}{\sigma} (P - P_0) + \nu_0. \quad (3.20)$$

Equations 3.18 and 3.20 constitute a more practical model of the semiconductor laser because they contain only a few parameters, all of which are experimentally accessible. This model inherits two weaknesses from the rate equation model from which it was derived. First, the rate equation model only includes one mechanism for frequency modulation, *i.e.* variation of the carrier number. In reality, there is a second physical process that produces frequency modulation when the injection current is varied. That process is a thermal effect that enhances frequency modulation below 10 MHz by as much as a few orders of magnitude [91, 92, 96]. As mentioned earlier, the capacitors in the feedback loop in the active laser interferometer introduces greater loss at low frequencies to counteract this effect. Therefore, I do not account for the thermal effect explicitly in my model. However, care must be taken in measuring the constant η as it will have a different value below 10 MHz than above.

The second weakness of this model is that it neglects the important physical phenomenon of phase noise. Due to spontaneous recombination in the active region,

the phase of the electric field is subject to discontinuous jumps [95]. As a result, the frequency of the laser fluctuates somewhat around the value predicted by the deterministic model. The effect of the interferometer on this phase noise is discussed in the next subsection.

3.2.2 The Mach-Zehnder Interferometer

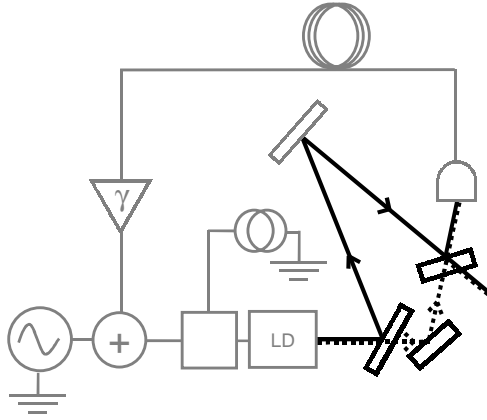


Figure 3.7: The second component of the active interferometer with delayed band-pass feedback: The Mach-Zehnder interferometer. The interferometer provides the nonlinearity needed to obtain chaos.

The coherent light waves light emitted by the diode laser are directed into an interferometer. As will be shown below, the interferometer outputs a beam whose intensity is a nonlinear function of the input optical power and frequency. Thus, this component provides nonlinearity to the system, a necessary property for producing complex dynamics. In this subsection, I explain the principle of operation of the Mach-Zehnder interferometer in detail.

A Mach-Zehnder interferometer takes a single laser beam as input, splits it into equal intensity beams that travel in separate arms, and recombines them after they

travel different distances (see Fig. 3.8(a)). To model this process, I assume the input field is of the form

$$E_{in}(x, y, z, t) = E(y, z)e^{-i(\omega t - kx)}, \quad (3.21)$$

with optical frequency $\nu = \omega/2\pi$ and intensity

$$I_{in} = \frac{c\epsilon_0}{2}E^2, \quad (3.22)$$

where c is the speed of light and ϵ_0 is the permittivity of free space. Since there are two 50-50 beam splitters (labelled BS1 and BS2 in Fig. 3.8(a)) in the system, there are actually four separate beam paths, as shown in Fig. 3.8(b). Two of these paths meet at each output. Reflection from each air-to-glass interface adds a π phase shift to the electric field. Note that the reflection in path 4 at BS2 is at a glass-to-air interface so no phase shift occurs. Paths 1 and 3 are longer than paths 2 and 4 by a distance $l = c\Delta$ where Δ is the difference in propagation time through the two arms of the interferometer. The electric fields following each path can then be expressed as

$$E_1(x, y, z, t) = -\frac{1}{2}E(y, z)e^{-i(\omega t - k(x-l))}, \quad (3.23)$$

$$E_2(x, y, z, t) = -\frac{1}{2}E(y, z)e^{-i(\omega t - kx)}, \quad (3.24)$$

$$E_3(x, y, z, t) = \frac{1}{2}E(y, z)e^{-i(\omega t - k(x-l))}, \quad (3.25)$$

$$E_4(x, y, z, t) = -\frac{1}{2}E(y, z)e^{-i(\omega t - kx)}, \quad (3.26)$$

where, E_i is the field that follows path i . The intensity at either output is the coherent combination of the fields associated with the two paths that reach it.

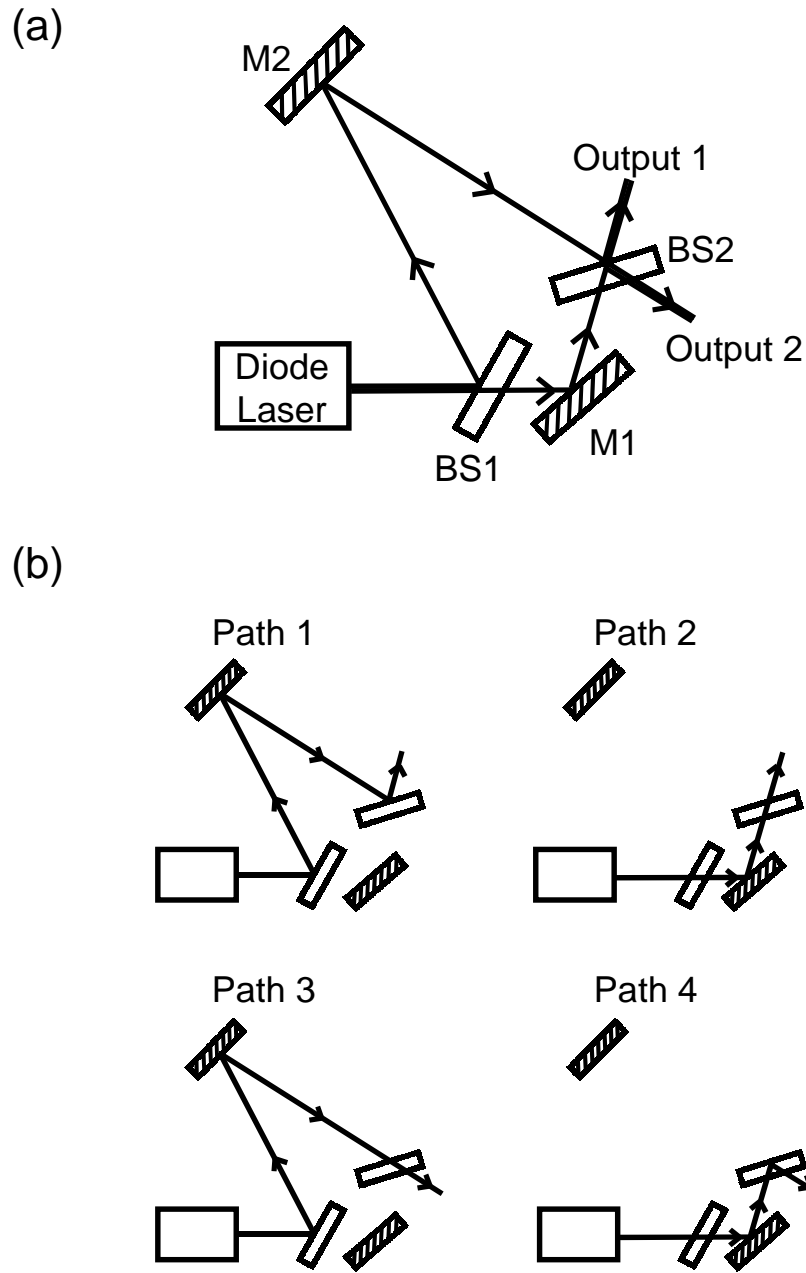


Figure 3.8: (a) Schematic of a Mach-Zehnder interferometer with unequal optical path lengths. (b) There are four separate paths through the interferometer. At each output port, the beams from two paths combine and interfere.

Fields E_1 and E_2 are combined at output 1 so the intensity at output 1 is

$$I_1 = \frac{c\epsilon_0}{2} |E_1 + E_2|^2, \quad (3.27)$$

$$= \frac{c\epsilon_0}{2} E^2 \left[\frac{1}{2} + \frac{1}{4} \left(e^{-i(\omega t - k(x-l))} e^{i(\omega t - kx)} + e^{-i(\omega t - kx)} e^{i(\omega t - k(x-l))} \right) \right], \quad (3.28)$$

$$= \frac{c\epsilon_0}{4} E^2 [1 + \cos(kl)], \quad (3.29)$$

$$= \frac{I_{in}}{2} [1 + \cos(\omega\Delta)], \quad (3.30)$$

where I have used $k = c\omega$ and $kl = k(c\Delta) = \omega\Delta$. The fields E_3 and E_4 are combined at output 2 giving an intensity

$$I_2 = \frac{c\epsilon_0}{2} |E_3 + E_4|^2, \quad (3.31)$$

$$= \frac{c\epsilon_0}{2} E^2 \left[\frac{1}{2} - \frac{1}{4} \left(e^{-i(\omega t - k(x-l))} e^{i(\omega t - kx)} + e^{-i(\omega t - kx)} e^{i(\omega t - k(x-l))} \right) \right], \quad (3.32)$$

$$= \frac{c\epsilon_0}{4} E^2 [1 - \cos(kl)], \quad (3.33)$$

$$= \frac{I_{in}}{2} [1 - \cos(\omega\Delta)]. \quad (3.34)$$

This model of the interferometer can be connected to the model of the diode laser since it is the source of the input intensity I_{in} . In the laser model, the output light is described in terms of the optical power emitted. The optical power P and intensity $I(x, y)$ of the light emitted by the laser are related by

$$P = \iint I dx dy, \quad (3.35)$$

where the integration is performed over the elliptical cross section of the laser beam. The important feature of Eq. 3.35 is the proportionality between P and I . This result, together with Eqs. 3.30 and 3.34, implies

$$P_1 = \frac{\zeta_F}{2} P [1 + \cos(\omega\Delta)], \quad (3.36)$$

$$P_2 = \frac{\zeta_F}{2} P [1 - \cos(\omega\Delta)], \quad (3.37)$$

where I have included the factor ζ_F to account for absorption by the neutral density filter between the laser and the interferometer.

Equation 3.20 relates the optical frequency ν of the laser to the optical power P . Thus, with a laser diode as the light source, the outputs of the interferometer are

$$\begin{aligned} P_1 &= \frac{\zeta_F}{2} P \{1 + \cos[\alpha(P - P_0) + \phi]\}, \\ P_2 &= \frac{\zeta_F}{2} P \{1 - \cos[\alpha(P - P_0) + \phi]\}, \end{aligned} \quad (3.38)$$

where $\alpha = 2\pi\Delta\eta/\sigma$ and $\phi = 2\pi\Delta\eta/\sigma\nu_0$. The constant offset ϕ of the argument to the cosine can be tuned by varying the DC component of the injection current. I choose to set this value to $m\pi$ where m is an even integer. If $\phi = -\pi/2$,

$$P_1 = \frac{\zeta_F}{2} P \{1 + \sin[\alpha(P - P_0)]\}, \quad (3.39)$$

$$P_2 = \frac{\zeta_F}{2} P \{1 - \sin[\alpha(P - P_0)]\}. \quad (3.40)$$

Choosing the opposite sign of ϕ simply flips the sign of the cosine terms. The constant parameter α determines the sensitivity of the interferometer and can be tuned by varying the path imbalance Δ . With a large value of α , the interferometer will amplify small fluctuations.

Up to this point, I have assumed the light waves in the interferometer are perfect plane waves and that the beamsplitters divide them exactly in half. In reality, neither of these conditions are strictly true. Curvature of the wavefronts produces variation in the degree of interference across the beamwidth. Typically, the interference pattern is a set of curved stripes. Careful alignment of the interferometer makes the stripes thicken until only a couple are visible over the beam width. However, the ideal of a uniform field is not experimentally attainable. Likewise, since

the beamsplitters are not perfect 50-50 splitters, the waves in each arm have different amplitudes so one wave cannot completely cancel out each the other. Both of these effects tend to reduce the visibility b of the fringes defined as

$$b \equiv \frac{P_{\max} - P_{\min}}{P_{\max} + P_{\min}}. \quad (3.41)$$

I account for this effect by adding a parameter to Eqs. 3.39 and 3.40 that reduces the visibility. Specifically,

$$P_1 = \frac{\zeta_F}{2} P \{1 + b \sin [\alpha (P - P_0)]\}, \quad (3.42)$$

$$P_2 = \frac{\zeta_F}{2} P \{1 - b \sin [\alpha (P - P_0)]\}. \quad (3.43)$$

Equations 3.42, 3.43, and 3.18 constitute a practical model of the laser and interferometer. Before proceeding to model the feedback loop, several caveats must be noted. First, since the interferometer sensitivity α is directly proportional to the path imbalance, at first glance it appears that α can be set to an arbitrarily large value. Unfortunately, the interferometer also amplifies phase noise in the laser field. To see why, assume that the phase noise can be modelled by adding a stochastic term $\xi(t)$ to Eq. 3.20 giving

$$\nu = \frac{\eta}{\sigma} [(P - P_0) + \nu_0 + \xi(t)]. \quad (3.44)$$

The output of the interferometer is then

$$P_1 = \frac{\zeta_F}{2} P \{1 + \cos [\alpha (P - P_0) + \alpha \xi(t) + \phi]\}. \quad (3.45)$$

Increasing the sensitivity of the interferometer proportionally increases the effect of phase noise. Thus there is a tradeoff between sensitivity and noise. Experimentally, I chose to set the sensitivity to a value such that amplitude of noise fluctuations is

roughly less than 10% of P_0 . This amount of noise may be large enough to have a significant effect on the dynamics of the system.

Second, I have assumed that the light waves reaching one output through two different paths have the same optical frequency. This assumption is reliable as long as the optical frequency is not modulated significantly in a period of time comparable to Δ , the difference in propagation times through the two paths being combined. The path difference in my interferometer is ~ 45 cm making the difference in propagation times ~ 1.5 ns. Oscillations in the system at frequencies comparable to or greater than $1/(1.5 \text{ ns})$ or 670 MHz cannot be explained by this model. In order to scale this device to higher frequencies, either the path difference must be shortened or a new model must be developed.

Third, due to aberrations in the wavefronts and finite precision in aligning the optical components making up the interferometer, the width of the interference fringes is less than the width of the laser beam itself, resulting in some spatial variation in intensity over a cross section of the beam emerging from the interferometer. Typically, about two fringes fit within the beam width. However, the output of the interferometer is detected by a photodiode whose active region is much smaller than the beam width so only a single fringe is observed. As a result, since much of the beam is clipped, only a fraction of the power is detected.

Fourth, many types of interferometer exist, *e.g.* the well-known Michelson interferometer, that could be used as the nonlinear element in this system. I chose to use a Mach-Zehnder interferometer because the components are arranged in such a way that no light is reflected back into the laser cavity. Such back reflections are a common cause of instability in diode lasers [80]. Ohtsubo *et al.* [43] investigated a similar interferometer-based device but used a Twyman-Green interferometer to provide nonlinearity. As a result, they had to include an expensive optical isolator

in order to guard against instabilities induced by back reflections.

The light exiting output 1 of the interferometer falls on a photodiode that converts the optical signal into an electronic signal. This signal propagates through the electronic feedback loop which is the subject of the next subsection.

3.2.3 The Electronic Feedback Loop

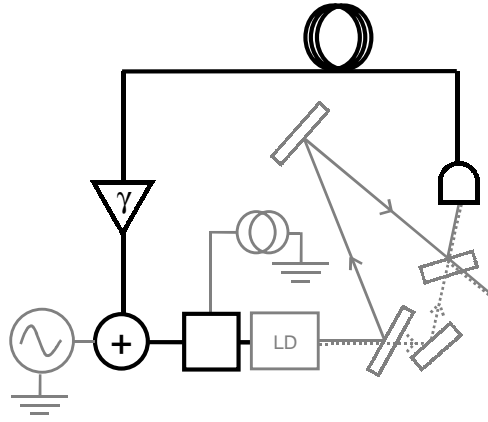


Figure 3.9: The third component of the active interferometer with delayed band-pass feedback: The electronic feedback loop. Time delay and bandpass filtering are produced by the feedback loop.

The electronic feedback loop converts the optical intensity emitted by the interferometer into an electrical signal and, after a delay period, modulates that signal onto the injection current of the diode laser. The loop contains several linear elements with amplification, attenuation, and filtering characteristics. High-pass filtering is provided by the two capacitors and the bias-T. Low-pass filtering is provided by the limited bandwidth of the photodiode, diode laser, and the electrical connections to the laser. As was the case with semiconductor laser, developing a first principles model of the feedback loop requires significant complexity and

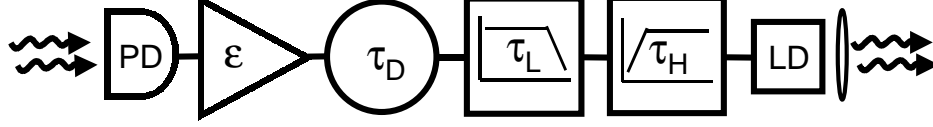


Figure 3.10: Block diagram of feedback loop. Light from the interferometer is converted into an electrical signal by the photodiode (PD). All electrical components are lumped into one amplifier with gain γ , one low-pass filter with time constant τ_L , one high-pass filter with time constant τ_H , and a time delay of τ_D . Finally, the electrical signal is converted back into light by the laser diode (LD).

knowledge of parameters that are difficult to obtain empirically from commercial devices such as the bias-T and laser mount. Therefore, I will again develop a highly simplified but practical model. I will assume the amplification, attenuation, and filtering of the various of the components of the feedback loop can be lumped into one single-pole low-pass filter, one-single pole high-pass filter, and one amplifier.

Figure 3.10 shows a block diagram of the lumped model. Light from the interferometer falls on the detector (PD in Fig. 3.10) producing a current proportional to the incident intensity. Based on the interferometer response given in Eq. 3.42, the photocurrent is

$$i_{\text{det}}(t) = \frac{\rho \zeta_C \zeta_F}{2} P(t) \{1 + b \sin [\alpha (P(t) - P_0)]\}, \quad (3.46)$$

where ρ is the sensitivity of the photodiode and ζ_C is the fraction of the power in the laser beam that actually falls on the detector. The photocurrent is converted into a voltage by a resistance $r = 50 \, \Omega$ and amplified by a factor ξ producing a voltage

$$V_{\text{det}} = \gamma P \{1 + b \sin [\alpha (P - P_0)]\}, \quad (3.47)$$

where

$$\gamma = \frac{\rho \zeta_C \zeta_F \xi r}{2} \frac{1}{\sqrt{2}}. \quad (3.48)$$

The extra factor of $2^{-1/2}$ is included to account for losses in the directional coupler (labelled B in 3.3) and power splitter/combiner (labelled F in 3.3), respectively. This voltage delayed for a length of time τ_D before reaching the low-pass filter. In general, a single pole low-pass filter is described by the equation

$$\tau_L \dot{V} = -V + V_{in}(t), \quad (3.49)$$

where V_{in} is the input to the filter, $V(t)$ is the output, and τ_L is the response time. In this case, the input is $V_{\text{det}}(t - \tau_D)$ so the output of the low-pass filter is given by the equation

$$\tau_L \dot{V} = -V + \gamma P_{\tau_D} \{1 + b \sin[\alpha(P_{\tau_D} - P_0)]\}, \quad (3.50)$$

where $P_{\tau_D} \equiv P(t - \tau_D)$. The output of the low-pass filter is the input to the high-pass filter. A single pole high-pass filter is described by the equation

$$\dot{U} = -\frac{U}{\tau_H} + \dot{U}_{in}, \quad (3.51)$$

where U_{in} is the input to the filter, $U(t)$ is the output voltage, and τ_h is the response time. In this case, $U_{in} = V$ so

$$\dot{U} = -\frac{U}{\tau_H} + \dot{V}. \quad (3.52)$$

I assume this voltage is proportional to the current I_{AC} appearing in Eqs. 3.18 and 3.19 so that

$$P(t) = \sigma R U(t) + P_0, \quad (3.53)$$

where R is the constant of proportionality and has dimensions of impedance. Taking the derivative with respect to time of this equation and substituting Eq. 3.52 for \dot{U} I obtain

$$\dot{P} = -\frac{1}{\tau_H} (P - P_0) + \kappa \dot{V}, \quad (3.54)$$

where $\kappa \equiv \sigma R$. Equation 3.54 describes the evolution of the optical power output by the laser diode. The light from the laser travels through the interferometer and ultimately reaches the detector, thereby closing the feedback loop.

3.3 Experimental Determination of Model Parameters

Equations 3.50 and 3.54 together constitute the complete model of the active interferometer with time-delayed bandpass-filtered feedback. For reference, I restate them here

$$\begin{aligned} \dot{P} &= -\frac{1}{\tau_H} (P - P_0) + \kappa \dot{V}, \\ \tau_L \dot{V} &= -V + \gamma P_{\tau_D} \{1 + b \sin [\alpha (P_{\tau_D} - P_0)]\}. \end{aligned} \quad (3.55)$$

The model contains ten parameters. Table 3.1 lists their values as determined experimentally. In this section, I describe the measurements I perform to obtain these values.

The feedback loop gain γ depends on a number of parameters that are straight forward to measure. Specifically, according to Eq. 3.48,

$$\gamma = \frac{(50 \text{ ohms}) \rho \zeta_C \zeta_F \xi}{2\sqrt{2}}, \quad (3.56)$$

where ρ is the sensitivity of the photodiode, ζ_C is the fraction of the laser beam that falls on the small sensitive region of the photodiode, ζ_F is the fraction of light not

Parameter	Description	Value
τ_L	Low-pass filter time constant	0.66 ± 0.05 ns
τ_H	High-pass filter time constant	22 ± 0.5 ns
τ_D	Feedback delay time	19.1 ± 0.1 ns
κ	Voltage to power conversion at bias-T	$4.8 \pm 0.1 \times 10^{-3}$ mW/mV
α	Interferometer sensitivity	1.89 ± 0.05 mW $^{-1}$
P_0	Optical power operating point	26 ± 0.5 mW
b	Fringe visibility	0.8 ± 0.02
ρ	Photodiode sensitivity	0.44 ± 0.02 mA/mW
ζ_C	Fraction of total optical power detected	0.21 ± 0.02
ζ_F	Fraction of power transmitted by NDF	0.47 ± 0.02

Table 3.1: Physically relevant values of model parameters

absorbed by the neutral density filter, and ξ is the voltage gain of the amplifiers. The amplifier gain ξ is determined by input a known radio-frequency voltage and observing the output. The gain has some frequency dependence (less than 3 dB) within the bandwidth (0.01-1 GHz) so I use specifically the value at 52 MHz, the fundamental frequency of oscillation reported in the next section.

The photodiode sensitivity ρ , and losses due to beam clipping and the neutral density filter are determined by applying a known amount of light and observing the resulting photocurrent as follows. The light source for these measurements is the laser diode. The total power out with an injection current of 74 mA is determined to be $P_0 = 26$ mW using a large-area photoreceiver (New Focus 2031). I place the neutral density filter between the laser and the photoreceiver to find the fraction of power transmitted, ζ_F . I then replace the photoreceiver with the photodiode. I add a lens to the beam path to obtain a smaller beam width at the photodiode. The focusing ensures that all the optical power in the beam reaches the sensitive area of the photodiode. However, the photodiode is not positioned precisely at the focal point of the lens to prevent localized saturation of the detector. The current produced by the photodiode flows through a 50 Ω resistance and the resulting

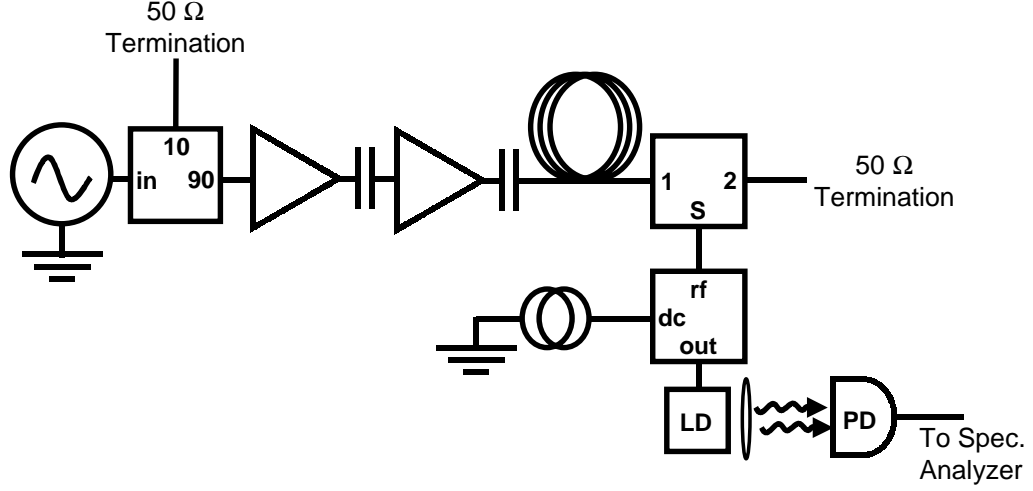


Figure 3.11: Setup for open loop measurements used to determine the transfer characteristics of the feedback loop.

voltage is recorded to determine ρ . Next, I place the laser at the input to the interferometer and the photodiode at the output. The photocurrent is measured one more time to determine ζ_C .

The parameters τ_L , τ_H , and κ determine the pass band of the electronic feedback loop. I obtain reasonable values for these parameters by measuring the open loop transfer characteristic of the feedback loop. The loop is broken by disconnecting the photodetector and repositioning it directly in front of the laser as shown in Fig. 3.11. A signal generator is connected in place of the photodetector so that a sinusoidal voltage of known amplitude and frequency is injected into the opened feedback loop and eventually to the laser. The output of the laser is measured immediately before the interferometer using the photodetector previously removed from the loop. This open loop configuration is described by a simple modification of Eq. 3.55. In this case, the input to the low-pass filter is a sinusoidal voltage of the form $V_{in} = V_0 e^{i\Omega t}$, where V_0 and Ω are the amplitude and frequency of the input

voltage, respectively. The voltage that modulates the laser is then given by

$$\tau_L \dot{V} = -V + \frac{1}{\sqrt{2}} \xi V_0 e^{i\Omega t}. \quad (3.57)$$

Assuming a sinusoidal response, the solution to this equation is

$$V(t) = \frac{\frac{1}{\sqrt{2}} \xi V_0}{1 + i\Omega \tau_L} e^{i\Omega t}. \quad (3.58)$$

Inserting this result into Eq. 3.55 and assuming the response of the optical power is of the form $P = P_{DC} + P_{AC} e^{i\Omega t}$, where P_{DC} is a constant offset and P_{AC} is a complex amplitude, I obtain

$$i\Omega P_{AC} e^{i\Omega t} = -\frac{1}{\tau_H} (P_{DC} + P_{AC} e^{i\Omega t} - P_0) + \kappa i\Omega \frac{\frac{1}{\sqrt{2}} \xi V_0}{1 + i\Omega \tau_L} e^{i\Omega t}. \quad (3.59)$$

Equating the constant terms I find

$$P_{DC} = P_0. \quad (3.60)$$

Equating the oscillating terms, cancelling common factors, and solving for P_{AC} gives

$$P_{AC} = \frac{\kappa \frac{1}{\sqrt{2}} \xi V_0}{\left(1 - \frac{i}{\Omega \tau_H}\right) (1 + i\Omega \tau_L)}. \quad (3.61)$$

Finally, solving for the magnitude of P_{AC} and rearranging I obtain

$$\frac{|P_{AC}|}{\frac{1}{\sqrt{2}} \xi V_0} = \frac{\kappa}{\sqrt{\left(1 + \frac{1}{\Omega^2 \tau_H^2}\right) (1 + \Omega^2 \tau_L^2)}}. \quad (3.62)$$

This equation can be compared with the experimentally determined open loop response in order to obtain physically relevant values of the parameters κ , τ_L , and τ_H . Figure 3.12 shows both the measured (circles) and theoretical (dotted line) response of the open loop system to sinusoidal driving at two different values of the amplifier gain ξ . The theoretical curve is produced using the values $\kappa = 4.8 \times 10^{-3}$ mW/mV, $\tau_L = 0.66$ ns, and $\tau_H = 22$ ns chosen by varying κ , τ_L , and τ_H in order to achieve

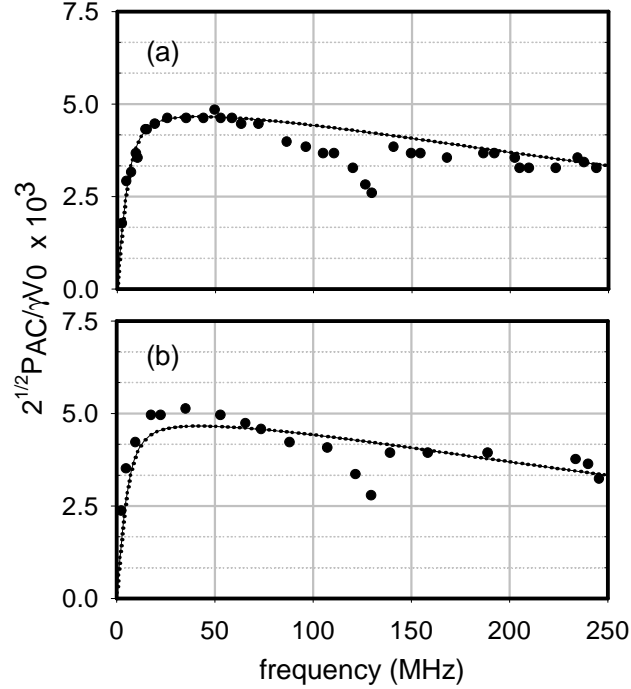


Figure 3.12: Frequency response of open loop system at two different gain values: (a) $\gamma = 14.6$, (b) $\gamma = 4.8$.

a good fit. With these values, the theoretical curve fits to within a few percent of the experimental data everywhere except in the region between 80 and 140 MHz. The dip in the response here is also apparent in the response of the laser to direct modulation through the bias-T. Therefore, it is apparently caused by either the bias-T or the electronics inside the laser mount. I choose to ignore this discrepancy because, as the next two sections show, the simple model successfully reproduces most features of the observed dynamics.

With the photodiode placed back at the output of the interferometer, the visibility b is determined by observing minima and maxima in the photodetector's output current as the DC injection current is varied. From these measurements,

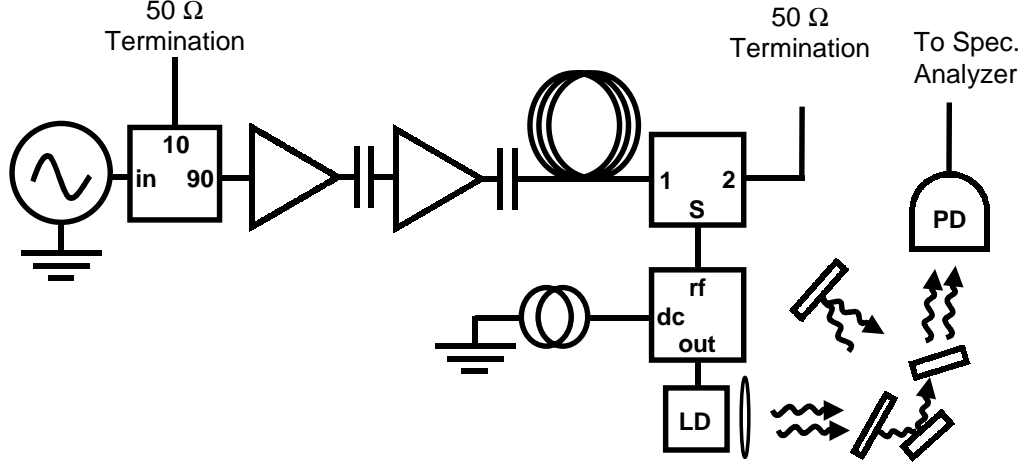


Figure 3.13: Setup for open loop measurements used to determine parameter α .

the minimum and maximum optical power is calculated for several fringes and Eq. 3.41 is evaluated to find b .

A second open loop measurement is made to determine the parameter α , in this case with the photodiode placed after the interferometer as shown in Fig. 3.13. I assume the optical power entering the interferometer is $P(t) = P_0 + P_{AC}e^{i\Omega t}$ where P_{AC} is given by Eq. 3.61. Inserting this into Eq. 3.42, I obtain the power output by the interferometer

$$P_1 = \frac{\zeta_F}{2} (P_0 + P_{AC}e^{i\Omega t}) \{1 + b \sin(\alpha P_{AC}e^{i\Omega t})\}. \quad (3.63)$$

Assuming $\alpha P_{AC} \ll 1$, which can be assured by keeping the drive voltage V_0 small, I approximate P_1 as

$$P_1 = \frac{\zeta_F}{2} (P_0 + P_{AC}e^{i\Omega t}) \{1 + b\alpha P_{AC}e^{i\Omega t}\}. \quad (3.64)$$

I collect terms according to oscillation frequency to get

$$P_1 = \frac{\zeta_F}{2} \{P_0 + (1 + P_0 b\alpha) P_{AC}e^{i\Omega t} + b\alpha P_{AC}^2 e^{i2\Omega t}\}. \quad (3.65)$$

The amplitude of the component at the drive frequency Ω is

$$\frac{\zeta_F}{2} (1 + P_0 b \alpha) P_{AC}. \quad (3.66)$$

The current from the photodiode is measured and analyzed using a spectrum analyzer. Equation 3.66 is then used to calculate α .

The remaining parameter is the time delay τ_D . Direct measurement of this parameter is not easy because it includes contributions from several electronic components, each of which introduces some phase lag in addition to simple propagation delay. Therefore, I resort to an indirect method that makes use of the model itself. I close the feedback loop and allow the system to oscillate periodically. The feedback gain γ is adjusted so that the system is just beyond the Hopf bifurcation. In the next section, I present a linear stability analysis of this bifurcation that relates the observed frequency to the time delay. I assume the correct value of τ_D is that which gives the same frequency of oscillation at the Hopf bifurcation as is observed in the experimental system.

3.4 Dynamics of Closed-Loop System without Modulation

To characterize the behavior of the active interferometer with time-delayed bandpass feedback, I examine the bifurcations that occur as I vary the loop gain γ from a low to a high value. In both the experiment and the model, I observe sequence of bifurcations beginning with a steady state and ending with broadband chaos. In this section, I first discuss the bifurcation from steady state to a periodic oscillation. I present a linear stability analysis to explain the fundamental frequency of oscillation. Then I discuss the later transition from periodic oscillation to broadband chaos.

To examine the bifurcations of a dynamical system without delay, it is often

useful to visualize trajectories in phase space. Much information can be gleaned from the geometry and topology of such a representation. However, the phase space of a delay system has an infinite number of dimensions and is difficult to visualize. Therefore, I simply examine time series and power spectra in order to explore the dynamics of my system. The two variables in the model, P and V , are not easily accessible. The power emitted by the laser P could be measured by putting a beam splitter between the laser and the interferometer. However, it is preferable to keep the free space propagation time as small as possible to minimize the response time of the active interferometer. The voltage V is only accessible by opening the laser mount itself. An experimentally convenient quantity is the output from the unused port of the interferometer. This quantity is compared with the output of the model using Eq. 3.43. All measurements described in the following subsections are from this second port using a detector identical with the one in the feedback loop. I record the voltage signal from this detector in the time domain using a high-speed digital oscilloscope, and in the frequency domain using a spectrum analyzer. Time series from the model are obtained by numerical integration using an Adam-Bashforth-Moulton predictor-corrector algorithm [101].

3.4.1 Hopf Bifurcation

With the gain below a critical value, both the experiment and model display a steady state. Figure 3.14 shows a time series of the optical power detected at the second output of the interferometer while the system is in the steady state. The fluctuations are attributed to noise in the loop, primarily phase noise in the diode laser. The existence of the steady state in the model is easily demonstrated by setting the derivatives in Eqs. 3.50 and 3.54 to zero and solving for P and V . The

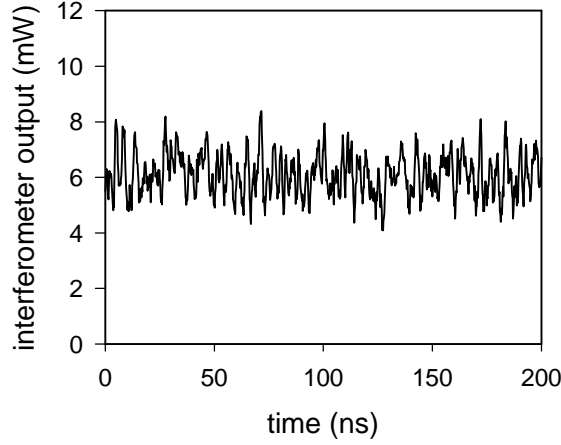


Figure 3.14: Time series of optical power detected at second port of interferometer with feedback gain $\gamma = 4.0$ mV/mW. The system is in a steady state with fluctuations due to phase noise.

result is

$$P_* = P_0, \quad (3.67)$$

$$V_* = \gamma P_0, \quad (3.68)$$

where P_* and V_* denote the steady state values of P and V . Assuming the value of P_0 as given in Table 3.1, the power out of the second port, given by Eq. 3.43, is 6.11 mW, in good agreement with the data in Fig. 3.14.

When the gain in the model is increased through the critical value $\gamma^* = 5.34$ mV/mW, the steady state is replaced by a periodic oscillation. As shown by the open circles in Figure 3.15(a), the amplitude of this oscillation grows smoothly from zero as the gain is increased. In the range just beyond the bifurcation point, the amplitude scales as $\sqrt{\gamma}$, as shown in Fig 3.15(b), suggesting a supercritical Hopf bifurcation [48]. A similar transition occurs in the experiment where the critical value of γ is 5.1 ± 0.5 mV/mW. The filled circles in Fig 3.15(a) show how the

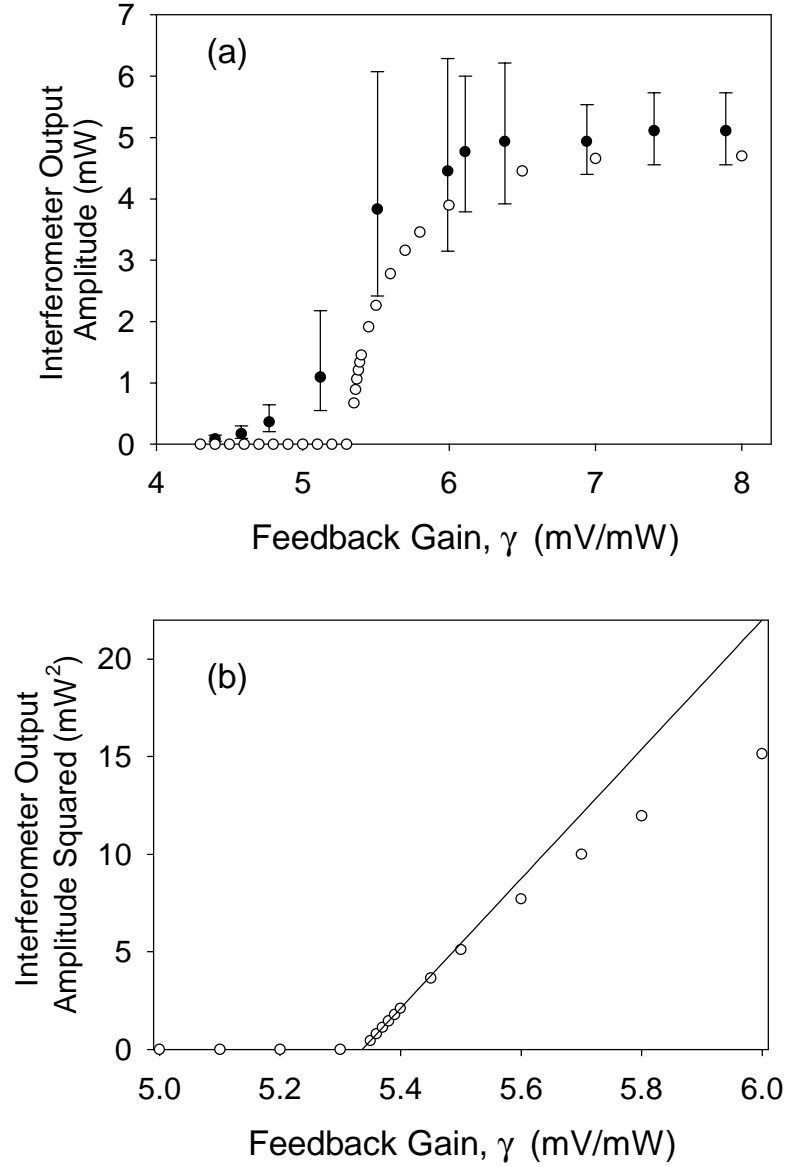


Figure 3.15: Experimental and simulated data showing how the amplitude of the periodic oscillation increases with the feedback gain γ . (a) The filled circles show the experimentally measured amplitude. The large error bars are due to the influence of phase noise near the transition. The open circles show data from the model. (b) A closer look at the model data near the bifurcation point. The line is a least squares fit to the points just beyond the bifurcation. The linear scaling of the square of the amplitude with the feedback gain indicates a supercritical Hopf bifurcation.

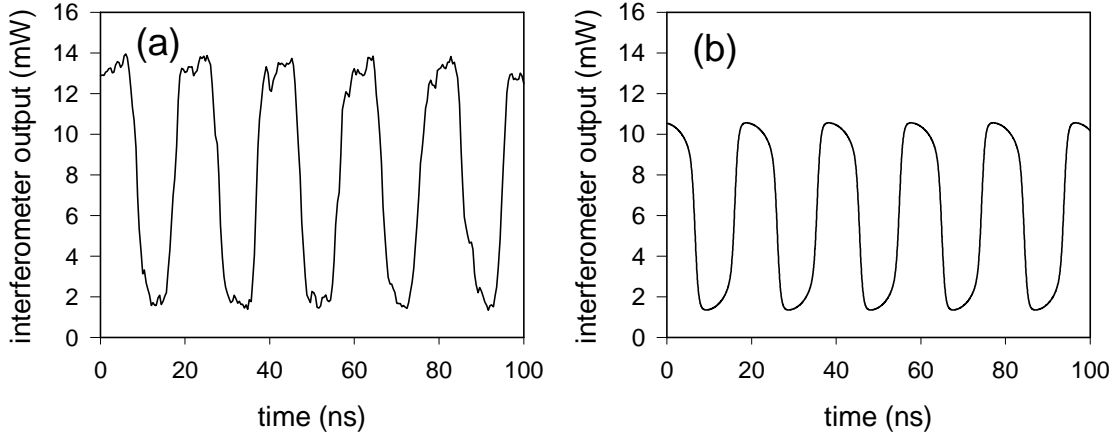


Figure 3.16: Time series from the (a) experiment and (b) model of the output at the second interferometer port in periodic regime. The feedback gain is $\gamma = 6.8$ mV/mW.

amplitude increases with the feedback gain. The rather large uncertainty is due to the fact that the phase noise obscures the transition by exciting the system to oscillate at the Hopf frequency even when it is slightly unstable. Figure 3.16 shows time series of the periodic oscillation from the experiment and model with $\gamma = 6.8$ mV/mW.

The dominant frequency of the oscillation is $51.5 \text{ MHz} \pm 1 \text{ MHz}$. This frequency is very nearly equal to $1/\tau_D$. By varying τ_D in both the model and experiment, I find that this relation holds over a wide, but limited range of τ_D . Experimentally, τ_D is varied by adding or subtracting fixed lengths of coaxial cable to the feedback loop. The first experimental value of $\tau_D = 19.1 \text{ ns}$ is determined according to the procedure described in the preceeding section. The other values are determined relative to this value by adding or subtracting propagation time appropriate to the change of cable length. Figure 3.17 shows the relation between the observed frequency and τ_D in model and experimental time series. In general, it appears the

frequency is approximately n/τ_D where n is an integer that increases with τ_D . The experimental data points coincide with the model data points except at $\tau_D = 65.9$ ns. Here the experimental system remains on the $n = 2$ branch while the model has switched to the $n = 3$ branch. This may indicate multistability above the bifurcation point. The set of Hopf frequencies observed represents a distinct difference between this dynamical system and those like the Ikeda and Mackey-Glass systems for which the fundamental frequency is always close to $1/(2\tau_D)$.

The fundamental frequency can be predicted from the model through linear stability analysis of the steady state. The analysis I now present was first performed by my collaborator, Dr. Lucas Illing. I consider a small perturbation about the steady state of the form

$$P(t) = P_* + \delta P e^{\lambda t}, \quad (3.69)$$

$$V(t) = V_* + \delta V e^{\lambda t}, \quad (3.70)$$

where δP and δV are small amplitudes and λ is the eigenvalue. Inserting these solutions into Eqs. 3.50 and 3.54, I obtain the characteristic equation

$$\lambda^2 + \left(\frac{1}{\tau_L} + \frac{1}{\tau_H} \right) \lambda + \frac{1}{\tau_L \tau_H} - \frac{\kappa \gamma}{\tau_L} (1 + b\alpha P_0) \lambda e^{-\lambda \tau_D} = 0, \quad (3.71)$$

where I have assumed $\alpha \delta P \ll 1$. The time delay produces an exponential term making the characteristic equation transcendental. Since I cannot solve this equation analytically, I determine the fundamental frequency at the bifurcation point only. Assuming $\lambda = is$ and separating the real and imaginary parts of Eq. 3.71, I obtain

$$-s^2 + \frac{1}{\tau_L \tau_H} - \frac{\kappa \gamma}{\tau_L} (1 + b\alpha P_0) s \sin(s\tau_D) = 0, \quad (3.72)$$

$$\left(\frac{1}{\tau_L} + \frac{1}{\tau_H} \right) s - \frac{\kappa \gamma}{\tau_L} (1 + b\alpha P_0) s \cos(s\tau_D) = 0. \quad (3.73)$$

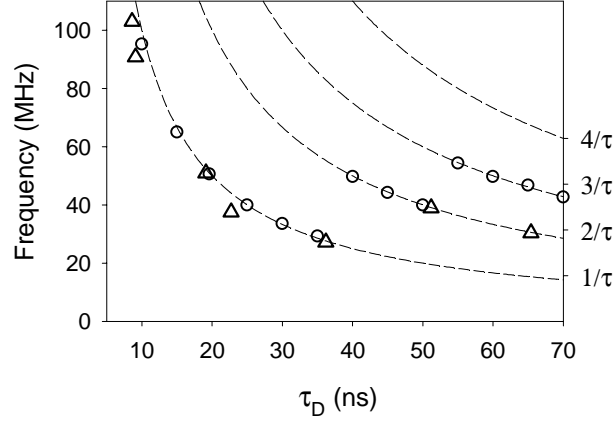


Figure 3.17: Hopf frequency as a function of delay time τ_D . Circles are data points from the numerical model. Triangles are experimental data points. The dotted lines show the function n/τ where $n = 1, 2, 3, \dots$

I set $x = s\tau_D$ and eliminate ε from these equations to obtain

$$x^2 - \frac{\tau_D^2}{\tau_L \tau_H} + \tau_D \left(\frac{1}{\tau_L} + \frac{1}{\tau_H} \right) x \tan(x) = 0. \quad (3.74)$$

This equation can be solved numerically to find all frequencies that go unstable as γ is increased. Due to the transcendental nature of the equation, there is an infinite number of such frequencies. The Hopf frequency is the one that goes unstable at the lowest value of γ . By eliminating τ_D from Eqs. 3.73 and 3.73 I obtain

$$\gamma_{th} = \frac{1 + \tau_L/\tau_H}{\kappa(1 + b\alpha P_0) \cos x}, \quad (3.75)$$

which is the threshold value of γ for a given value of x . Given a set of solutions to Eq. 3.74, I use this equation to find which frequency first goes unstable. The result is shown in by the solid line in Fig. 3.18. As observed in the experiment, the fundamental frequency is roughly n/τ_D with discrete jumps from one branch to another as τ_D increases. In the limit where $\tau_H \rightarrow 0$, the same stability analysis gives the fundamental frequency the system would display if the high-pass filter

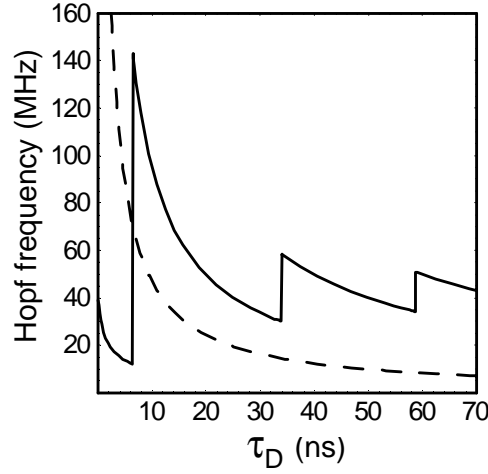


Figure 3.18: Hopf frequency predicted by linear stability analysis of steady state. The solid line corresponds to the active interferometer with bandpass feedback. The dotted line corresponds to the same system but with the high-pass filtering removed from the feedback loop. The discrete frequency jumps due to the high-pass filter are not displayed in well-known low-pass systems such as the Ikeda and Mackey-Glass.

were removed from the feedback loop. In that case Eq. 3.74 becomes

$$x + \frac{\tau_D}{\tau_L} \tan(x) = 0, \quad (3.76)$$

and Eq. 3.75 becomes

$$\gamma_{th} = \frac{1}{\kappa(1 + b_1 \alpha P_0) \cos x}. \quad (3.77)$$

The resulting frequency, roughly $1/(2\tau_D)$, is shown by the dashed line in Fig. 3.18. This case resembles the frequencies observed in the well-known Ikeda and Mackey-Glass systems that have only low-pass filtering in the feedback loop. The discrete jumps in the fundamental frequency can therefore be attributed to high-pass filtering in the feedback loop.

The origin of the fundamental frequency can be understood intuitively by considering whether a wave circulating in the feedback loop will reinforce itself. If the

feedback is positive, a wave will reinforce itself if an integer number of wavelengths equals the propagation length of the loop. If the feedback gain is negative, as in the Ikeda system, the propagation length must be a half integer number of wavelengths. Each of these infinite number of wavelengths represents a different mode of oscillation. When the gain in the loop is larger than the losses of a given mode, the wave will grow each time it travels around the loop. Assuming the gain bandwidth is not perfectly flat, one particular wavelength will reach this threshold first as the gain is increased from a low level. In a system with low-pass feedback, the gain is highest at low frequencies so the mode with the lowest frequency is the fundamental oscillation. If the feedback is also high-pass filtered, the gain may be peaked near a higher frequency mode so higher integer or half integer multiples of $1/\tau_D$ may become the fundamental oscillation. The Ikeda and Mackey-Glass systems both have negative, low-pass filtered feedback so the fundamental frequency is always near $1/(2\tau_D)$. The active interferometer has positive, band-pass filtered feedback so the fundamental frequency is roughly some integer multiple of $1/\tau_D$ where the integer is determined by the shape of the pass band. In the limit $\tau_H \rightarrow \infty$, the high-pass filter is removed but a sign change in the feedback is also removed producing negative, low-pass filtered feedback and consequently a fundamental frequency of $1/(2\tau_D)$.

3.4.2 Route to Chaos

Beyond the Hopf bifurcation, the system follows a sequence of bifurcations to chaos. The sequence does not appear to follow any of the standard routes such as period doubling or intermittency. Several non-standard routes to chaos have been observed in delay dynamical systems including an intermittency route with unusual laminar phase scaling [102] and a quasi-periodic route with two period doublings [103].

Figure 3.19 shows a series of power spectra from the experiment as γ is increased.

Experimentally Observed Behavior	Feedback Gain, γ (mV/mW)
steady state	$<5.1 \pm 0.5$
period-1	$5.1-11.0 \pm 1.0$
period-2 to chaos	$11-17 \pm 1$
very broadband chaos	$>17 \pm 1$

Table 3.2: Dynamic transitions in the opto-electronic device without modulation as the feedback gain is varied.

I measure the power spectral density when the gain is just below the Hopf bifurcation to obtain an estimate of the noise floor for these and all subsequent frequency domain measurements. The resulting noise floor is approximately 2×10^{-3} mW²/MHz². Spectral features weaker than this level are completely obscured in the experiment.

At feedback gains higher than the value at the Hopf bifurcation, the sinusoidal periodic oscillation begins to square off. Figure 3.19(a) shows a time series and power spectrum taken with $\gamma = 9.4$ mV/mW. The square shape of the waveform is most clearly indicated by the prominence of the odd harmonics in the spectrum. As the feedback gain is increased, a small, broad peak appears at half the fundamental frequency suggesting a period-doubling bifurcation as shown in Fig. 3.19(b) where $\gamma = 13.2$ mV/mW. The peak at half the fundamental frequency is three orders of magnitude below the fundamental, indicating that the period-doubled orbit only deviates slightly from the original orbit. The weakness and broadness of the peak at half the fundamental frequency coupled with the presence of phase noise may explain why the period doubling is not apparent in the time domain in Fig. 3.19(b). As the gain is further increased, the broad background rises and the tall peaks at the fundamental frequency and its harmonics weaken. Figure 3.19(c) shows a time series and power spectrum where $\gamma = 17.6$ mV/mW. The power spectrum is quite broad and the peaks have nearly dropped to the level of the background. Table 3.2 summarizes the route to chaos. Although the locations of bifurcations are difficult to determine precisely from the experimental system, the approximate range of each

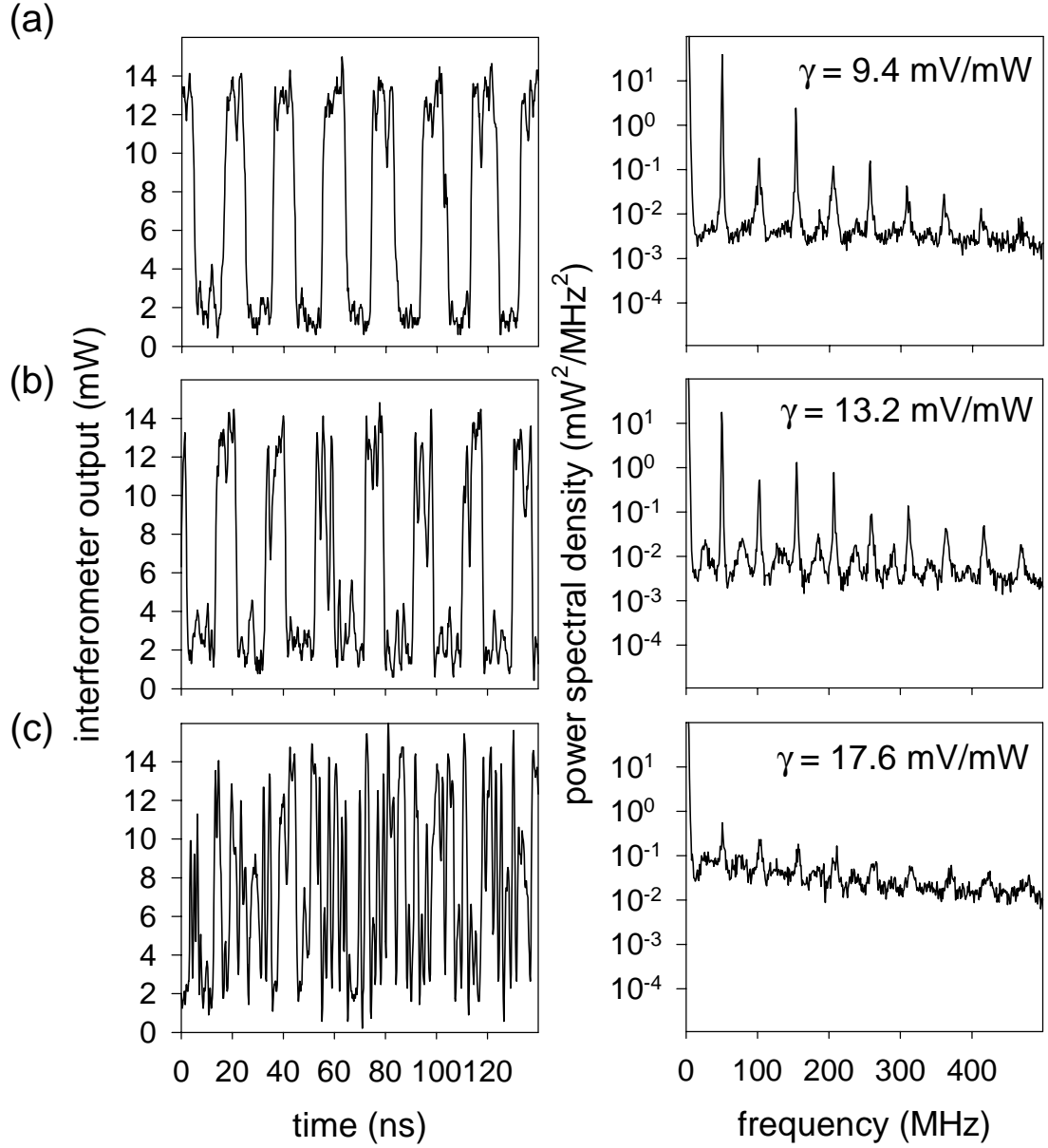


Figure 3.19: Experimentally measured time series and power spectra measured from the second output port of interferometer. Three steps on the route to chaos are shown.

type of observed behavior is given.

The degree of complexity of the chaotic oscillations is an important quantity for understanding both the dynamics of the system and its usefulness in applications. For example, the degree of security in chaos-based communications schemes is believed to be related to the complexity of the dynamics [88]-[90]. Although techniques exist for extracting various measures of complexity (dimension, entropy, Lyapunov exponents) from experimental time series, they require long ($>10^6$ points), high resolution (12 bit or better) data sets with very little noise [104, 105]. Such data is not attainable from this system due to its high speed and the strong influence of phase noise. I have attempted to apply the false nearest neighbors [105] method for estimating dimension to experimental data collected with a high-speed digital oscilloscope. With data sets of 15,000 points with 8 bit resolution, the method failed to converge. Furthermore, even with a mathematical model, accurate determination of important dynamical quantities is difficult for any time-delay system exhibiting high dimensional chaos. Studies of time delay systems with low-pass filtered feedback suggest that the dimension of the chaotic attractor is given roughly by the number harmonics of the fundamental frequency that fit within the low-pass filter bandwidth in the long-delay limit [108]. Loosely speaking, increasing the time delay puts more modes within the bandwidth of the system increasing the complexity of the dynamics. Applying this relation to my system gives an estimated maximum dimension of ~ 4.5 . However, it is not clear that this rule applies to this system. Some attempts have been made to estimate the Lyapunov dimension of a delay system with band-pass filtered feedback [44]. Interestingly, the dimension was found to be nearly three times the dimension of a low-pass filtered system with the same bandwidth. However, the value obtained (3,700) is extremely high and the method used to estimate it is generally believed to be unreliable for dimensions above 10 or

so.

A similar route to chaos is displayed by the model as seen in Fig. 3.20 where time series and power spectra are shown for the values of γ used the experiment. The power spectra are obtained by performing a Fast Fourier Transform on the model timeseries with a 610 kHz frequency resolution and 20 GHz Nyquist critical frequency [101]. At $\gamma = 9.4$ mV/mW, the oscillation, shown in Fig. 3.20(a) is nearly a square wave. Odd harmonics dominate the power spectrum. At $\gamma = 13.2$ mV/mW, the square wave has undergone at least one period doubling; however, the fundamental frequency is still several orders of magnitude larger than any harmonic or subharmonic, as shown in Fig. 3.20(b). Also, a low frequency component appears in the time domain as small differences in the waveform from one period to the next. Figure 3.21 shows the same power spectrum with a finer frequency resolution (152.5 kHz). A relatively large peak appears at 1.8 MHz. This low frequency oscillation does not appear to be a transient or the product of a particular integration algorithm. Since 1.8 MHz falls below the high-pass filter cutoff frequency (3 dB point), the origin of this oscillation remains unclear. The presence of this low frequency and its harmonics may contribute to the broadness of the peaks observed in the lower resolution experimental power spectra at half the fundamental frequency as for example in Fig. 3.19(b).

Finally, at $\gamma = 17.6$ mV/mW, the waveform no longer resembles a square wave. The power spectrum, shown in Fig. 3.20(c), is very broad with only a few peaks rising more than an order of magnitude above the background. The dynamics of the model appear to resemble qualitatively the experiment experimentally observed behavior quite well.

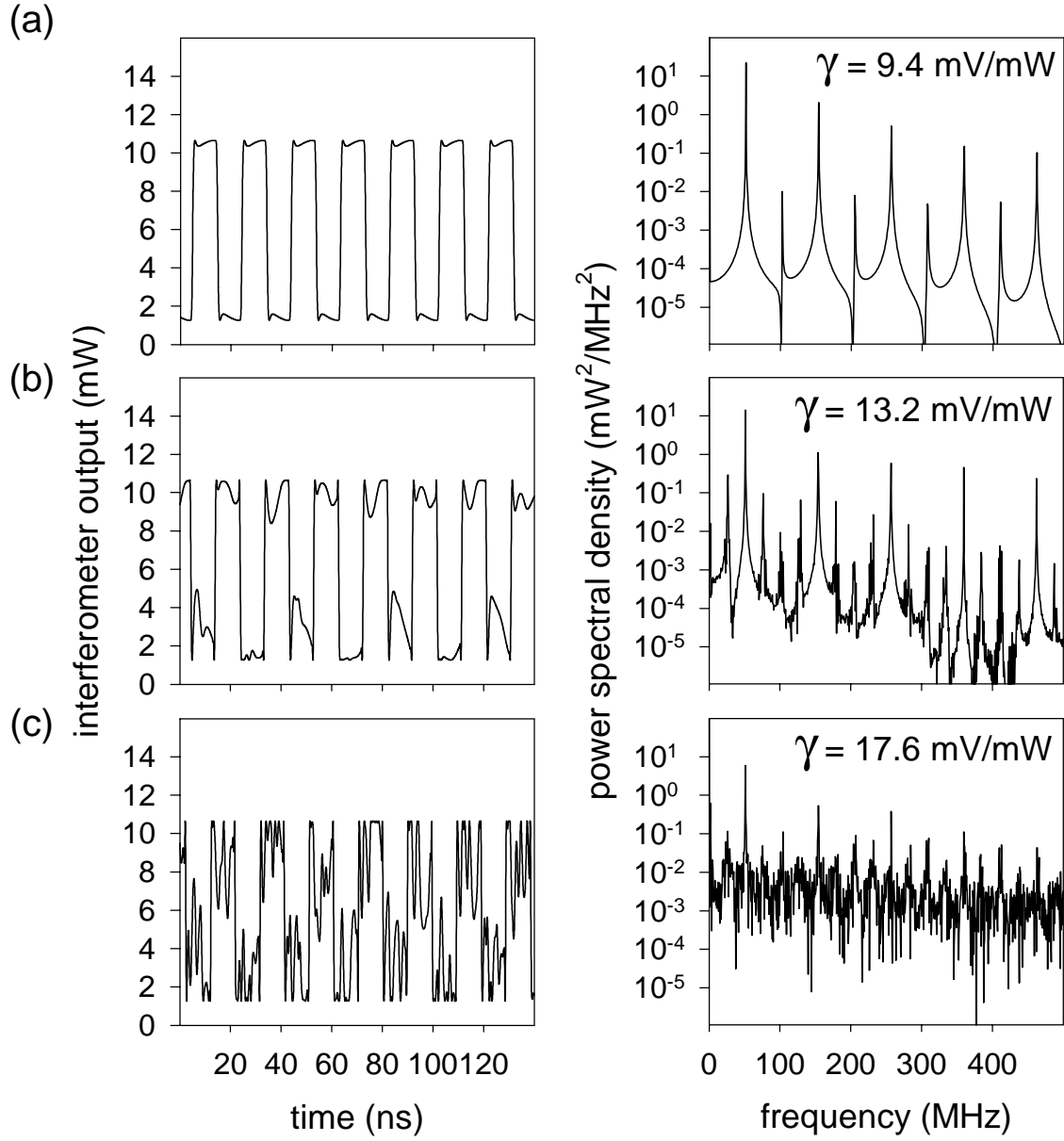


Figure 3.20: Time series and power spectral densities from model at the same gains as experimental data shown in Fig. 3.19.

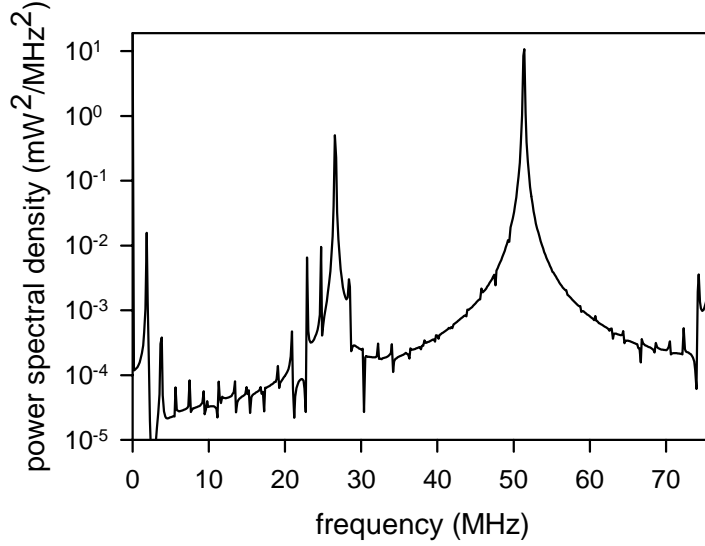


Figure 3.21: A closer look at the low-frequency part of the power spectral density of the interferometer output from the model with $\gamma = 13.2$ mV/mW. The frequency resolution is four times higher than in Fig. 3.20(b).

3.5 Dynamics with External Modulation

In this section, I investigate the effects of external modulation on the active interferometer with delayed bandpass feedback. First, I examine frequency locking due to weak modulation near the fundamental frequency. Frequency locking has been reported in delay systems with only low-pass filtered feedback [106, 107] but has not previously been investigated in systems with bandpass feedback. Frequency locking plays an important role in applications such as dynamical memory where the time-delay system is locked to an external reference clock [34]. Next, I study the route to chaos under stronger external modulation. As shown in the previous section, the period doubling bifurcation displayed by the active laser interferometer without modulation is rather subtle. The frequency component at half the fundamental frequency is three orders of magnitude smaller than the component at the fundamental

frequency. In this section, I show that the addition of an external modulation near the fundamental frequency significantly enhances the frequency component corresponding to the period doubled solutions. This effect is of practical importance to the control experiments reported in the next chapter. In control experiments generally, the domain of control is determined by varying the controller parameters and observing an error signal that measures the distance from the desired orbit. A large jump in the error signal is interpreted as the edge of the domain. However, this approach becomes problematic when applied to the active interferometer without modulation because the uncontrolled state differs only slightly from the controlled state so no sudden jump is observable. Since in the modulated system the orbits are more distinct, the error signal is much easier to interpret and is therefore a better testbed for evaluating the effectiveness of a controller.

The modulation is added by injecting a sinusoidal voltage into the feedback loop just before the bias-T through an RF power combiner as shown in Fig. 3.3. The effect of this injected voltage is described by adding a time dependent term to Eq. 3.53 to get

$$P(t) = \sigma R [U(t) + V_m \sin(\Omega_m t)] + P_0, \quad (3.78)$$

where V_m and $\Omega_m/2\pi$ are the modulation amplitude and frequency. Taking the derivative with respect to time and substituting Eq. 3.52, the full model becomes

$$\tau_L \dot{V} = -V + \gamma P_{\tau_D} \{1 + b_1 \sin[\alpha(P_{\tau_D} - P_0)]\}, \quad (3.79)$$

$$\dot{P} = -\frac{1}{\tau_H} (P - P_0) + \kappa \left[\dot{V} + \Omega_m V_m \cos(\Omega_m t) \right]. \quad (3.80)$$

When the modulation frequency is close to the fundamental frequency, frequency locking occurs pulling the natural oscillation frequency towards the modulation frequency. Figure 3.22 shows the strongest peak in the power spectrum as a function

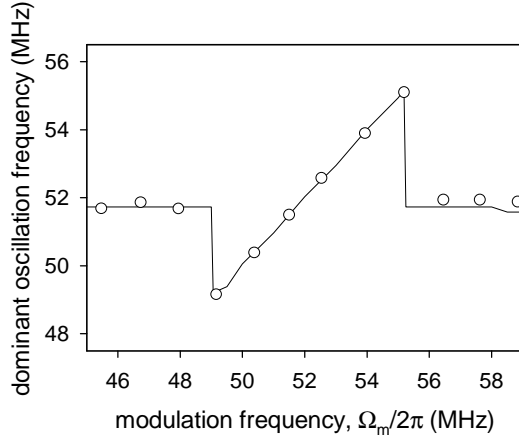


Figure 3.22: Frequency locking due to weak external modulation at a frequency near the fundamental oscillation frequency. The circles show experimental data. The solid line shows results from the mathematical model. The feedback gain is $\gamma = 6.3$ mV/mW.

of the modulation frequency from both the experiment (circles) and the numerically integrated model (solid line). With the loop gain $\gamma = 6.3$ mV/mW and the modulation amplitude $V_m = 34$ mV, a locking region of about 6 MHz is apparent. The strong agreement between the model and the experiment confirms that Eq. 3.80 correctly describes the effect of external modulation.

Under stronger modulation, the system follows a route to chaos much like that described in the previous section where a fundamental frequency period doubles and then broadens into chaos as γ is increased. Figure 3.23 shows several experimental time series and power spectra of the optical power at the second interferometer port with $V_m = 225$ mV and $\Omega_m/2\pi = 51.7$ MHz. With the feedback gain below $\gamma = 6.7 \pm 0.4$ mV/mW, the system displays a periodic oscillation at the external modulation frequency (to within the 300 kHz resolution bandwidth of the spectrum analyzer) as shown in Fig. 3.23(a). When the feedback gain is increased beyond $\gamma = 6.7 \pm 0.4$ mV/mW a period doubling occurs producing a large frequency component at half

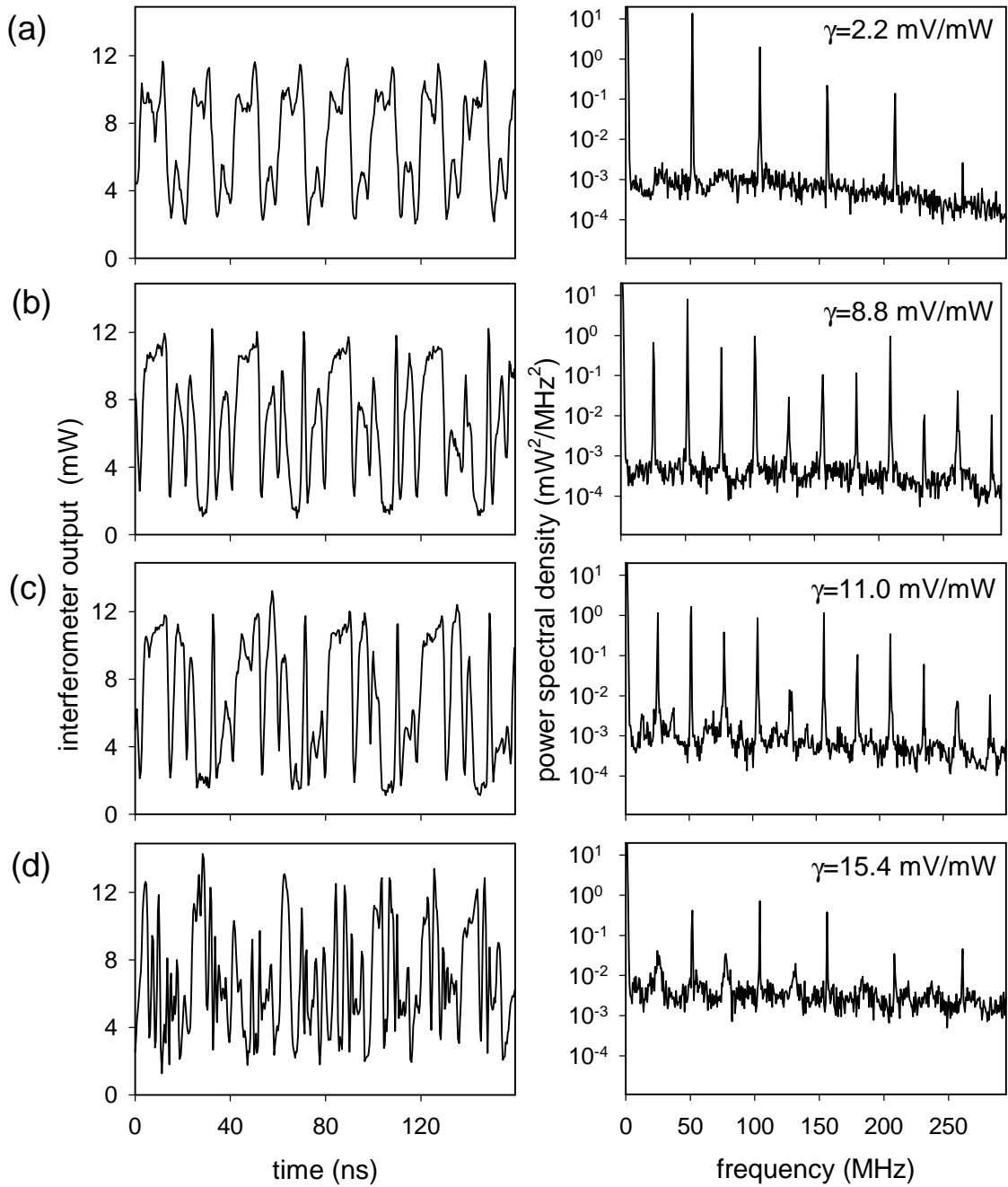


Figure 3.23: Experimentally measured time series and power spectra of the output power at the second port of the active interferometer with external modulation showing route to chaos as γ is increased. The loop gain γ is (a) 2.2 mV/mW, (b) 8.8 mV/mW, (c) 11.0 mV/mW, and (d) 15.4 mV/mW. The period-doubled orbit in (b) has a much stronger component at half the fundamental frequency (~ 26 MHz) than in the undriven system (see Fig. 3.19(b)).

Experimentally Observed Behavior	Feedback Gain, γ (mV/mW)
period-1	$<6.7 \pm 0.4$
period-2	$6.7-10.0 \pm 0.5$
period-4 dominated chaos	$10.0-15.0 \pm 0.5$
very broadband chaos	$>15 \pm 0.5$

Table 3.3: Experimentally observed dynamic transitions in the modulated system as the feedback gain is varied.

the modulation frequency. Figure 3.23(b) shows the period doubled oscillation and the large frequency component at $\Omega_m/4\pi$ when $\gamma = 8.8$ mV/mW. The height of the frequency component corresponding to the doubled period is within an order of magnitude of the peak at the fundamental frequency. This contrasts strongly with the period doubled solution in the undriven system where the period doubled frequency was three orders of magnitude smaller than the fundamental (see Fig. 3.19(b)). As the gain is increased beyond $\gamma = 10.0 \pm 0.5$ mV/mW, the frequency content around one fourth of the fundamental begins to peak as seen in Fig. 3.23(d) where $\gamma = 11.0$ mV/mW. This may indicate another period doubling transition. Finally, beyond $\gamma = 15.0 \pm 0.5$ mV/mW, the background in the power spectrum rises and the peaks fall, resulting in a broad, flattened spectrum where the time series is extremely irregular. The entire route to chaos is summarized in Table 3.3. Using the same gain values as in the experiment, very similar time series and power spectra are produced by the model, as shown in Fig. 3.24. With $\gamma = 2.2$ mV/mW, as shown in Fig. 3.24(a), the model displays a period one orbit. Around $\gamma = 6.7$ mV/mW, a period doubling occurs. As in the preceeding section, the period-doubled orbit is subject to low-frequency modulation as shown in Fig. 3.24(b). As the feedback is further increased, the background in the power spectrum broadens and a peak appears at one fourth the fundamental frequency, as shown in Fig 3.24(c). As in the experiment, the peak at one fourth the fundamental oscillation is small and broad. This may indicate that the system is already chaotic but that the period

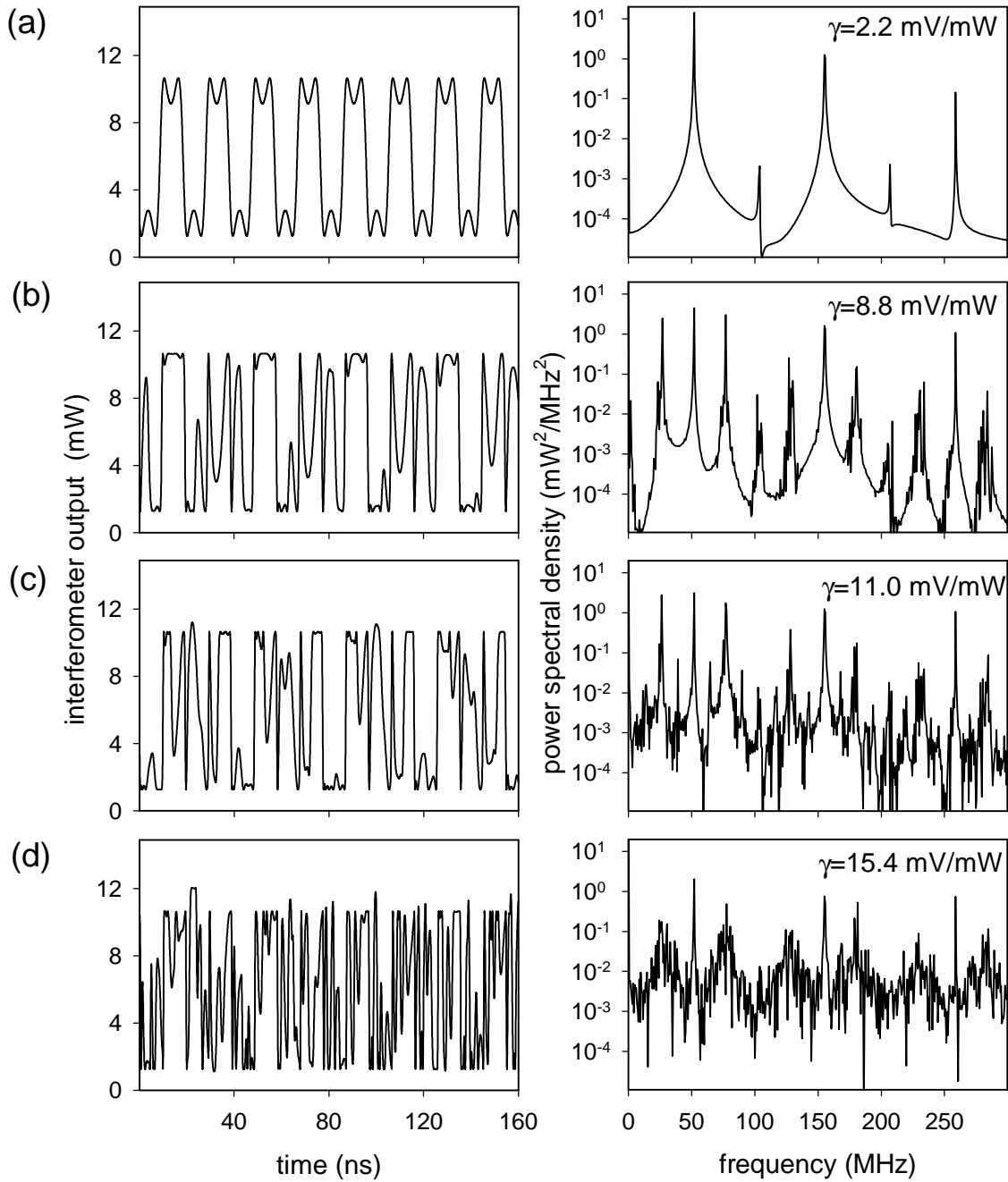


Figure 3.24: Time series and power spectra from the numerically integrated model of the modulated system showing the route to chaos. As in the experiment, the frequency content of the period doubled orbit has a much stronger component at half the fundamental frequency than the similar orbit in the unmodulated case (see Fig. 3.20(b)). The gain γ is (a) 2.2 mV/mW, (b) 8.8 mV/mW, (c) 11.0 mV/mW, and (d) 15.4 mV/mW.

four orbit is only weakly unstable. In Fig. 3.24(d), where $\gamma = 2.2$ mV/mW, the power spectrum is considerably flattened and the system is clearly chaotic.

3.6 Discussion

In this chapter I have presented a new fast chaotic time-delayed optical system. As shown in later chapters, the system is suitable for fundamental studies of controlling fast dynamics. It also has many features that make it well suited for applications such as chaos-based communications.

The system is flexible in the sense that key characteristics are easily manipulated. The source of nonlinearity in the system is the Mach-Zehnder interferometer. The shape of the nonlinearity is easily modified by adjusting the mirrors that make up the interferometer. In applications such as synchronization-based communications, where a slave oscillator must be closely matched to a master, this accessibility is a significant advantage over chaotic optical systems that are strongly affected by fixed or non-adjustable nonlinearities, such as the material properties of a semiconductor laser or erbium-doped fiber laser.

The timescale of the chaotic oscillations is also easily modified. The data and analysis in Sec. 3.4.1 show that the fundamental frequency of oscillation can be tuned by adjusting the feedback delay time. The total bandwidth of the chaotic fluctuations is limited by the passband of the feedback loop. For the purposes of this study, I choose to use components that produce a relatively slow fundamental frequency of 51 MHz and a pass band of 7-250 MHz so that the system does not oscillate too rapidly for a fast data acquisition device (a 1 GHz bandwidth digitizing oscilloscope) to obtain accurate time series. As shown in Fig. 3.17, by simply reducing the feedback delay to 8.6 ns, I obtain a fundamental oscillation frequency of 103 MHz, much faster than many chaotic opto-electronic systems that have been

reported in the literature [42, 43, 45]. However, the system could easily be implemented with faster electronic components and a shorter feedback delay to obtain the much higher speeds necessary in a real communication system. The timescale of chaotic oscillations in other sources of fast optical chaos, such as the semiconductor laser with optical feedback or erbium-doped fiber laser, is determined by the internal dynamics of a laser and, therefore, is not tuneable.

The model presented here may no longer apply if the oscillation speed approaches the relaxation oscillation frequency. To retain the model, the injection current could be set far above threshold to achieve the highest possible relaxation oscillation frequency. A value on the order of 20 GHz is obtainable with some diode lasers so the model may be scaleable to oscillations at a few gigahertz [96].

Chapter 4

Modified TDAS Control for Time-Delay Systems

In the last chapter, I introduced a new fast chaotic time-delay system. Fast time-delay optical and electro-optical chaotic systems are likely to be key elements in chaos-based applications such as communications, dynamic memory, and computation. However, successful application of such devices requires a fundamental understanding of techniques for manipulating the chaotic dynamics such as control and synchronization. Several researchers have demonstrated techniques for synchronizing fast chaotic optical systems [28, 31, 58, 109, 110]. Relatively little success has been demonstrated with respect to the related problem of control.

Much effort has focused on controlling semiconductor lasers with optical feedback, but with limited success [38, 54, 111, 112]. The primary source of difficulty in controlling such systems is the high speed of fluctuations. Rapid oscillations present two challenges. First, high speed sampling technology is necessary to obtain accurate time series. At present, the fastest digital sampling oscilloscopes can record data at rates of a few billion samples per second. However, some chaotic optical systems are known to display oscillations on a time scale three orders of magnitude shorter. Second, as discussed in Ch. 2, chaos control schemes fail when the control loop latency is comparable to the expansion rate in phase space. Although latency as short as 4.4 nanoseconds has been demonstrated, this is still clearly too long for many systems of interest [63].

Time delay auto-synchronization has proven to be an effective control technique for chaotic systems displaying oscillations at megahertz frequencies. In this scheme,

the control signal is determined by comparing the state of the system at the present time with the state of the system at a time in the past. The state of the system is represented by either one of the variables of the system or a linear combination of multiple variables. The time delay τ_P is chosen to be the period τ_P of the unstable periodic orbit to be stabilized. Nonetheless, it can fail if control loop latency is larger than 10-20% of the period of the orbit. Extended time delay auto-synchronization has been shown to be more robust to latency by retaining information from an infinite number of past states in order to determine the control signal. However, implementing ETDAS can be very challenging.

In this chapter, I introduce a modified approach to TDAS control applicable to time delay systems that allows for latency equal to the time delay. This technique should be applicable to many of the electro-optic time delay systems currently being studied and may also be useful for other systems described by delay differential equations. I apply the modified TDAS control approach to the active laser interferometer with bandpass feedback described in the previous chapter. In Sec. 4.1, I describe this new control approach. In Sec. 4.2, I present an experimental demonstration of the modified TDAS approach by applying it to the active interferometer with bandpass feedback and external modulation. The success of control is quantified by measuring the domain of control. In Sec. 4.3, I develop a mathematical model of the interferometer with control. The model shows behavior in qualitative agreement with the experiment.

4.1 Modified TDAS Control

Several optical time-delay systems have been designed expressly to produce sub-nanosecond chaotic fluctuations [27, 44, 57]. Such fast fluctuations would be difficult to control using techniques that cannot compensate for a significant amount of

control loop latency. In this section, I introduce a modified form of the TDAS control method for fast chaotic time-delay systems that permits an amount of latency equal to the feedback delay time of the system.

To illustrate this control approach, I will apply it the model equation introduced by Ikeda

$$\dot{x}(t) = -x(t) + \gamma f[x(t - \tau_D)], \quad (4.1)$$

where γ is the strength of the nonlinearity and τ_D is the delay time. The function $f(x)$ is assumed to have at least one maximum. This equation was originally derived as a model of a ring cavity containing a nonlinear dielectric medium in which case $f[x] = \pi \sin(x)$ [76]. Recently, numerous electro-optic devices have been devised that are described by this type of equation with various nonlinear functions [43], [110]-[35]. The Mackey-Glass Equation, a common model for studying time delay systems, is also of this form with $f[x] = x(1 + x^{10})^{-1}$ [41].

In all these cases, Eq. 4.1 may be viewed as describing a low pass filter with unit response time and input $u(t) = \gamma f[x(t - \tau_D)]$ as shown schematically in Fig. 4.1. The input term $u(t)$ retains a “memory” of the system state a time τ_D in the past. This memory is reflected in the autocorrelation function of $f[x(t)]$ defined as

$$c_{auto}(\tau_D) = \frac{\int_{-\infty}^{\infty} f[x(t)]f[x(t - \tau_D)]dt}{\int_{-\infty}^{\infty} f[x(t)]^2 dt}, \quad (4.2)$$

which gives the correlation between a time series of $f[x(t)]$ and the same time series with a delay τ_D [104]. For example, Fig. 4.2 shows the autocorrelation function of the input term of Eq. 4.1 where $f[x] = \pi \sin(x)$ with $\gamma = 2.1$ and $\tau_D = 20$. With these parameter values, the dimension of the system has been estimated to be approximately 42 [40]. Nonetheless, a series of peaks in the autocorrelation function appear at frequencies near $n\tau_D$ where $n = 1, 2, 3, \dots$. This suggests that

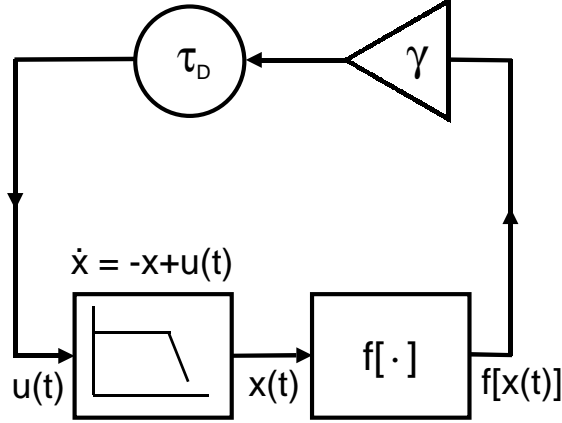


Figure 4.1: Block diagram showing the general form of the class of time-delay systems to which the modified TDAS method may be applied. The basic elements are a low pass filter, a nonlinear element ($f[x]$), and a delayed feedback loop. Well known models such as the Ikeda and Mackey-Glass equations are of this form.

the $f[x(t - \tau_D)]$ may contain sufficient information to predict $f[x(t)]$ and perturb the system accordingly in order to effect control.

Based on this observation, I propose to control time delay systems by modifying the TDAS approach in two ways. First, the control loop latency is intentionally set to τ_D . Second, the feedback control signal is the difference between the values of the nonlinear function $f[x]$ at times separated by the desired orbits period rather than the difference in the values of x itself. Applying this control method to Eq. 4.1 gives

$$\dot{x}(t) = -x(t) + \gamma f[x(t - \tau_D)] + \gamma_c \{f[x(t - \tau_D)] - f[x(t - \tau_D - \tau_P)]\}, \quad (4.3)$$

where γ_c is the control gain and τ_P is the period of the desired orbit. Figure 4.3 shows a block diagram of the system plus controller.

The original TDAS scheme assumes nearly instantaneous feedback from the

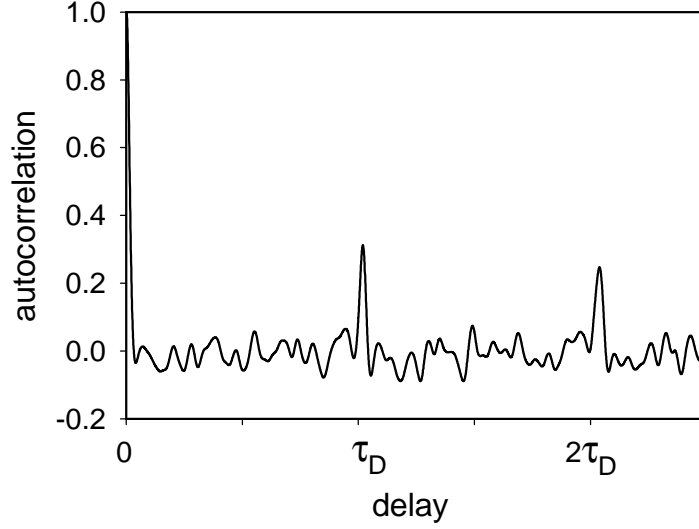


Figure 4.2: Autocorrelation function of the nonlinear term of the Ikeda model of a passive nonlinear resonator in the regime of high dimensional chaos. The peak at τ_D suggests that a delayed version of the nonlinear term may contain sufficient information about the current state of the system to successfully control it.

controller, whereas it has been shown that latency on the order of 20% of the period of the orbit is usually enough to foil TDAS control [49, 50]. The fundamental oscillation displayed by this class of systems typically has a period of τ_D or $2\tau_D$ so a TDAS controller is likely to fail if subject to a latency of τ_D . The modified TDAS scheme allows a period of time τ_D in order to compute and apply the appropriate control signal and therefore may allow control of faster systems.

To test the proposed control scheme experimentally, I apply it to the time delay system described in the previous chapter, the active interferometer with bandpass feedback and external modulation. The control signal is generated using the second output of the interferometer. A photodetector at the second port of the interferometer converts the emitted power into a voltage. The voltage signal is split. One half is delayed by a time τ_P and then subtracted from the other. The resulting signal

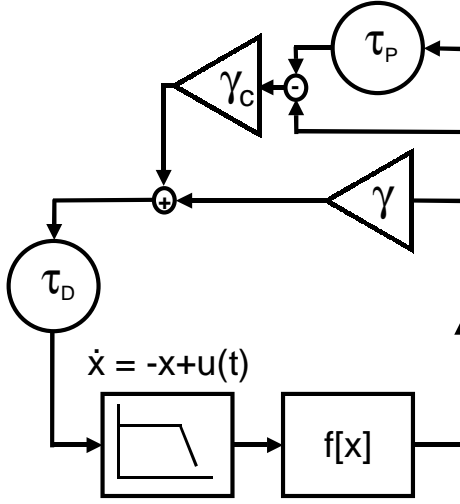


Figure 4.3: Block diagram showing the modified TDAS control scheme. The feedback control signal is the difference between the values of the nonlinear function $f[x]$ at times separated by the period of the desired orbit. The control loop latency is set equal to τ_D

is amplified and combined with the feedback loop of the interferometer before the bias-T. Figure 4.4 shows a schematic diagram of the entire system including the controller.

4.2 Experimental Demonstration of Modified TDAS Control

In this section, I describe the experimental demonstration of the modified TDAS control scheme. The experimental system is the active interferometer with delayed bandpass feedback and external modulation. I describe how I implemented the controller using radio-frequency electronic components. I present methods for properly setting the necessary time delays. The effectiveness of the controller is quantified by estimating the domain of control of a periodic orbit with a frequency close to that of the fundamental oscillation frequency.

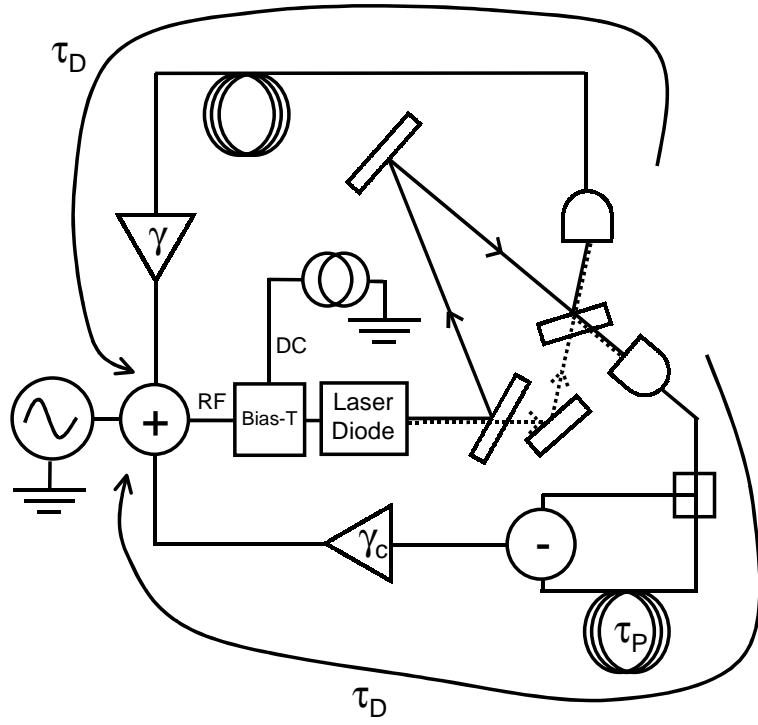


Figure 4.4: Schematic diagram of active interferometer and controller. A photodetector at the second port of the interferometer converts the emitted power into a voltage. The voltage signal is split. One half is delayed by a time τ_P and then subtracted from the other. The resulting signal is amplified and combined with the feedback loop of the interferometer before the bias-T. The propagation time through the controller is set equal to the feedback delay time, τ_D .

4.2.1 Modified TDAS Controller Implementation

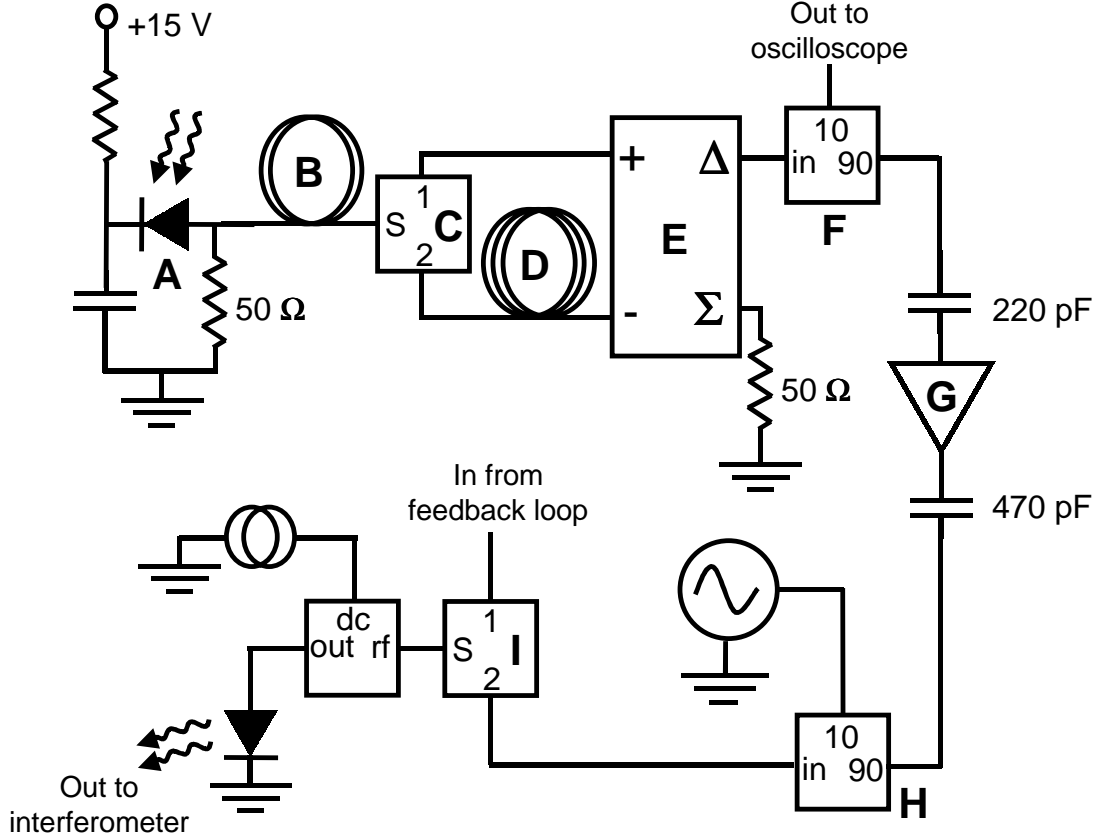


Figure 4.5: Schematic diagram of the modified TDAS controller. The components labelled A-I are as follows: A - Hamamatsu silicon photodiode S4751; B - Coaxial cable RG 58/U and variable delay; C - MiniCircuits power splitter/combiner ZFSC-2-1W-75; D - Coaxial cable RG 58/U and variable delay; E - M/ACOM 180 hybrid junction H-9; F - MiniCircuits directional coupler ZFDC-20-4; G - MiniCircuits amplifier ZFL-1000GH; H - MiniCircuits directional coupler ZFDC-10-1; I - MiniCircuits power splitter/combiner ZFSC-2-1W-75.

To implement the modified TDAS scheme, I use RF electronic components similar to those used in the feedback loop of the active interferometer itself. Figure 4.5 shows the experimental implementation of the modified TDAS controller in detail.

The intensity at the output of the second port of the interferometer falls on a Si

photodiode (A in Fig. 4.5). Only 23% of the power is detected because the beam width is larger than the active region of the detector for reasons discussed in Sec. 3.1. The photodiode produces a current proportional to the incident power that is converted to a voltage through a $50\ \Omega$ resistance.

This voltage signal propagates through a length of coaxial cable to an RF power splitter (C in Fig. 4.5, 5-600 MHz bandwidth). The length of the cable is chosen so that the total propagation time through the entire control loop is τ_D . (The procedure for accurately determining the proper length is described below.) The voltage at each of the two outputs of the power splitter is $1/\sqrt{2}$ times the input voltage. The voltage signal from port 1 of the power splitter travels directly to the 180° hybrid junction (M/ACOM H-9, 2-2000 MHz bandwidth, labelled E in 4.5). The voltage signal from port 2 of the splitter travels down a length of coaxial cable before reaching the hybrid junction. The length of the cable (D in Fig. 4.5) is chosen so that the voltage signal from port 2 is delayed by a period of time equal to τ_P relative to the voltage signal from port 1.

The two voltage signals from the splitter are recombined by the 180° hybrid junction which performs the subtraction operation. This passive device has two input ports, labelled $+$ and $-$ in Fig. 4.5, and two output ports labelled Δ and Σ . When RF voltages V_+ and V_- are applied to the $+$ and $-$ ports respectively, the voltages at the Δ and Σ ports are

$$\Delta = \frac{1}{\sqrt{2}}(V_+ - V_-), \quad (4.4)$$

$$\Sigma = \frac{1}{\sqrt{2}}(V_+ + V_-). \quad (4.5)$$

The output of port 1 of the power splitter enters the $+$ port. The signal from port 2 of the power splitter enters the $-$ port of the hybrid after propagating through

the cable. The Σ port of the hybrid is terminated through $50\ \Omega$ and the power dissipated here is not used. The Δ port supplies the signal that travels through the remainder of the control loop.

A small fraction (1%) of the power output from the Δ port of the hybrid is sampled by a directional coupler (MiniCircuits ZFDC-20-4, 1-1000 MHz bandwidth), amplified by a low noise amplifier (MiniCircuits ZFL1000LN, 0.1-1000 MHz bandwidth), and recorded by a high-speed digital oscilloscope (Tektronix TDS680B, 1 GHz bandwidth). This signal provides a measure of the error between the state of the system and the desired state.

The remainder of the signal power from the hybrid continues in the control loop passing through a 220 pF capacitor, a variable gain amplifier (MiniCircuits ZFL-1000GH, 10-1000 MHz bandwidth), and a 470 pF capacitor. The capacitors are chosen to match those in the interferometer feedback loop (see Fig. 3.3) so that the controlled signal undergoes the same band pass filtering as the feedback signal. The resulting control signal is combined with the external modulation signal through a directional coupler (MiniCircuits ZFDC-10-1, 1-500 MHz bandwidth). The control signal is directed into what is normally the “output” port while the modulation signal enters through the coupling port. The combined signal exits through the nominal “input” port. This configuration is chosen in order to isolate the components that measure the error signal from the modulation source. Finally, the combined modulation and control signal reaches a power combiner that sums it with the interferometer’s feedback signal. The resulting signal is applied to the RF input of the bias-T at the laser mount.

Both sections of coaxial cable used to set delay times contain adjustable length coaxial lines (General Radio Co. 874-LK10L). These devices, somewhat resembling a trombone slide, allow fine tuning of the cable delay over a range of 310 ps. The

delay line (B in Fig. 4.5) located immediately after the photodetector sets the control loop latency. Its length is chosen to provide a total latency 19.1 nanoseconds, *i.e.*, equal to τ_D . The second delay line (D in Fig. 4.5), which sets the orbit period, is adjusted to minimize the control error signal inside the domain of control. A control delay of 19.33 ± 0.05 ns appears to minimize the error signal throughout the experimentally observed domain of control.

4.2.2 Procedure for Measuring Delays

In order to correctly implement the modified TDAS control scheme, two path lengths must be carefully determined in order to obtain the appropriate time delays τ_P and τ_D . Different techniques are appropriate for determining τ_P and τ_D since the former is due entirely to propagation through coaxial cable while the latter includes phase shifts due to amplifiers and filters, and propagation through both free space and coaxial cable. Therefore I describe each method separately.

The path that produces the time delay τ_P is the length of cable between the power splitter and the - input port of the hybrid minus the length between the splitter and the + input port. The delay associated with this path is determined by applying a sinusoidal voltage to the input of the splitter and observing the signal at the Δ port of the hybrid. The transfer function through the splitter-delay-hybrid combination is derived by assuming an input of $V_{in} = V_0 e^{i\omega t}$ and a response in the form $V_{out} = V_{\Delta} e^{i\omega t}$ where V_{Δ} is an amplitude to be determined. Inserting these functions into Eq. 4.4, including a factor of $1/\sqrt{2}$ due to the splitter, and assuming

the delay of one path relative to the other is τ gives

$$\begin{aligned} V_{\Delta} e^{i\omega t} &= \frac{1}{2} (V_0 e^{i\omega t} - V_0 e^{i\omega(t-\tau)}) , \\ V_{\Delta} &= \frac{V_0}{2} (1 - e^{-i\omega\tau}) , \end{aligned} \tag{4.6}$$

$$\left| \frac{V_{\Delta}}{V_0} \right| = \sin^2 \left(\frac{\omega\tau}{2} \right) . \tag{4.7}$$

From Eq. 4.7, it can be seen that the transfer function has notches at all integer multiples of $1/\tau$. The location of the first notch is determined by analyzing the output of the Δ port with a spectrum analyzer with resolution bandwidth of 30kHz. The resulting uncertainty in the delay time is on the order of 0.01 ns.

The path that produces control loop latency of τ_D contains the entire controller including propagation through the interferometer, splitter, hybrid, cables, capacitors, and amplifier. Many of these components add phase delay in addition to propagation delay. Therefore, a direct measurement of the propagation distance only gives an order-of-magnitude estimate of the delay time. To get a more accurate measure of the delay, I take advantage of the fact that the active interferometer without external modulation oscillates at a fundamental frequency very close to $1/\tau_D$. By blocking the detector at the first port of the interferometer and removing the delay line from between the splitter and hybrid, I create a new feedback loop. I increase the gain until oscillations appear. The signal from the directional coupler (labelled F in Fig. 4.5) is measured by a spectrum analyzer to determine the frequency of oscillation. I estimate the error in the delay determined in this manner to be 0.2 ns or less.

4.2.3 Observation of Control

I characterize the effect of the controller on the experimental system in two ways. First, I examine the changes in the power spectrum of the interferometer output as

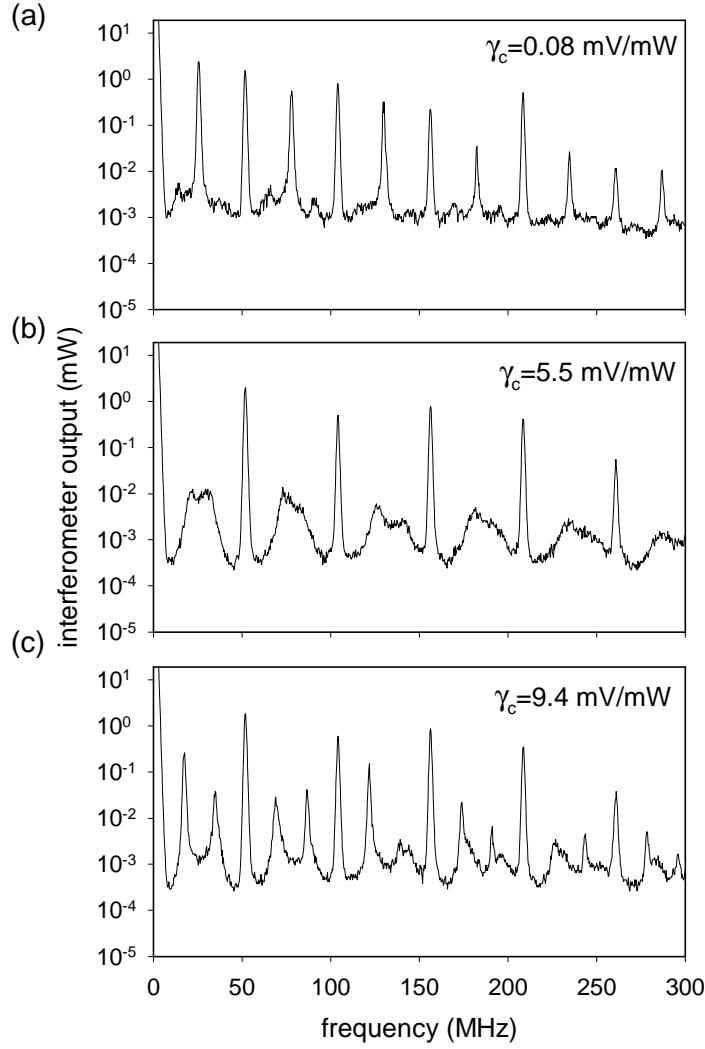


Figure 4.6: Typical experimental power spectra recorded when the feedback gain $\gamma = 12.4$. (a) The control gain $\gamma_c = 0.08$ is small enough that the spectrum is indistinguishable from that of the system with no control. (b) The control gain $\gamma_c = 5.5$, well within the domain of control. The large peaks at half-integer multiples of the fundamental frequency are suppressed more than 20 dB below their uncontrolled amplitude and the broad background falls several dB below its uncontrolled level. (c) The control gain $\gamma_c = 9.4$, new sideband frequencies appear around the fundamental frequency and its harmonics indicating control is no longer effective.

the control gain is varied. Then I estimate the domain of control by examining the size of the error signal.

To observe the influence of the controller on the system in the frequency domain, the signal from the directional coupler in the feedback loop (labeled B in Fig. 3.3) is amplified and sent to a spectrum analyzer. Figure 4.6 shows a set of typical power spectra recorded when the feedback gain $\gamma = 12.4$ mV/mW. In Fig. 4.6(a), the control gain $\gamma_c = 0.08$ mV/mW, a small enough value that the spectrum is indistinguishable from that of the system with no control. Dominant peaks, located at integer and half-integer multiples of the fundamental frequency, rise out of a broad background indicating chaotic oscillation. In Fig. 4.6(b), $\gamma_c = 5.5$ mV/mW. The large peaks at half-integer multiples of the fundamental frequency are suppressed more than 20 dB below their uncontrolled amplitude. Also, the broad background falls several dB below its uncontrolled level. The system at this point is well within the domain of control. In Fig. 4.6(c), where $\gamma_c = 9.4$ mV/mW, new sideband frequencies appear around the fundamental frequency and its harmonics indicating control is no longer effective. The appearance of sidebands as the control gain is increased to a value beyond the domain of control has been observed in an experimental study of the original TDAS method [49].

A broader view of the effect of the controller is obtained by measuring the domain of control. To do this, I use the signal from the directional coupler labelled F in Fig. 4.5 as a measure of the control error signal. When the feedback gain is set to a low value where the system oscillates at the fundamental frequency, the root mean square value of the error signal is 3.5 ± 1 millivolts. This signal is due to noise from the laser and amplifiers and to imperfections in the controller. I consider this level a good estimate of the error signal I can expect when the system is within the domain of control and choose the cutoff value to be just slightly larger at 4.2

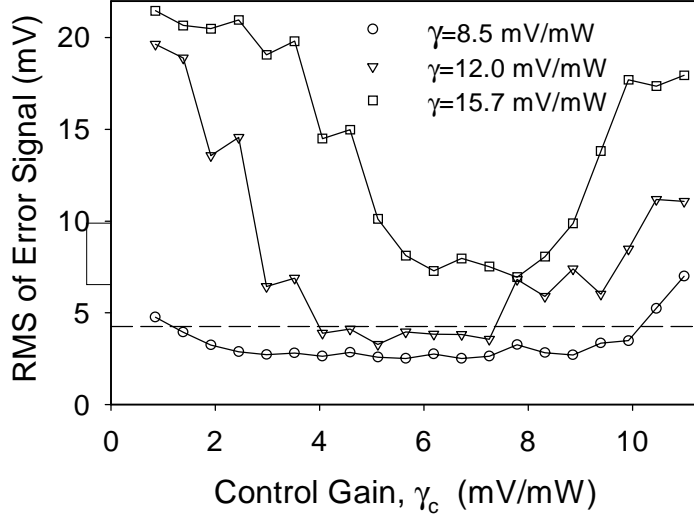


Figure 4.7: Experimentally measured average error signal at three different gain values. The dashed line shows the cutoff of 4.2 mV chosen to define the domain of control.

mV. I vary the feedback gain and control gain over a wide range, recording the root mean square value of the error signal at several points. Those points where the error signal average is below the cutoff are considered to be within the domain of control.

Data collection is automated using a personal computer and digital oscilloscope. The computer and oscilloscope communicate through a GPIB interface. The computer contains two analog outputs that are used to set γ and γ_c . After setting the gain values, the computer directs the digital oscilloscope to record a time series of 2,500 points at a sample rate of 500 MS/s and calculate the root mean square value. This value is relayed to the computer for storage and the gains are adjusted to the next value.

Three data sets collected in this manner are shown in Fig. 4.7. Each set is

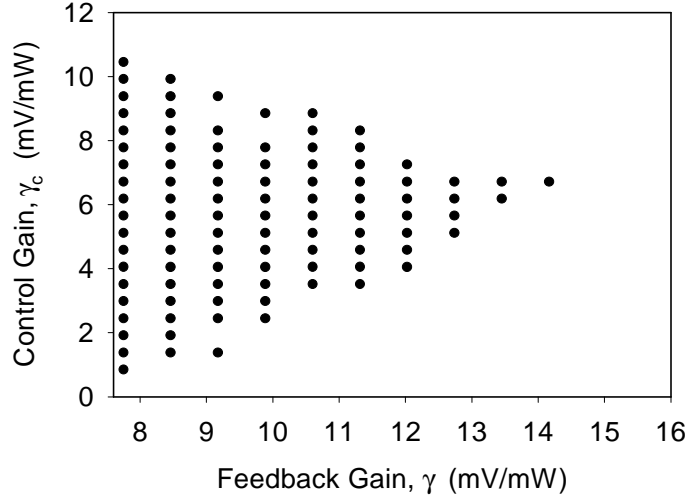


Figure 4.8: Experimentally measured domain of control. At each point, the root mean square of the error signal was compared with a cutoff value. The black dots mark points below the cutoff.

recorded with a different feedback gain. First, the circles show the error signal when $\gamma = 8.5$ mV/mW. At this gain the uncontrolled system is just above the transition from oscillation at the fundamental frequency to oscillation at half the fundamental frequency. Over a large range of γ_c , the error signal is below the cutoff value marked by the dashed line. The triangles show the average error at a higher gain where $\gamma = 12.0$ mV/mW. At this feedback gain, the uncontrolled system displays oscillations with a strong frequency component at half the fundamental frequency and a broadening background including a peak at one fourth the fundamental frequency. Only in a relatively small part of the range of γ_c does the error signal remain below the cutoff. Finally, at a high gain value of $\gamma_c = 15.7$ mV/mW, where the oscillations of the uncontrolled system are broadband, the squares show that, although the error signal does display a minimum, the error signal never falls below the cutoff. The system is considered to be outside the domain of control at these points.

Chaos Control Method	Orbit Period, τ_P	Control Loop Latency, τ_ℓ
TDAS [49, 72]	99 ns	<30 ns
ETDAS [49, 72]	99 ns	<120 ns
Pulsewidth Modulation [63]	52 ns	4.4 ns
Modified TDAS	19.33 ns	19.1 ns

Table 4.1: Shortest period orbits controlled experimentally in chaotic systems. The modified TDAS method described in this chapter is used to stabilize the shortest timescale dynamics reported to date. Note that with this method the latency need not be small compared to the period of the orbit.

Having explained the process by which I quantify the effect of the controller, I now present my experimental estimation of the control domain. Figure 4.8 shows all points within the range of γ and γ_c at which the error signal was observed to be below the cutoff. The estimated domain has a triangular shape such that the range of effective control gains decreases approximately linearly as the feedback gain is increased. As might be expected, the domain is very wide at feedback gain values where the uncontrolled system is either periodic or only slightly chaotic. As the feedback gain increases and the system becomes more chaotic, the domain is thinner but still significant. Control apparently fails completely for feedback gain values where the uncontrolled system shows a broad and nearly flat spectrum (roughly $\gamma = 14.5$ mV/mW). A few “holes” appear at the edges of the domain where the error signal is just above the cutoff. Such behavior is typical of a noisy system near a stability threshold.

The experimentally observed domain of control shown in Fig. 4.8 extends from the period-2 region into the chaotic regime where the period-2 frequency is still quite large noted in Table 3.3. In the chaotic region, the modified TDAS control method successfully stabilizes a periodic orbit with a period of 19.33 ns. In Table 4.1, this result is compared with the three shortest period experimentally stabilized orbits of chaotic systems reported in the literature. The period of the orbit stabilized

here is less than half the period of the next fastest orbit. Also given in Table 4.1 are the experimentally successful control loop latencies for each method. Note that the latency of the modified TDAS controller is nearly equal to the stabilized orbit period. Only one other chaos control method, ETDAS, has demonstrated a similar tolerance to latency. Experimental implementation of ETDAS is likely to be more challenging than the modified TDAS method in many cases because it can require a predistortion stage in the controller [49]. Thus, the modified TDAS method provides a balance of design simplicity and tolerance to latency.

4.3 Mathematical Model of Interferometer with Controller

To gain more insight into the experimental results presented above, I develop a mathematical model of the controlled system. Based on the detailed description of the controller implementation in the last subsection, the interferometer model developed in the previous chapter is now easily augmented to include the modified TDAS controller. In this subsection, I add control to the model and then use it to predict the domain of control.

According to Eq. 3.43, the power P_2 emitted by the second port of the interferometer is given by

$$P_2(t) = \frac{\zeta_F}{2} P(t) \{1 - b \sin [\alpha (P(t) - P_0)]\}, \quad (4.8)$$

where $P(t)$ is the power emitted by the laser and b , α , P_0 , and ζ_F are as given in Sec. 3.2.3. A fraction ζ_C of this power falls on the detector, which converts it to current with a sensitivity of $\rho = 0.44$ mA/mW. A resistor $r = 50$ Ω converts the current into the voltage

$$V_{\text{det}}(t) = \frac{\rho r \zeta_C \zeta_F}{2} P(t) \{1 - b \sin [\alpha (P(t) - P_0)]\}. \quad (4.9)$$

This voltage is delayed and split into two separate signals. One of these is delayed again. Then the two are recombined by the hybrid junction according to Eq. 4.4 producing a voltage

$$V_{hybrid}(t) = \frac{\rho r \zeta_C \zeta_F}{4} \{P(t) [1 - b \sin [\alpha (P(t) - P_0)]] - P_{\tau_P} [1 - b \sin [\alpha (P_{\tau_P} - P_0)]]\}, \quad (4.10)$$

where I use the notation $P_\tau = P(t - \tau)$ and I have ignored for the moment all other propagation delays. A directional coupler splits off 1% of the power from this signal reducing the voltage by a factor of 0.99. The capacitors and amplifier in the control loop are chosen to match the components in the interferometer feedback loop. This is done so that the control signal receives the same bandpass filtering as the feedback signal. The entire system is then described by the equations

$$\tau_L \dot{V} = -V + \gamma P_{\tau_D} \{1 + b \sin [\alpha (P_{\tau_D} - P_0)]\} + \gamma_c c(t), \quad (4.11)$$

$$\dot{P} = -\frac{1}{\tau_H} (P - P_0) + \kappa \left[\dot{V} + \Omega_m V_m \cos (\Omega_m t) \right], \quad (4.12)$$

$$c(t) = \{P_{\tau_D} \{1 - b \sin [\alpha (P_{\tau_D} - P_0)]\} - P_{\tau_D + \tau_P} \{1 - b \sin [\alpha (P_{\tau_D + \tau_P} - P_0)]\}\}. \quad (4.13)$$

The quantity $c(t)$ will be used below as a measure of the effectiveness of the controller. The control gain γ_c is given by

$$\gamma_c = \frac{\rho r \zeta_c \zeta_F \xi}{4}. \quad (4.14)$$

I use this model to obtain a theoretical estimate of the domain of control. For the original TDAS scheme, tools have been developed to locate or approximate the domain of control that don't require integration of the full set of equations governing the system and controller. However, these techniques have not been generalized to time-delay dynamical systems or to include latency. Therefore, I resort to direct

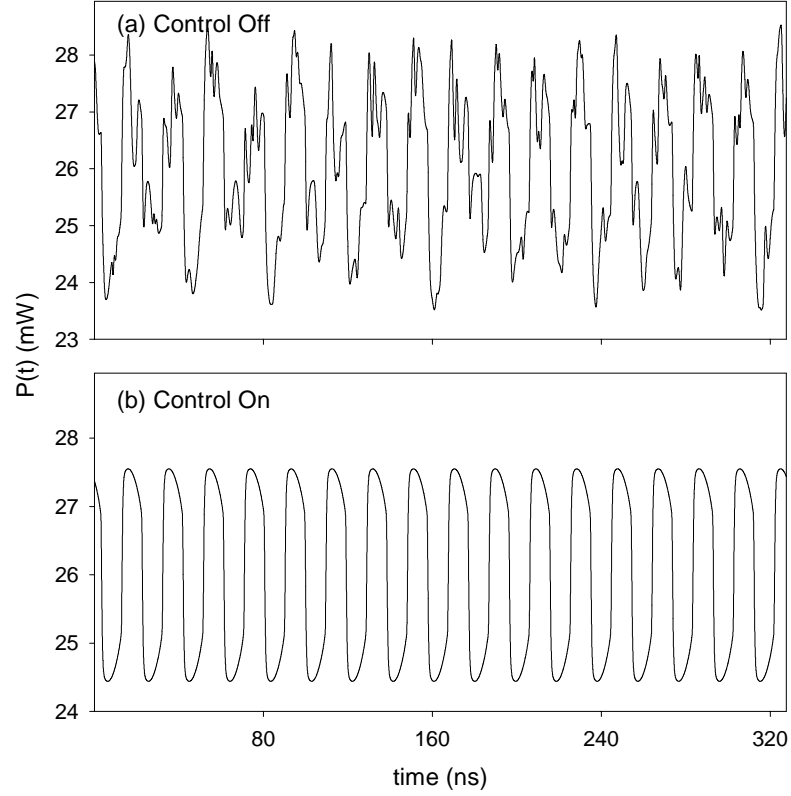


Figure 4.9: Time series of power emitted from created by numerically integrating model of inteferometer and controller. The feedback gain is $\gamma = 14.0$ mV/mW. (a) Uncontrolled irregular oscillation with $\gamma_c = 0$ mV/mW. (b) Stabilized oscillation near the fundamental frequency with $\gamma_c = 4.5$ mV/mW.

numerical integration of Eqs. 4.11-4.13 in order to locate the domain of control. I use the fixed step-size an Adam-Bashforth-Moulton predictor-corrector algorithm [101].

There are some difficulties with this approach. First, the initial conditions of the system consist of two functions (one each for P and V) defined on the interval $[-\tau, 0]$. In a phase space of infinite dimensions, there is no obvious method for sampling a large number of initial conditions in order to determine where a typical trajectory will evolve. Moreover, it has been observed that the basin of attraction of a stabilized UPO shrinks as the boundary of the domain of control is approached. Since only a finite number of initial conditions can be investigated, this approach necessarily underestimates the true domain of control to some extent. For points well within the domain of control, I choose a sine wave with the frequency of the orbit to be controlled as the initial condition of the system with the intention of starting the system close to the desired orbit in phase space. For points closer to the boundary of the domain of control, I use a time series of the controlled orbit near the center of the domain of control as the initial condition.

A second difficulty is that generally the period of the unstable orbit τ_P is not commensurate with the feedback delay, τ_D . Since the integration step size is chosen such that an integer number of steps fit within τ_D , the same is not true for τ_P . The period τ_P can only be specified to within the accuracy of the integration step size. As a result of this error in τ_P , the error signal never goes to zero. In spite of these issues, I proceed to use numerical integration to estimate the domain of control for though it may be a crude tool, it happens to be the only one available at this time.

Typical results from the integrated model are shown in Fig. 4.9. The power emitted by the laser is plotted as a function of time with and without control.

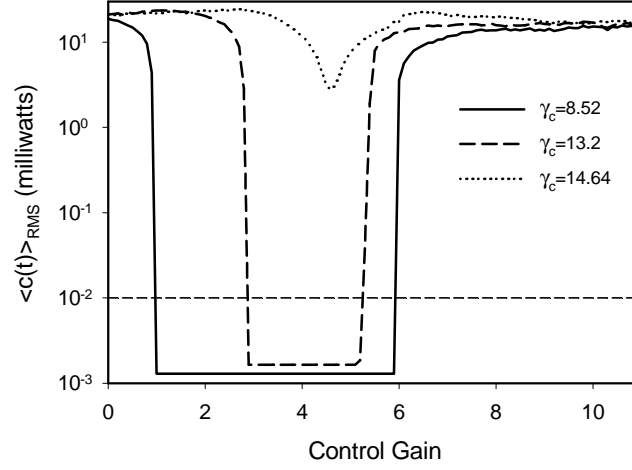


Figure 4.10: Root mean square of error signal from model. Domain of control is estimated by recording control gain values that produce an error signal below a cutoff value. The dashed horizontal line shows the cutoff at 0.01 mW.

With $\gamma = 14.0$ mV/mW, the uncontrolled system (see Fig. 4.9(a)) displays chaotic oscillations (see the preceding chapter for more description of the uncontrolled dynamics). When the control is applied (see Fig. 4.9(b) where $\gamma_c = 4.5$) a periodic oscillation appears.

I adjust the control delay to minimize the root mean square value of the error signal. In general, the period of an unstable orbit in a dynamical system may change as a bifurcation parameter is adjusted. However, throughout the range of feedback gains from 8-14.5 mV/mW, the control delay that produced a minimum in the error signal was a constant value of 19.315 ns to within the 2.5 ps resolution of the integration. The effects of varying τ_P will be investigated in more detail in the next chapter.

To locate the domain of control, I generate many time series like those in Fig. 4.9 using a range of values of γ and γ_c both inside and outside the domain of control.

From each time series, I calculate the root mean square value of $c(t)$ as defined in Eq. 4.13. Figure 4.10 shows how the average error signal changes as the control gain is varied at three different values of γ . The dotted line gives $\langle c(t) \rangle_{rms}$ as a function of the control gain with $\gamma = 8.52$ mV/mW. Near $\gamma_c = 0$ mV/mW, the control error is high indicating that the system is outside the domain of control. Around $\gamma_c = 1.0$ mV/mW, $\langle c(t) \rangle_{rms}$ abruptly falls two orders of magnitude to a value close to zero. The fact that it does not go all the way to zero (within machine precision) is due to the fact that there is some error in τ_P , as mentioned earlier. Near $\gamma_c = 6.0$ mV/mW, the $\langle c(t) \rangle_{rms}$ again changes abruptly, this time increasing rapidly by two orders of magnitude. A similar behavior is displayed by the system with $\gamma = 13.2$ mV/mW. The long dashed line in Fig. 4.10 shows $\langle c(t) \rangle_{rms}$ in this case. At two points, $\langle c(t) \rangle_{rms}$ jumps abruptly. Between these points the error signal is very small. The dotted line in Fig. 4.10 shows quite different behavior in the case where $\gamma = 14.64$ mV/mW. Although a minimum occurs, the decrease is less than an order of magnitude and no abrupt jump occurs.

I interpret those regions where the gain is extremely low as being within the domain of control. In order to define the boundaries of the estimated domain, a cutoff value of $\langle c(t) \rangle_{rms}$ must be chosen. Since the error signal falls so rapidly when control is achieved, the resulting domain estimate should not depend sensitively on the cutoff chosen. Based on the appearance of time series from borderline values of γ_c , I set the cutoff at 10^{-2} mW. The resulting estimated domain of control is shown in Fig. 4.11.

The estimated domain is qualitatively quite similar to the domain estimated experimentally (see Fig. 4.8). The shape is triangular showing the linear decrease in the range of effective control gains as the feedback gain is increased. Control fails completely near $\gamma = 14.5$ mV/mW. As in the experiment, this is the beginning of

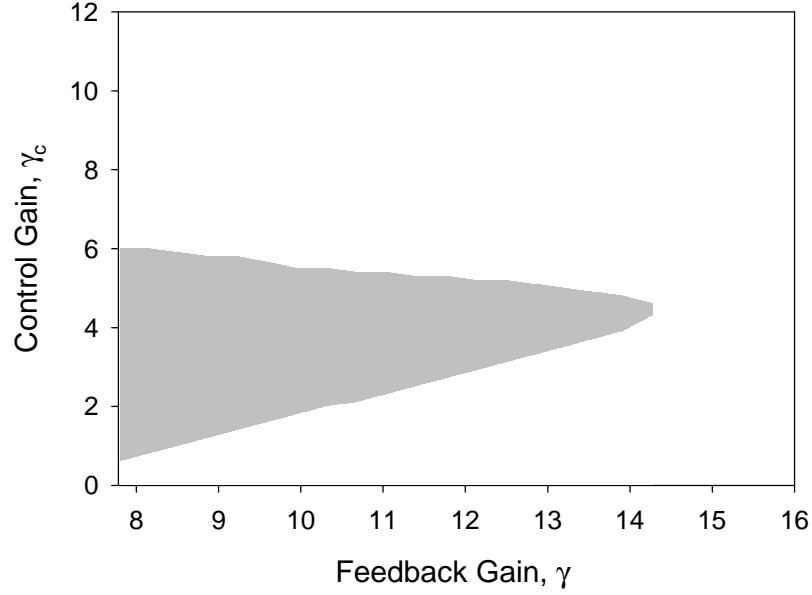


Figure 4.11: Domain of control of modified TDAS applied to the model of the active interferometer.

the region where the dynamics become very broad band.

4.4 Summary

In this chapter, I have proposed a modification of the TDAS control method suitable for fast, time-delay chaotic systems. In this new method, the control loop latency is intentionally set to equal the time delay. I have demonstrated this method experimentally by applying it to the active interferometer with bandpass feedback and external modulation. I developed a model of the system with control that produced behavior in good agreement with the experiment. Two time delays appear in the control term in the modified TDAS method. In the next chapter, I will examine

the effect on control of variation of these delays.

Chapter 5

Influence of Delay Mismatch in the Modified TDAS Control Method

The modified TDAS control scheme introduced in the preceeding chapter for controlling time-delay systems requires adjusting two time delays in the control loop. First, the control perturbation consists of the difference between the interferometer output at two times separated by a time interval which, in this chapter, I will refer to as the *control time delay*. Ideally, the control delay is equal to the period of the orbit to be controlled, τ_P . The second delay time in the controller is the control loop latency, which is set to equal the time delay τ_D of the feedback loop of the uncontrolled system. The modified TDAS control method was motivated by the observation that many time delay systems have a strong peak in the auto correlation function around τ_D . Since this peak has a finite width and is not centered exactly on τ_D , it is interesting to ask how varying the latency around τ_D affects control. Similarly, how does the varying the control time delay away from the true orbit of the period affect control?

Studies of the original TDAS control method found that variation of these delays produced quite distinct effects on control. Effective TDAS control strongly depends on the careful matching of the control time delay with the period of the unstable orbit [49, 113]. For example, in an experimental study of controlling a diode resonator using TDAS, a dramatic increase in the error signal was observed when the control time delay differed by a few hundred picoseconds from the orbit period of 100 ns. On the other hand, the error signal remained small while the control loop latency was adjusted by several nanoseconds.

The theoretical explanation for these differing effects is as follows. With the control time delay exactly equal to the period of the desired orbit, the error signal is identically zero when the system is on the orbit. Thus the unstable orbit of the system without control is also an orbit of the system with control. Any mismatch between the control time delay and the orbit period results in a non-zero error signal when the system is on the desired orbit. Therefore, the desired orbit of the system without control is not a periodic orbit of the system with control applied. However, the controlled system will follow a periodic orbit that differs only slightly from the desired orbit of the uncontrolled system if the mismatch is small enough [114]. This so-called fictitious orbit has a shape, period, and stability that tend towards those of the uncontrolled orbit as the mismatch tends toward zero. Since the period of the fictitious orbit differs from the control time delay, the error signal tends toward zero as the mismatch is decreased. Thus, the error signal is expected to have a minimum when the control delay is exactly τ_P and to increase smoothly as the mismatch is increased.

Variation of the control loop latency produces a different response from the controller. Latency is ideally zero in TDAS control, but experiments have shown successful control with non-zero latency [49]. Positive control loop latency does not prevent the error signal from going to zero on the desired orbit. Therefore, no matter how much latency is present, the orbit of the uncontrolled system is always an orbit of the controlled system (assuming the control delay is properly set). However, the latency does affect the stability of the orbit [65, 66, 115]. Thus, the error signal is expected to be zero as long as the latency is within some stability domain but to grow abruptly when the a stability boundary is crossed.

The modifications to TDAS introduced for controlling time-delay systems do not alter the basic role played by the control delay and the latency. Therefore,

qualitatively similar results are expected when these delays are varied around their nominal values. As in TDAS, the desired orbit of the uncontrolled system is only an orbit of the system with control if the control time delay exactly equals τ_P . The error signal should have a unique minimum when the control time delay equals τ_P . Also, as in TDAS, control should be stable in a finite range of latency around the nominal value of $\tau_L = \tau_D$.

To test these expectations, I investigate the influence of variation control loop latency and control delay from their nominal values on the modified TDAS control method as applied to the active interferometer with delayed bandpass feedback. In Sec. 5.1, I describe simulations using the mathematical model developed in the preceeding chapters. In Sec. 5.2, I present experimental results and a comparison with the model. Both the experimental and simulated results are consistent with the conclusions drawn above regarding the role of the delays in the control method. In Sec. 5.3, I discuss the implications of these results on the practicality of the modified TDAS method.

5.1 Simulations

The active interferometer with delayed bandpass feedback and modified TDAS control is described by the equations

$$\tau_L \dot{V} = -V + \gamma P_{\tau_D} \{1 + b_1 \sin [\alpha (P_{\tau_D} - P_0)]\} + \gamma_c c(t), \quad (5.1)$$

$$\dot{P} = -\frac{1}{\tau_H} (P - P_0) + \kappa \left[\dot{V} + \Omega_m V_m \cos (\Omega_m t) \right], \quad (5.2)$$

$$c(t) = \{P_{\tau_D} \{1 - b_2 \sin [\alpha (P_{\tau_D} - P_0)]\} - P_{\tau_D + \tau_P} \{1 - b_2 \sin [\alpha (P_{\tau_D + \tau_P} - P_0)]\}\}, \quad (5.3)$$

derived in Chapters 3 and 4. The quantity $c(t)$ is referred to here as the *error signal*. For all simulations described in this chapter, I set the feedback loop gain

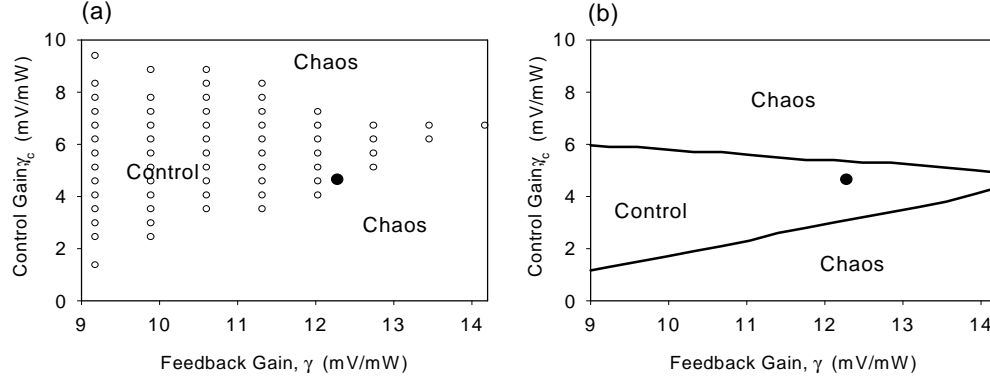


Figure 5.1: (a) Experimental and (b) theoretical domains of control as determined in the previous chapter. The black circle shows the point in each domain at which the data in this chapter is collected.

$\gamma = 12.28$ so that the uncontrolled system displays chaotic oscillations according to Sec. 3.5. The control gain is set to $\gamma_c = 4.65$, placing the system within both the experimental and theoretical domains of control as shown in Fig. 4.8. All other parameters are as given in Ch. 4. In particular, the feedback delay $\tau_D = 19.1$ ns.

I first consider variations of the control time delay and fix the control loop latency at $\tau_L = 19.1$ ns. I numerically integrate Eqs. 5.1 and 5.2 using nearly the same procedure as described in Sec. 4.3. However, I use a time step ten times smaller. As explained in Sec. 4.3, the integration time step is chosen so that an integer number of steps equals the feedback delay time, τ_D . This means that, in general, the period of the orbit τ_P is not equal to an integer number of integration steps. However, as the integration step size is reduced, an integer number of steps can better approximate the true value of τ_P . Using a time steps of 2.5 ps, I can approximate the true orbit period to within less than 0.02% (assuming the true period is within 1 ns of τ_D).

At each of several values of the control time delay, I quantify the control error

by calculating the root mean square average of $c(t)$. To obtain each average value, I

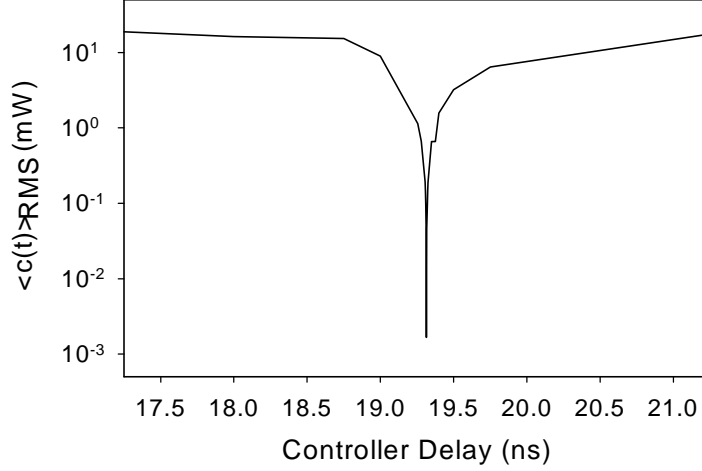


Figure 5.2: Average error signal in the modified TDAS controller as control loop latency is varied in the mathematical model. The feedback gain $\gamma = 12.28$ and the control gain $\gamma_c = 4.65$.

first integrate through a transient of duration $10,000\tau_D$ and then average the value of $c(t)$ over the next $100\tau_D$. Figure 5.2 shows $\langle c(t) \rangle$ on a logarithmic scale as a function of control time delay. As expected, a very sharp minimum is observed. The control time delay is equal to 19.315 ns at the minimum. Adjusting the control time delay just 7.5 ps above or below this value results in an increase of $\langle c(t) \rangle$ by two orders of magnitude. Adjusting the control delay by an additional 100 ps above or below results in another order of magnitude increase in the error signal. Finally, at roughly 1 ns to either side of the 19.315 ns, $\langle c(t) \rangle$ is four orders of magnitude above the minimum value. The sharp minimum and smooth increase in the error signal as the control delay is moved away from 19.315 ns is consistent with the theoretical picture of a gradual distortion of the orbit of the uncontrolled system.

Next, I investigate the influence of the control loop latency on the effectiveness

of the controller. I keep the value of the control time delay fixed at 19.315 ns and quantify the effectiveness of the controller by determining $\langle c(t) \rangle$ while I vary the latency. The result is shown in Fig. 5.3. Over a range of values from 0 to 40 ns, the average value of $c(t)$ is uniformly high except for a deep notch stretching from 19.0 ns to 19.45 ns where the error drops abruptly by four orders of magnitude to the minimum value observed in the previous paragraph. This finite region where the error is very small and the abrupt transitions at the edges of the region where the error signal increases dramatically are consistent with theoretical description given above based on results from the original TDAS method.

It is notable that control is not effective in the model when the latency approaches zero. A theoretical study has predicted there may be cases where ETDAS control is only effective in some non-zero range of latency but no example has appeared in the literature [115]. Also notable is the fact that control fails when the latency is equal to $2\tau_D$. Apparently, at least at this control gain value, the memory of the system decays too rapidly for successful control with a latency equal to multiples of τ_D .

5.2 Experimental Observations

In this section I describe the experimentally observed effects of varying the delays in the modified TDAS control method when applied to the active interferometer with delayed bandpass feedback. The experimental setup is identical to that described in Sec. 4.2. I set the gain $\gamma = 12.28$ so that the uncontrolled system displays chaotic oscillations. The control gain $\gamma_c = 4.65$, placing the system well within the experimentally determined domain of control shown in Fig. 4.8. Following the order of presentation of the preceding section, I will first consider variations of the control delay time followed by variations of the control loop latency.

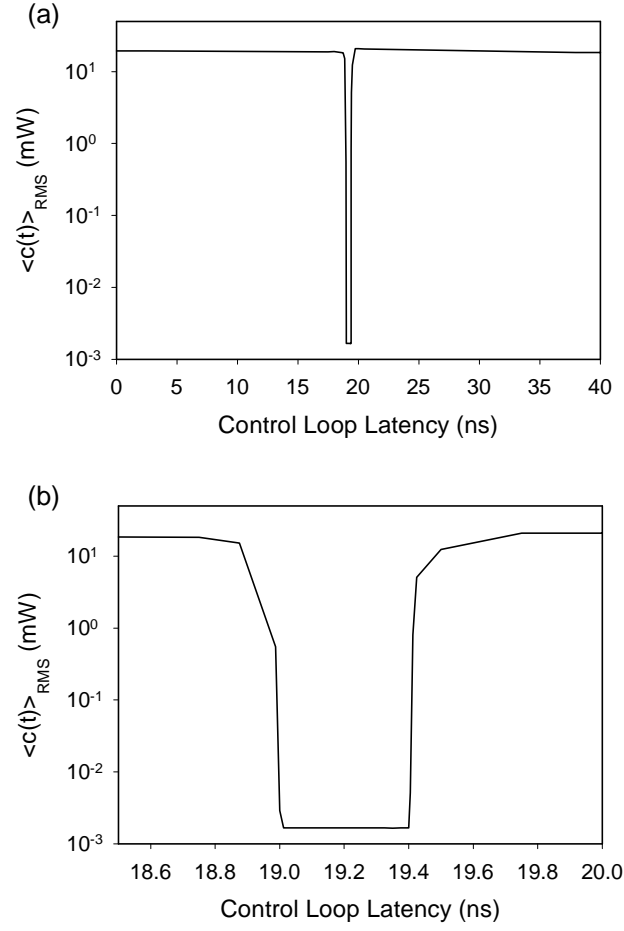


Figure 5.3: Average error signal in the modified TDAS controller as control loop latency is varied in the mathematical model. The feedback gain $\gamma = 12.28$ and the control gain $\gamma_c = 4.65$. A wide range of latency from zero to over $2\tau_D$ is shown in (a). The region around the minimum is shown in more detail in (b).

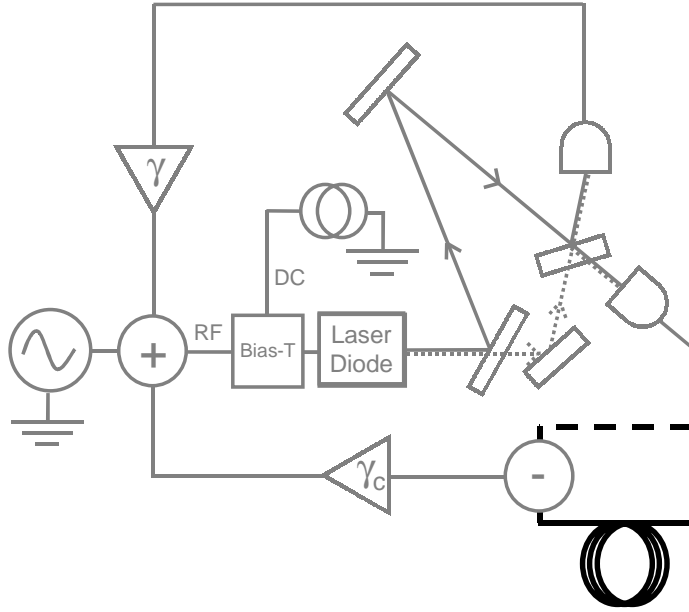


Figure 5.4: The control delay is determined by the difference in propagation time through the two highlighted sections. The direct path is shown as a heavy dashed line. The delayed path is shown as a heavy solid line.

The control delay is determined physically by the difference in propagation time through the two paths connecting the splitter labelled C in Fig. 4.5 and the hybrid coupler labelled E. These two paths are shown schematically in Fig. 5.4. Experimentally, this path length is varied by adjusting the length of the delay line located just after the splitter. Coarse adjustments are made by adding or subtracting fixed lengths of RG-58 coaxial cable. A 20 cm length of cable adds approximately 1 ns to the control loop latency. Fine adjustments are made using a constant impedance, variable length delay line with a tunable range of 310 ps (General Radio Co. 874-LK10L).

To quantify the effect of varying the control delay, I record the root mean square average of the error signal. A high-speed digital oscilloscope records 2,500 samples

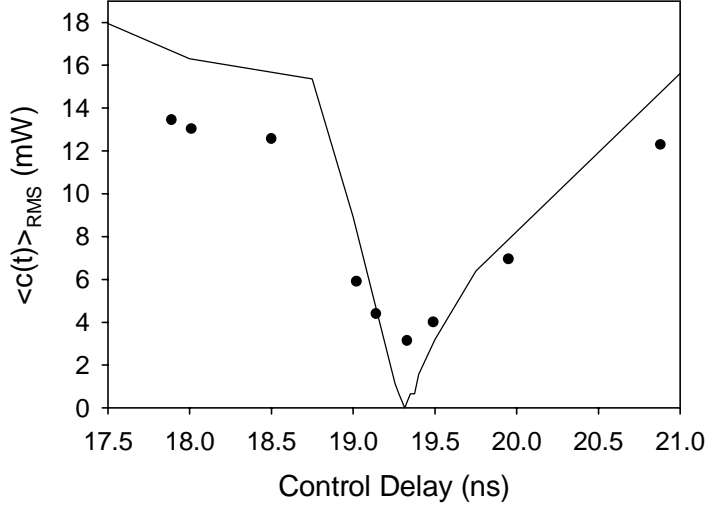


Figure 5.5: Average error signal in the modified TDAS controller as the control time delay is varied. The circles show experimental values. The feedback gain $\gamma = 12.28$ and the control gain $\gamma_c = 4.65$. The solid line shows the simulation reproduced from Fig. 5.2.

of the error signal at a rate of 1 GS/s and then calculates the root mean square. In Fig. 5.5, the circles show the resulting values of $\langle c(t) \rangle$. The solid line is the simulated result from Fig. 5.2 reproduced on a linear scale. A minimum appears at 19.33 ns where the error signal drops to the noise level as defined in Sec. 4.2.3. The error signal rises by a factor of two within 0.5 ns on either side of the minimum. The width of the minimum is comparable to that observed when the control loop latency is varied. Although no sharp minimum is apparent as in the simulations, the gross shape of the experimentally observed minimum agrees with the simulated minimum.

I next investigate the effect of varying the control loop latency. In the active interferometer with bandpass feedback, the control loop latency is the total propagation time of the signal as it travels through the closed loop formed by the controller,

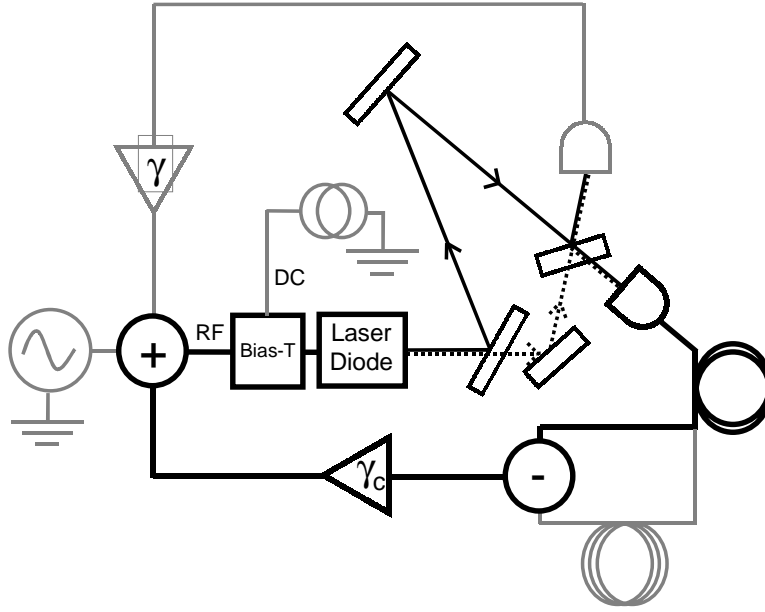


Figure 5.6: Schematic diagram of active interferometer with modified TDAS control. The control loop latency is the propagation time around the path shown here by the heavy black line.

laser and interferometer. This path is shown schematically in Fig. 5.6 by the heavy black lines. The path length is varied by adjusting the length of the delay line located just after the detector. As in the previous experiment, a variable delay is included for fine adjustments. I set the control time delay to 19.33 ns, the location of the observed minimum in Fig. 5.5.

The result is shown in Fig. 5.7. The error signal displays a minimum at 19.1 ns reaching the estimated noise level of ~ 4 mV (see Sec. 4.2.3). It roughly triples in size 1 ns above or below the minimum. The transition from the region where the error signal is small to the region where it is large is somewhat smoother than in the simulated result. However, the minimum is clearly much wider than was observed when the control time delay was varied as predicted above.

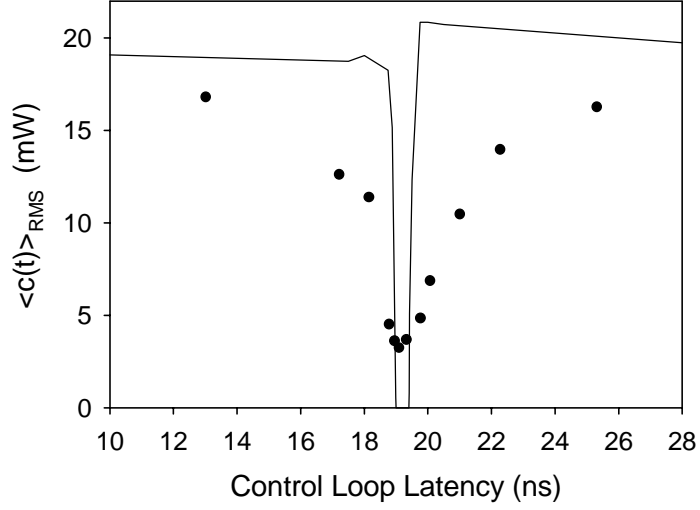


Figure 5.7: Average error signal in the modified TDAS controller as the control loop latency is varied. The circles show experimental values. The feedback gain $\gamma = 12.28$ and the control gain $\gamma_c = 4.65$. The solid line shows the simulation reproduced from Fig. 5.3.

5.3 Discussion

In this chapter, I examined the role of the control time delay and control loop latency in the modified TDAS control method. The effect on the control error signal when each of these quantities was varied around its nominal value was observed in simulations and in an experiment. The success of control was found to depend more sensitively on the control time delay than on the latency. The accuracy required in setting these delays is a central consideration in determining the practicality of the method.

My observations suggest that the latency needs to be known only to within several percent of its true value to achieve control in many situations. Any value within this finite range results in successful control with a very small error signal. Therefore, it does not appear to be a significant barrier to the practical application

of the method. The fact that the range of latencies over which control is successful is located around τ_D rather than around zero in the original TDAS method constitutes the primary advantage of the modified technique. Roughly speaking, a controller based on the original TDAS method applied to a fast time-delay system will require faster components than those used in the implementation of the system itself. On the other hand, a controller based on the modified TDAS method can be constructed with similar components to those used in the system itself.

The situation is more complicated with regard to the control time delay. The error signal is very sensitive to this parameter and goes to zero only at when the control time delay is precisely equal to the period of the uncontrolled orbit. In systems such as the active interferometer examined here, the presence of noise obscures the very sharp minimum in the error signal. The usefulness of the technique for a noisy system then rests on whether the broader minimum in the error signal that is observable is deep enough for the application at hand. On the other hand, in systems that are subject to much lower noise levels, the sharp minimum makes the control method a useful tool for accurately determining the period of the unstable orbits of a chaotic system similar to schemes devised for automating the process of locating the correct period in the original TDAS method [116, 117].

Chapter 6

Conclusion

The ability to control fast chaotic systems is an important tool for building a fundamental understanding of the dynamics of these systems and for exploiting them in technological applications. This dissertation documents my investigation of controlling a fast chaotic time-delay system. To conclude this report, I review the major results reported in each chapter and suggest further experiments and applications.

6.1 Summary

The first two chapters of this thesis provide introductory and background material. In Chapter 1, I delineate the place of my research in the larger fields of nonlinear dynamics and physics. This general introduction is followed by a chapter-by-chapter preview of the thesis. In Chapter 2, I provide a more specific context for my work. I define the concept of control loop latency and illustrate it with a simple example of proportional control of a linear system. I show that the domain of control for this simple system is dramatically reduced as the control loop latency is increased. I then review the development of techniques for controlling chaos in general and fast chaos in particular.

In Chapter 3, I introduce a new fast chaotic opto-electronic device consisting of a semiconductor laser, a Mach-Zehnder interferometer, and a bandpass filtered delayed electronic feedback loop. The device offers a high degree of design flexibility at a cost much lower than other known sources of fast optical chaos. The nonlinearity in the system is determined by the path difference through the arms of the interferometer. The time scale of the chaotic dynamics is determined by a the

delay time and bandwidth of the feedback loop. Thus, both of these key characteristics of the system are easily accessible and manipulable. For example, by simply adjusting the feedback delay time in my experimental system, the fundamental frequency of oscillation can be set anywhere in range 30-103 MHz. In principle, the system could easily be modified to oscillate at 1-10 GHz. This flexibility makes the system suitable for laboratory studies of dynamics at slow speeds. I characterize the behavior of the system as the feedback loop gain is varied both when the system is running autonomously and when it is subject to external modulation. I develop a mathematical model of the system that reproduces the experimentally observed behavior. In later chapters of this thesis, the system serves as a testbed for a new method for controlling fast time-delay.

In Chapter 4, I propose a new method for controlling chaos in a fast time-delay system. The method is a modification of the TDAS control technique where the control loop latency is precisely set equal to τ_D , the feedback time delay in the uncontrolled system. I demonstrate this technique by applying it to the active interferometer with bandpass feedback described in the previous chapter. The domain of control is estimated experimentally and numerically. The experimental and theoretical results show good qualitative agreement. The domain is found to have a rather simple, triangular shape that pinches off at a high feedback loop gain. Prior to my work, the fastest controlled chaotic system reported in the literature had a characteristic oscillation frequency of 19 MHz with a control loop latency of 4.4 ns [63]. With the modified TDAS method, control is achieved when the fundamental frequency of oscillation is 51.8 MHz despite the much larger latency of 19.1 ns.

In Chapter 5, I investigate the role of the control time delay and control loop latency in the modified TDAS control method. Results from studies of the time delays in the original TDAS method are reviewed and their application to the mod-

ified TDAS method is discussed. I examine, through experiments and simulations, the effect of varying the control time delay and latency around their nominal values. The observed behavior is consistent with expectations based on the studies of the original TDAS method. The control time delay must be set exactly equal to the period of the desired UPO if the control perturbations are to vanish when the system is actually on the orbit. In contrast, the control loop latency may be adjusted within a finite range without affecting the success of control.

6.2 Future Directions

The two main contributions of this thesis to the field of nonlinear dynamics are the introduction of a flexible new source of fast optical chaos and a new method for controlling fast time-delay chaotic systems. Both of these innovations open the door to further investigations and applications.

Much work remains to be done to fully characterize the dynamics of the active interferometer with delayed bandpass feedback. In Chapter 3, I observed a wide range of behavior as the feedback gain was varied. A more complete picture would be provided by a careful study and classification of the bifurcations that occur between the first periodic oscillation and broad band chaos. It is also important to understand the complexity of the dynamics both as a function of the feedback gain and the time delay. Only a couple of studies of the dimension of systems with bandpass delayed feedback have been reported. In both cases, the estimated dimension was surprisingly high relative to similar systems with lowpass delayed feedback [44, 87].

The active interferometer with delayed bandpass feedback has many features that may make it a good candidate for uses in chaos-based communications applications. First, the use of a semiconductor laser facilitates its integration with

modern optical communication technologies such as optical fiber transmission, optical switching, etc. The visible wavelength of the diode laser (660 nm) used here was chosen for experimental convenience over the invisible infra-red wavelengths (1.3-1.5 μm) commonly used in fiber optic communications systems. However, redesign at communications wavelengths would be straight forward.

Second, chaos synchronization may be easier to achieve with this system. In general, high-quality synchronization requires nearly identical chaotic systems [118]. Important parameters of the active interferometer with delayed bandpass feedback, such as the nonlinearity and the delay time are accessible and easily fine tuned. The main potential obstacle to high-quality synchronization in this system is the phase noise of the diode laser [119].

Third, the use of external electrical modulation offers a means for encoding messages by techniques successfully demonstrated using much more expensive chaotic sources such as the erbium-doped fiber laser. The basic idea is to use the message as a driving signal for the chaotic system. The message gets wrapped up in the chaotic dynamics in a complicated way making extraction practically impossible without a synchronized receiver [27].

Another interesting application of the active interferometer may be the rapid generation of random numbers [120, 121]. A wide variety of computing applications rely heavily on random numbers. For example, random numbers are used as encryption keys to protect data from unauthorized decryption. The ever increasing speed of modern processors produces a need for physical systems that can generate the truly random numbers at fast and faster rates. A study of the statistical properties of the oscillations observed in the active interferometer is necessary to determine whether the system passes the standard tests for randomness.

The modified TDAS control method provides a new tool for the investigation

and exploitation of fast chaotic systems like the active interferometer with bandpass delayed feedback. In this thesis, a proof-of-concept experiment demonstrates the successful application of the technique. However, much more can be done to understand how and when it works. Theoretical methods for predicting the domain of control with more accuracy than simple numerical integration already exist for the original TDAS method [64]. An extension of these methods to the modified TDAS method is desirable. Also, the modified TDAS method could be experimentally tested with a more well-known chaotic system such as an electronic circuit implementation of the Mackey-Glass system [122]. The dependence of the dimension of this system on the time delay is well characterized and thus the effectiveness of this method in controlling high-dimensional chaos could be more precisely determined.

Bibliography

- [1] Gingerich, O., *The Eye of Heaven: Ptolemy, Copernicus, and Kepler*. New York: American Institute of Physics, 1993.
- [2] Kazunori, A., *Nonlinear dynamics and chaos in semiconductors*. Philadelphia: Institute of Physics Publishing, 2001.
- [3] Schöll, E., *Nonlinear spatio-temporal dynamics and chaos in semiconductors*. New York: Cambridge University Press, 2001.
- [4] Blümel, R., and W. P. Reinhardt. *Chaos in Atomic Physics*. New York: Cambridge University Press, 1997.
- [5] Henrard, J., and S. Ferraz-Mello, eds. *Impact of Modern Dynamics in Astronomy: Proceedings of the IAU Colloquium 172 held in Namur, Belgium July 1998*. Boston: Kluwer Academic, 1999.
- [6] Contopoulos, G. I., *Order and Chaos in Dynamical Astronomy*. Springer Verlag, 2002.
- [7] Beck, C., *Spatio-Temporal Chaos and Vacuum Fluctuations of Quantized Fields*. New Jersey: World Scientific, 2002.
- [8] Biró, T. S., S. G. Matinyan, and B. Müller. *Chaos and Gauge Field Theory*. New Jersey: World Scientific, 1994.
- [9] Milonni, P. W., M.-L. Shih, and J. R. Ackerhalt. *Chaos in laser-matter interactions*. Singapore: World Scientific, 1987.
- [10] Abraham, N. B., F. T. Arrechi, and L. A. Lugiato, eds. *Instabilities and Chaos in Quantum Optics II*. New York: Plenum Press, 1988.
- [11] Auerbach, D., P. Cvitanovic, J. P. Eckmann, G. Gunaratne, and I. Procaccia, Exploring chaotic motion through periodic orbits. *Phys. Rev. Lett.* 58:2387-2389, 1987.
- [12] Hunt, B. R., and E. Ott. Optimal periodic orbits of chaotic systems occur at low period. *Phys. Rev. E* 54:328-337, 1996.
- [13] Zoldi, S. M., Unstable Periodic Orbit Analysis of Histograms of Chaotic Time Series. *Phys. Rev. Lett.* 81:3375-3378, 1998.

- [14] Lathrop, D. P., and E. J. Kostelich. Characterization of an experimental strange attractor by periodic orbits. *Phys. Rev. A* 40:4028-4031, 1989.
- [15] Dolan, K. T., Extracting dynamical structure from unstable periodic orbits. *Phys. Rev. E* 64:026213 (9 pages), 2001.
- [16] Grebogi, C., E. Ott, and J. Yorke. Unstable periodic orbits and the dimensions of multifractal chaotic attractors. *Phys. Rev. A* 37:1711-1724, 1988.
- [17] Cvitanović, P., Invariant Measurement of Strange Sets in Terms of Cycles. *Phys. Rev. Lett.* 61:2729-2732, 1988.
- [18] Ott, E., C. Grebogi, and J. Yorke. Controlling Chaos. *Phys. Rev. Lett.* 64:1196-1199, 1990.
- [19] Schuster, H. G., ed. *Handbook of Chaos Control*. New York: Wiley-VCH, 1999.
- [20] Krasner, S., ed., *The Ubiquity of Chaos*. Washington, D.C.: American Assoc. for the Advancement of Science, 1990.
- [21] Chen, G., ed., *Controlling Chaos and Bifurcations in Engineering Systems*. New York: CRC Press, 2000.
- [22] Fradkov, A. L., and A. Y. Pogromsky. *Introduction to Control of Oscillations and Chaos*. New Jersey: World Scientific, 1998.
- [23] Giacomelli, G., and A. Politi. Relationship between Delayed and Spatially Extended Dynamical Systems. *Phys. Rev. Lett.* 76:2686-2689, 1996.
- [24] Arrechi, F. T., G. Giacomelli, A. Lapucci, and R. Meucci. Two-dimensional representation of a delayed dynamical system. *Phys. Rev. A* 45:R4225-R4228, 1992.
- [25] Hayes, S., C. Grebogi, E. Ott, and A. Mark. Communicating with Chaos. *Phys. Rev. Lett.* 70:3031-3034, 1993.
- [26] Hayes, S., C. Grebogi, E. Ott, and A. Mark. Communicating with Chaos. *Phys. Rev. Lett.* 73:1781-1784, 1994.
- [27] Van Wiggeren, G. D., and R. Roy. Communication with Chaotic Lasers. *Science* 279:1198-1200, 1998.

- [28] Van Wiggeren, G. D., and R. Roy. Optical Communication with Chaotic Waveforms. *Phys. Rev. Lett.* 81:3547-3550, 1998.
- [29] Van Wiggeren, G. D., and R. Roy. Chaotic communication using time-delayed optical systems. *Int. J. Bifurcation and Chaos* 9:2129-2156, 1999.
- [30] Luo, L. G., and P. L. Chu. Optical secure communications with chaotic erbium-doped fiber lasers. *J. Opt. Soc. Am. B* 15:2524-2530, 1998.
- [31] Goedgebuer, J.-P., L. Larger, and H. Porte. Optical Cryptosystem Based on Synchronization of Hyperchaos Generated by a Delayed Feedback Tunable Laser Diode. *Phys. Rev. Lett.* 80:2249-2252, 1998.
- [32] Cuenot, J.-B., L. Larger, J.-P. Goedgebuer, and W. T. Rhodes. Chaos Shift Keying with an Optoelectronic Encryption System Using Chaos in Wavelength. *IEEE J. of Quant. Elec.* QE-37:849-855, 2000.
- [33] Sivaprakasam, S. and K. A. Shore. Signal masking for chaotic optical communication using external-cavity diode lasers. *Opt. Lett.* 24:1200-1202, 1999.
- [34] Aida, T., and P. Davis. Oscillation modes of laser diode pumped hybrid bistable system with large delay and application to dynamical memory. *IEEE J. of Quant. Elec.* QE-28:686-699, 1992.
- [35] Aida, T. and P. Davis. Oscillation Mode Selection Using Bifurcation of Chaotic Mode Transitions in a Nonlinear Ring Resonator. *IEEE Trans. Quant. Elec.* 30:2986-2997, 1994.
- [36] Sinha, S. and W. L. Ditto, Dynamics-based computation, *Phys. Rev. Lett.* 81:2156-2159, 1998.
- [37] Sinha, S. and W. L. Ditto, Computing with distributed chaos, *Phys. Rev. E* 60:363-377, 1999.
- [38] Sukow, D. W., "Experimental Control of Instabilities and Chaos in Fast Dynamical Systems." Ph. D. diss., Duke University, 1997.
- [39] Pyragas, K. Continuous control of chaos by self-controlling feedback. *Phys. Lett. A* 170:421-428, 1992.
- [40] Ikeda, K., and K. Matsumoto. High-Dimensional Chaotic Behavior in Systems with Time-Delayed Feedback. *Physica D* 29:223-235, 1987.

- [41] Mackey, M. C., and L. Glass. Oscillation and Chaos in Physiological Control Systems. *Science* 197:287-289, 1977.
- [42] Goedgebuer, J.-P., L. Larger, H. Porte, and F. Delorme. Chaos in wavelength with a tunable laser diode. *Phys. Rev. E* 57:2795-2798, 1998.
- [43] Liu, Y. and J. Ohtsubo. Period-three cycle in a chaotic system using a laser diode active interferometer. *Opt. Comm.* 93:311-317, 1992.
- [44] Goedgebuer, J.-P., P. Levy, L. Larger, C.-C. Chen, and W. T. Rhodes. Optical Communication With Synchronized Hyperchaos Generated Electrooptically. *IEEE J. of Quant. Elec.* QE-38:1178-1183, 2002.
- [45] Celka, P., Chaotic Synchronization and Modulation of Nonlinear Time-Delayed Feedback Optical-Systems. *IEEE Trans. Circuits Syst. I* 42:455-463, 1995.
- [46] Ogata, K., *Modern Control Engineering*. 2d ed. New Jersey: Prentice Hall, 1990.
- [47] El'sgol'ts, L. E., and S. B. Norkin. *Introduction to the Theory and Application of Differential Equations with Deviating Arguments*. New York: Academic Press, 1973.
- [48] Strogatz, S. H., *Nonlinear Dynamics and Chaos with Applications to Physics, Biology, Chemistry, and Engineering*. Cambridge: Perseus Publishing, 1994.
- [49] Sukow, D. W., M. E. Bleich, D. J. Gauthier, and J. E. S. Socolar. Controlling chaos in a fast diode resonator using extended time-delay autosynchronization: Experimental observations and theoretical analysis. *Chaos* 7:560-576, 1997.
- [50] Just, W., D. Reckwerth, E. Reibold, and H. Benner. Influence of control loop latency on time-delayed feedback control. *Phys. Rev. E* 59:2826-2829, 1999.
- [51] Callender, A., D. R. Hartree, and A. Porter. Time Lag in a control system. *Philosoph. Trans. Royal Soc. London*, 235, 415-444, 1936.
- [52] Niculescu, S.-I., *Delay Effects on Stability: A Robust Control Approach*. New York: Springer, 2001.
- [53] Dugard, L., and E. I. Verriest, eds., *Stability and Control of Time-Delay Systems*. New York: Springer, 1998.

- [54] Sukow, D. W., and D. J. Gauthier. Entraining Power-Dropout Events in an External-Cavity Semiconductor Laser Using Weak Modulation of the Injection Current. *IEEE J. of Quant. Elec.* QE-36:175-183, 2000.
- [55] Abarbanel, H. D. I., M. B. Kennel, M. Buhl, and C. T. Lewis. Chaotic dynamics in erbium-doped fiber ring lasers. *Phys. Rev. A* 60: 2360-2374, 1999.
- [56] Williams, Q. L., and R. Roy. Fast polarization dynamics of an erbium-doped fiber ring laser. *Opt. Lett.* 21:1478-1480, 1996.
- [57] Turovets, S. I., J. Dellunde, and K. A. Shore. Nonlinear dynamics of a laser diode subjected to both optical and electronic feedback. *J. Opt. Soc. Am. B* 14:200-208, 1997.
- [58] Liu, Y., P. Davis, and T. Aida. Synchronized chaotic mode hopping in DBR lasers with delayed opto-electrical feedback. *IEEE J. of Quant. Elec.* QE-37:337-352, 2001.
- [59] Romeiras, F. J., C. Grebogi, E. Ott, and W. P. Dayawansa. Controlling chaotic dynamical systems. *Physica D* 58:165-192, 1992.
- [60] Ditto, W. L., S. N. Rauseo, and M. L. Spano, Experimental control of chaos. *Phys. Rev. Lett.* 65: 3211-3214, 1990.
- [61] Hunt, E. R., Stabilizing high-period orbits in a chaotic system: The diode resonator. *Phys. Rev. Lett.* 67:1953-1955, 1991.
- [62] Roy, R., T. W. Murphy, Jr., T. D. Maier, Z. Gills, and E. R. Hunt. Dynamical control of a chaotic laser: Experimental stabilization of a globally coupled system, *Phys. Rev. Lett.* 68, 1259-1262, 1992.
- [63] Myneni, K., T. A. Barr, N. J. Corron, and S. D. Pethel. New Method for the Control of Fast Chaotic Oscillations. *Phys. Rev. Lett.* 83:2175-2178, 1999.
- [64] Bleich, M. E., and J. E. S. Socolar. Stability of periodic orbits controlled by time-delay feedback. *Phys. Lett. A* 210: 87-94, 1996.
- [65] Just, W., T. Bernard, M. Ostheimer, E. Reibold, and H. Benner. Mechanism of Time-Delayed Feedback Control. *Phys. Rev. Lett.* 78:203-206, 1997.
- [66] Just, W., E. Reibold, K. Kacperski, P. Fronczak, J. A. Holyst, and H. Benner. Influence of stable Floquet exponents on time-delayed feedback control. *Phys. Rev. E* 61: 5045-5056, 2000.

- [67] Pyragas, K., and A. Tamševičius. Experimental control of chaos by delayed self-controlling feedback. *Phys. Lett. A* 180:99-102, 1993.
- [68] Lüthje, O., S. Wolff, and G. Pfister. Control of Chaotic Taylor-Couette Flow with Time-Delayed Feedback. *Phys. Rev. Lett.* 86:1745-1748, 2001.
- [69] Dykstra, R., D. Y. Tang, and N. R. Heckenberg. Experimental control of single-mode laser chaos by using continuous, time-delayed feedback. *Phys. Rev. E* 57:6596-6598, 1998.
- [70] Pierre, T., G. Bonhomme, and A. Atipo. Controlling the Chaotic Regime of Nonlinear Ionization Waves using the Time-Delay Autosynchronization Method. *Phys. Rev. Lett.* 76:2290-2293, 1996.
- [71] Gravier, E., X. Caron, G. Bonhomme, and T. Pierre. Control of the chaotic regime of nonlinear drift-waves in a magnetized laboratory plasma. *Phys. Plasmas* 6:1670-1673, 1999.
- [72] Socolar, J. E. S., D. W. Sukow, and D. J. Gauthier. Stabilizing unstable periodic orbits in fast dynamical systems. *Phys. Rev. E* 50:3245-3248, 1994.
- [73] Lu, W., and R. G. Harrison. Controlling chaos using continuous interference feedback: proposal for all optical devices. *Opt. Comm.* 109:457-461, 1994.
- [74] Nakajima, H. and Y. Ueda. Half-period delayed feedback control for dynamical systems with symmetries. *Phys. Rev. E* 58:1757-1763, 1998.
- [75] Ikeda, K., K. Kondo, and O. Akimoto. Successive Higher-Harmonic Bifurcations in Systems with Delayed Feedback. *Phys. Rev. Lett.* 49:1467-1470, 1982.
- [76] Ikeda, K., H. Daido, and O. Akimoto. Optical Turbulence: Chaotic Behavior of Transmitted Light from a Ring Cavity. *Phys. Rev. Lett.* 45:709-712, 1980.
- [77] Carmichael, H. J., R. R. Snapp, and W. C. Schieve. Oscillatory instabilities leading to “optical turbulence” in a bistable ring cavity. *Phys. Rev. A* 26:3408-3422, 1982.
- [78] Gopalsamy, K., *Stability and Oscillations in Delay Differential Equations of Population Dynamics*. Boston: Kluwer Academic, 1992.
- [79] van Tartwijk, G. H. M., and D. Lenstra. Semiconductor Lasers with optical injection and feedback. *Quantum Semiclass. Opt.* 7:87-143, 1995.

- [80] Mork, J., B. Tromborg, and J. Mark, Chaos in Semiconductor Lasers with Optical Feedback: Theory and Experiment. *IEEE J. of Quant. Elec.* QE-28:93-108, 1992.
- [81] Otsuka, K., and J.-L. Chern. High-speed picosecond pulse generation in semiconductor lasers with incoherent optical feedback. *Opt. Lett.* 16:1759-1761, 1991.
- [82] Arrechi, F. T., G. Giacomelli, A. Lapucci, and R. Meucci. Dynamics of a CO₂ laser with delayed feedback: The short-delay regime. *Phys. Rev. A* 43:4997-5004, 1991.
- [83] Arrechi, F. T., Space-time complexity in nonlinear optics. *Physica D* 51:450-464, 1991.
- [84] Labate, A., M. Ciofini, and R. Meucci. Controlling quasiperiodicity in a CO₂ laser with delayed feedback. *Phys. Rev. E* 57:5230-5236, 1998.
- [85] Ohtsubo, J., and Y. Liu. Optical bistability and multistability in an active interferometer. *Opt. Lett.* 15: 731-733, 1990.
- [86] Ohtsubo, J., and Y. Liu. Observation of higher harmonic bifurcations in a chaotic system using a laser diode active interferometer. *Opt. Comm.* 85:457-461, 1991.
- [87] Udaltsov, V. S., L. Larger, J.-P. Goedgebuer, M. W. Lee, E. Genin, and W. T. Rhodes. Bandpass Chaotic Dynamics of Electronic Oscillator Operating With Delayed Nonlinear Feedback. *IEEE Trans. Circuits Syst. I* 49:1006-1009, 2002.
- [88] Pérez, G., and H. A. Cerdeira. Extracting Messages MAsked by Chaos. *Phys. Rev. Lett.* 74:1970-1973, 1995.
- [89] Short, K. M., and A. T. Parker. Unmasking a hyperchaotic communication scheme. *Phys. Rev. E* 58:1159-1162, 1998.
- [90] Short, K., Signal Extraction from Chaotic Communications. *Intl. J. Bifurcation Chaos* 7:1579-1597, 1997.
- [91] Kobayashi, S., Y. Y. Yamamoto, M. Ito, and T. Kimura. Direct Frequency Modulation in AlGaAs Semiconductor Lasers. *IEEE J. of Quant. Elec.* QE-18:582-595, 1982.

- [92] Tsai, C.-Y., C.-H. Chen, T.-L. Sung, C.-Y. Tsai, and J. M. Rorison. Theoretical modeling of carrier and lattice heating effects for frequency chirping in semiconductor lasers. *Appl. Phys. Lett.* 74:917-919, 1999.
- [93] Liu, J.-M., and T. B. Simpson, Four-Wave Mixing and Optical Modulation in a Semiconductor Laser, *IEEE J. of Quant. Elec.* QE-30:957-965, 1994.
- [94] Vahala, K. J., and M. A. Newkirk, Parasitic-Free Modulation of Semiconductor Lasers. *IEEE J. of Quant. Elec.* QE-25:1393-1398, 1989.
- [95] Agrawal, G. P., and N. K. Dutta. *Long-Wavelength Semiconductor Lasers*. New York: Van Nostrand Reinhold Company, 1986.
- [96] Petermann, K., *Laser Diode Modulation and Noise*. Boston: Kluwer Academic Pub., 1988.
- [97] Hall, R. N., G. H. Fenner, J. D. Kingsley, T. J. Soltys, and R. D. Carlson. Coherent Light Emission from GaAs Junctions. *Phys. Rev. Lett.* 9:366-368, 1962.
- [98] Holonyak, N. Jr., and S. F. Bevacqua. Coherent (Visible) Light Emission from Ga(As_{1-x}P_x) Junctions. *Appl. Phys. Lett.* 1:82-83, 1962.
- [99] Nathan, M. I., W. P. Dumke, G. Burns, F. H. Hill, Jr., and Gordon Lasher. Stimulated Emission of Radiation from GaAs p-n Junctions. *Appl. Phys. Lett.* 1:62-63, 1962.
- [100] Quist, T. M., R. H. Rediker, R. J. Keyes, W. E. Krag, B. Lax, A. L. McWorther, and H. J. Zeiger. Semiconductor Maser of GaAs. *Appl. Phys. Lett.* 1:91-92, 1962.
- [101] Press, W. H., B. P. Flannery, S. A. Teukolsky, and W. T. Vetterling, *Numerical Recipes in C: The Art of Scientific Computing*. 2nd ed., Cambridge: University Press, 1992.
- [102] LeBerre, M., E. Ressayre, and A. Tallet. Type-I Intermittency Route to Chaos in a Saturable Ring-Cavity-Retarded Differential Difference System. *J. Opt. Soc. B* 5:1051-1062, 1988.
- [103] Kaiser, F., and D. Merkle. Routes to Chaos in a Delay-Differential Equation System Modelling a Passive Optical Resonator. *Phys. Lett. A* 139:133-140, 1989.

- [104] Kantz, H., and T. Schreiber. *Nonlinear Time Series Analysis*. New York: Cambridge University Press, 1997.
- [105] Abarbanel, H. D. I., *Analysis of Observed Chaotic Data*. New York: Springer, 1996.
- [106] Gao, J. Y., and L. M. Narducci. The effect of modulation in a bistable system with delay. *Opt. Comm.* 58:360-364, 1986.
- [107] Gao, J. Y., G. X. Jin, J. W. Sun, X. Z. Guo, Z. R. Zhen, N. B. Abraham, and L. M. Narducci. The effect of modulation in a bistable system with delay. *Opt. Comm.* 71:224-228, 1989.
- [108] Mensour, B., and A. Longtin. Power spectra and dynamical invariants for delay-differential and difference equations. *Physica D* 113:1-25, 1998.
- [109] Murkami, A., and J. Ohtsubo. Chaos synchronization based on a continuous chaos control method in semiconductor lasers with optical feedback. *Phys. Rev. E* 63:066203, 2001.
- [110] Celka, P., Synchronization of Chaotic Optical Dynamical Systems Through 700 m of Single Mode Fiber. *IEEE Trans. Circuits Syst. I* 43:869-872, 1996.
- [111] Rogister, F., D. W. Sukow, A. Gavrielides, P. Mégret, O. Deparis, and M. Blondel. Experimental demonstration of suppression of low-frequency fluctuations and stabilization of an external-cavity laser diode. *Opt. Lett.* 25:808-810, 2000.
- [112] Hohl, A., and A. Gavrielides. Experimental control of a chaotic semiconductor laser. *Opt. Lett.* 23:1606-1608, 1998.
- [113] Gauthier, D. J., Private communication.
- [114] Just, W., "Principles of Time Delayed Feedback Control" in *Handbook of Chaos Control*, ed. H. G. Schuster, 21-41. New York: Wiley-VCH, 1999.
- [115] Hövel, P., and J. E. S. Socolar. Stability domains for time-delay feedback control with latency. Submitted for publication.
- [116] Kittel, A., J. Parisi, and K. Pyragas. Delayed feedback control of chaos by self-adapted delay time, *Phys. Lett. A* 198:433-436, 1995.

- [117] Nakajima, H., H. Ito, and Y. Ueda. Automatic adjustment of delay time in delayed feedback control of chaos, *IEICE Trans. Fund.* E80:1554- , 1997.
- [118] Gauthier, D. J., and J. C. Bienfang. Intermittent Loss of Synchroniztion in Coupled Chaotic Oscillators: Toward a New Criterion for High-Quality Synchronization. *Phys. Rev. Lett.* 77:1751-1754, 1996.
- [119] Blakely, J. N., D.J. Gauthier, G. Johnson, T.L. Carroll, and L.M. Pecora. Experimental investigation of high-quality synchronization of coupled oscillators. *Chaos* 10:738-744, 2000.
- [120] Gerosa, A., R. Bernardini, and S. Pietri. A Fully Integrated Chaotic System for the Generation of Truly Random Numbers. *IEEE Trans. Circuits Syst. I* 49:993-1000, 2002.
- [121] Gleeson, J. T., Truly random number generator based on turbulent electroconvection. *Appl. Phys. Lett.* 81:1949-1951, 2002.
- [122] Namajūnas, A., K. Pyragas, and A. Tamaševičius. An electronic analog of the Mackey-Glass system. *Phys. Lett. A* 201:42-46, 1995.

Biography

Jonathan Neal Blakely was born on August 9, 1974 in Durham, North Carolina. As a teenager, he became interested in modern physics after reading Stephen Hawking's *A Brief History of Time*. In 1992, he entered the University of North Carolina at Greensboro. While at UNC-G, he served as president of the local chapter of the Society of Physics Students, and was inducted into Sigma Pi Sigma Physics Honor Society and Phi Beta Kappa. In his senior year, he discovered "chaos" through an independent study. In 1996, he graduated magna cum laude earning a Bachelor of Science degree in physics. That summer he worked in UNC-G's Biophysics lab and in the Fall entered the graduate program in Physics at Duke University. In 1998, he earned a Master of Arts degree in physics from Duke University.

LIST OF PUBLICATIONS

J.N. Blakely and D.J. Gauthier, 'Attractor bubbling in coupled hyperchaotic oscillators,' an Invited article in the Theme Issue of Control and Synchronization of Chaos, *Int. J. Bifurction Chaos* 10, 835 (2000).

J.N. Blakely, D.J. Gauthier, G. Johnson, T.L. Carroll, and L.M. Pecora, 'Experimental investigation of high-quality synchronization of coupled oscillators,' *Chaos* 10, 738 (2000).

LIST OF PRESENTATIONS

'Flexible Source of High Speed Optical Chaos', Photonics in the Forest: Convocation of the Fitzpatrick Center for Photonics and Communication Systems, April 17, 2001, Durham, NC.

'Flexible Source of Optical Chaos for Use in Communications', Dynamics Days 2001, Chapel Hill, NC, January 4, 2001.

'Flexible Source of Optical Chaos for Use in Communications', OPTO-Southeast Meeting on Optoelectronics, Photonics, and Imaging, September 19, 2000, Charlotte, NC.

‘Observation of a New Scaling Relation in the Transition from Synchronized Chaos to Attractor Bubbling’, 66th Annual Meeting Southeastern Section Meeting of the APS, November 8, 1999, Chapel Hill, NC.

‘Experimental Evaluation of Several Proposed Criteria for Synchronization’, 5th SIAM Conference on Applications of Dynamical Systems, May 23, 1999, Snowbird, UT. (invited presentation)

‘Experimental Determination of the Coupling Required for Synchronization of Hyperchaos’, APS Centennial Meeting, March 22, 1999, Atlanta, GA.

‘Experimental Comparison of Synchronization Criteria Using Non-normal Oscillators’, Dynamics Days, January 6, 1999, Atlanta, GA.